NUMERICAL WAVE FORCE SIMULATION

Final Technical Report To:

Technology Assessment and Research Program
Minerals Management Service
Department of The Interior
MMS Contract No. 14-12-0001-30218

Professor J. Kim Vandiver
Massachusetts Institute of Technology
Room 5-222
Cambridge, Massachusetts 02139

January 15, 1986

INTRODUCTION

The general objectives of this project were to improve the understanding of hydrodynamic loading on offshore structures and to improve tchniques for computing loads on offshore structures. The loads are primarily due to waves and currents. The project included efforts on both topics. The body of this report consists of two graduate student theses and three professional papers. The theses address the topics of time and frequency domain representation of ocean waves and the three papers address the subject of current induced vibration of marine risers and cables. The remainder of this introduction defines the topics in more detail.

Wave Forces: Time Domain Simulation

Wave loads can be described and computed in the time domain or the frequency domain. In the time domain the computation of forces for the purpose of designing offshore structures requires knowledge of the wave kinematics over a three-dimension grid of points which usually also define the geometry of the structure of interest. The kinematics required are usually the wave surface elevation and the water particle velocities and accelerations. The pressure at each grid point is also useful at times. The results of this research project include a significant advancement in the methods of computing wave kinematics for time domain simulation. The results are applicable to deep and finite water depths, can account for the actual position of the free surface, and do not require the approximation of a random sea by a finite number of sinusoidal components, but in fact allow for modelling of a smooth continuous wave spectrum. This work is described in detail in the first report to follow this Introduction and is

entitled "Time Series Analysis of Ocean Waves". The results, as presented, allow the time domain calculation of wave kinematics over a large grid of points due to the passage of random waves from a single direction. The wave time history can be synthesized or can use measured wave data. The extension of the results to the simultaneous arrival of waves from many directions is simple. The waves are assumed to be linear. A multi-directional sea can be built up by superposition of individual wave time histories originating from several independent directions. At each grid point vector sums of velocities and accelerations are computed and then used in calculating forces. The greatest weakness in the simulation of multi-directional random seas has been in the author's opinion in the area of measuring and understanding real multi-directional seas. This requires improved methods of calculating directional wave spectra. This topic is addressed in the next paragraph.

Wave Forces: Frequency Domain Representation

Whereas time domain simulations are important for non-linear modelling of extreme events, such as the 100 year wave, linear frequency domain modelling is usually adequate for fatigue life estimates. Linear superposition allows wave spreading to be accounted for relatively easily in fatigue life estimates for offshore structures. However, knowledge of directional wave spectra is difficult to obtain because the measurements are expensive and difficult to make, and are usually far from optimum from the point of view of the person who must process the data into directional wave spectra. To make up for deficiencies in the data requires powerful multi-dimensional spectral estimation techniques. The second manuscript in

this report addresses the problem of multi-dimensional spectral estimation from non-optimal data sets, with particular application to wave number spectral estimation.

Current Loads

Current accounts for a major source of loading on long flexible cylinders such as marine risers, mooring cables, and suspended pipeline spans. The dominant loading mechanism is vortex shedding. Vortex excited response is far from being adequately understood, even for the purposes of design calculations. The major topic of importance to designers, which is as yet inadequately understood, is the response of a long cylinder such as riser to a spatially varying (sheared) flow. The principal investigator has worked on flow-induced response problems for ten years. In the course of the work of the past year three professional papers were completed. These are presented in this report. The first is a "state of the art" analysis of the response prediction problems in sheared flow. The paper is entitled "The Prediction of Lock-in Vibration on Flexible Cylinders in a Sheared Flow". The key hydrodynamic and structural dynamic parameters are discussed. A significant error in the earlier literature is pointed out and the areas requiring further work are clearly defined.

The last two papers bear on the problem of the simulation of vortex excited motions of risers. The phenomena is highly non-linear. Any attempt to simulate flow-induced motion must account for the non-linear relation between the fluid loads and structural motions. Most cylinders such as risers excited by flow exhibit very different response in the direction perpendicular to the flow (known as cross-flow motion) and

in-line motion. The paper entitled "The Relationship Between In-Line and Cross-Flow Vortex-Induced Vibration of Cylinders", for the first time in literature demonstrates and describes the non-linear relationship between the cross-flow and in-line response. The last paper entitled "The Identification of the Quadratic System Relating Cross-Flow and In-Line Vortex Induced Vibration" actually provides the methodology and theoretical basis for computing the non-linear transfer function between the cross-flow and in-line motions. Results based on field measurements of flow-induced vibration are presented. The non-linear transfer functions can be used in frequency or time domain simulations of response.

Acknowledgements

The authors wish to thank Mr. Charles E. Smith, the MMS research program manager for this project, for his confidence and support in the sponsorship of this work. Four graduate students benefitted directly from the opportunity to work on the research. The relevance to industry of the research supported by MMS over the years has been evidenced by the degree to which students have been sought after, and by the significant contributions that these past students have made professionally in very short periods of time after graduation.

TIME SERIES ANALYSIS OF OCEAN WAVES

by

DOUGLAS GLEN DOMMERMUTH

ABSTRACT

In this paper, the methods of digital-signal processing are applied to ocean waves. The applications of differentiation, fast Fourier transforms, and convolution integrals to time series generation of ocean waves are developed. In deep water, the vertical attenuation and horizontal propagation impulse response functions for ocean waves are solved analytically. In shallow water, the vertical-attenuation and horizontal-propagation problems are solved using the fast Fourier transform. The convolution integrals used to simulate irregular waves are faster than sum of sinusoids method.

Supervisor: Dr. J. K. Vandiver
Title: Professor of Ocean Engineering

CHAPTER 1 ANALYSIS OF OCEAN WAVES IN THE TIME DOMAIN

1.1 THE FREQUENCY DOMAIN VERSUS THE TIME DOMAIN . . . 1-1
1.2 APPLICATIONS OF TIME-DOMAIN ANALYSIS 1-3
1.3 MORISON'S EQUATION 1-4
1.4 SUMMARY OF CHAPTER ONE 1-6

CHAPTER 2 REGULAR AND IRREGULAR WAVES

2.1 AIRY WAVE THEORY 2-1
2.2 THEORY OF IRREGULAR WAVES 2-8
2.3 SUMMARY OF CHAPTER TWO 2-9

CHAPTER 3 THE CONTINUOUS SPECTRUM OF OCEAN WAVES

3.1 FOURIER TRANSFORMS AND INVERSE FOURIER TRANSFORMS 3-1
3.2 THE CONVOLUTION THEOREM IN THE TIME DOMAIN 3-3
3.3 THE FOURIER TRANSFORM AND CONVOLUTION INTEGRAL . . 3-4
3.4 THE TIME AND WAVE-FREQUENCY DOMAIN 3-5
3.5 THE SPACE AND WAVE-NUMBER DOMAIN 3-6
3.6 SUMMARY OF CHAPTER THREE 3-7

CHAPTER 4 TRANSFER FUNCTIONS FOR ANALYSIS OF OCEAN WAVES

4.1 EFFICIENT MODELING OF OCEAN WAVES 4-1
4.2 THE TRANSFER FUNCTIONS IN DEEP WATER 4-4
4.3 THE TRANSFER FUNCTIONS IN WATER OF FINITE DEPTH . 4-5
4.4 SUMMARY OF CHAPTER FOUR 4-7

CHAPTER 5 DIFFERENTIATING TIME SERIES OF OCEAN WAVES

5.1 THEORY OF DIFFERENTIATION OF SINUSOIDAL WAVES . . 5-1
5.2 NUMERICAL DIFFERENTIATION OF SINUSOIDAL WAVES . . 5-2
5.3 SUMMARY OF CHAPTER FIVE 5-3

CHAPTER 6 THE HORIZONTAL WATER-PARTICLE VELOCITY

6.1 HORIZONTAL WATER-PARTICLE VELOCITY - DEEP WATER . 6-1
6.2 HORIZONTAL WATER-PARTICLE VELOCITY - FINITE DEPTH 6-3
6.3 SUMMARY OF CHAPTER SIX 6-4

CHAPTER 7 THE VERTICAL-ATTENUATION PROBLEM

7.1 VERTICAL ATTENUATION IN DEEP WATER 7-1
7.2 VERTICAL ATTENUATION IN WATER OF FINITE DEPTH . . 7-3
7.3 SUMMARY OF CHAPTER SEVEN 7-4

CHAPTER 8 THE HORIZONTAL-PROPAGATION PROBLEM

8.1 HORIZONTAL PROPAGATION IN DEEP WATER 8-1
8.2 HORIZONTAL PROPAGATION IN WATER OF FINITE DEPTH . 8-7
8.3 SUMMARY OF CHAPTER EIGHT 8-8

CHAPTER 9 CONCLUSIONS

9.1 LIMITATIONS OF THE PROPOSED METHOD 9-1
9.2 ADVANTAGES OF THE PROPOSED METHOD 9-2

APPENDIX A DIFFERENTIATION

APPENDIX B THE HORIZONTAL WATER-PARTICLE VELOCITY

APPENDIX C VERTICAL ATTENUATION

APPENDIX D HORIZONTAL PROPAGATION

APPENDIX E BIBLIOGRAPHY

APPENDIX F FIGURES

F.1 TYPICAL OFFSHORE STRUCTURES F-2
F.2 FLOW NORMAL TO A CYLINDER'S AXIS F-3
F.3 FLOW IN-LINE WITH A CYLINDER'S AXIS F-4
F.4 COORDINATE SYSTEM FOR AIRY WAVE THEORY F-5
F.5 RANGE OF VALIDITY OF AIRY WAVE THEORY F-6
F.6 COORDINATE SYSTEM FOR THE GRID F-7
F.7 ALGORITHM FOR GENERATING WAVE KINEMATICS I F-8
F.8 ALGORITHM FOR GENERATING WAVE KINEMATICS II . . . F-9
F.9 HORIZONTAL WATER-PARTICLE VELOCITY I F-10
F.10 HORIZONTAL WATER-PARTICLE VELOCITY II F-11
F.11 VERTICAL ATTENUATION IN DEEP WATER F-12
F.12 VERTICAL ATTENUATION IN WATER IN FINITE DEPTH . F-13
F.13 HORIZONTAL PROPAGATION IN DEEP WATER I F-14
F.14 HORIZONTAL PROPAGATION IN DEEP WATER II F-15
F.15 HORIZONTAL PROPAGATION IN FINITE WATER DEPTHS . F-16
F.16 SUM OF SINUSOIDS VERSUS THE PROPOSED METHOD I . F-17
F.17 SUM OF SINUSOIDS VERSUS THE PROPOSED METHOD II . F-18
F.18 ERROR ANALYSIS OF CENTRAL DIFFERENCE METHOD . . F-19
F.19 SINUSOIDAL WAVE CONTAMINATED WITH NOISE F-20
F.20 DERIVATIVE OF A WAVE CONTAMINATED WITH NOISE I . F-21
F.21 DERIVATIVE OF A WAVE CONTAMINATED WITH NOISE II F-22

APPENDIX G TABLES

G.1 AIRY WAVE THEORY IN FINITE WATER DEPTHS G-2
G.2 AIRY WAVE THEORY IN DEEP WATER G-3

CHAPTER 1

ANALYSIS OF OCEAN WAVES IN THE TIME DOMAIN

1.1 THE FREQUENCY DOMAIN VERSUS THE TIME DOMAIN

Time-domain analysis can be very useful for the design of offshore structures. However, time-domain analysis is not performed very often because the software in use today is inefficient. Instead frequency-domain analysis is used. A frequency-domain analysis is made efficient by the many linearizations that are imposed. The motions, exciting and restraining forces, and wave kinematics are linearized to perform a frequency-domain analysis. But these linearizations make the frequency domain a worse model of reality than the time domain because the time domain does model nonlinearities. Also, physically, the time domain is a better choice than the frequency domain because natural phenomena change with time, not with frequency. Both the frequency domain and time domain have certain advantages and disadvantages which make the proper choice for analysis extremely important.

The response of an offshore structure to a storm is very nonlinear. Since the frequency domain cannot model nonlinearities, it cannot model response to storms. It models the response of an offshore structure under normal operating conditions. It is best used during preliminary design, in the early stages of the design spiral, when there are many possible solutions. It is an efficient and inexpensive way of eliminating poor design choices. Unlike the frequency domain, the time domain can model the response of an offshore structure to a storm. It is best used during final design, near the end of the design spiral, when only one or two designs are being considered. Poor design choices that are not found by a frequency-domain analysis can be found by a time-domain analysis.

Together with model tests, the time domain can be a valuable method of design. If it is used properly, it will certainly help to avoid accidents such as befell the Ocean Ranger and Glomar Explorer. This is especiallly important as the search for oil is extended into deeper and harsher environments.

Time-domain analysis will become more attractive as it becomes more efficient. Its inefficiency leads to very expensive and extremely long computer simulations. One of the leading contributors to this inefficiency is the algorithm which models irregular seas. This paper will

demonstrate an efficient method for modeling irregular seas.

1.2 APPLICATIONS OF TIME-DOMAIN ANALYSIS

Time-domain analysis of an offshore structure's response to ocean waves can identify poor design choices. Specifically, the ocean engineer is most interested in preventing structural failure. Other design objectives include flood prevention, station-keeping ability, and good seakeeping characteristics. Time-domain analysis can help meet all of these design objectives. Useful applications of time-domain analysis include dynamic response of jackets, hybrid towers, guyed towers, and risers. Other applications include seakeeping response of semisubmersibles and tension-leg platforms. As seen in figure F.1, all of these structures are made of slender cylinders. In general, Morison's equation can be used to model the dynamic response of a cylinder to an ocean wave when the cylinder's diameter is smaller than the wave's length. The application of Morison's equation is controversial. Yet, for the problems we want to solve, Morison's equation gives results which are in good agreement with experiments.

1.3 MORISON'S EQUATION

For forces normal to a cylinder's axis, Morison's equation can be expressed as (figure F.2)

$$\vec{F_n} = C_a \rho \nabla (\vec{\dot{u}_n} - \vec{\ddot{x}_n}) + \rho \nabla \vec{\dot{u}_n} + C_d \frac{1}{2} \rho A |\vec{u_n} - \vec{\dot{x}_n}| (\vec{u_n} - \vec{\dot{x}_n}) \qquad (1.1)$$

where the variables have the following definitions:

1) $\vec{F_n}$ is the vector of hydrodynamic forces normal to the cylinder's axis,

2) C_a is the added-mass coefficient and C_d is the viscous-drag coefficient for flow normal to the cylinder's axis,

3) ρ is the mass density of water,

4) ∇ is the volume of the cylinder,

5) A is the projected area in the direction of the normal, and

6) $\vec{u_n}$, $\vec{\dot{x}_n}$, $\vec{\dot{u}_n}$, and $\vec{\ddot{x}_n}$ are normal components of the water-particle velocity, the cylinder's velocity, the water-particle acceleration, and the cylinder's acceleration respectively.

The first term in the equation is called the added-mass force. This term models forces proportional to acceleration. The second term models forces proportional to the gradient of pressure. The last term models viscous forces. Morison's equation does not model diffraction. However, Morison's equation can be a good model of the hydrodynamic forces acting on cylinders with diameters less than one-quarter of the wave length. Furthermore, unlike

most potential flow models, Morison's equation does model viscous forces. These forces can be the greatest proportion of the total force acting on offshore structures.

Similiarly, the hydrodynamic forces acting in-line with a cylinder's axis can be expressed as (figure F.3)

$$\vec{F_t} = C_a \rho \forall (\dot{\vec{u}}_t - \ddot{\vec{x}}_t) + P_D A \vec{t} + C_d \frac{1}{2} \rho A |\vec{u}_t - \dot{\vec{x}}_t| (\vec{u}_t - \dot{\vec{x}}_t) \qquad (1.2)$$

where the variables have the following definitions:

1) $\vec{F_t}$ is the vector of hydrodynamic forces in-line with the cylinder's axis,

2) C_a is the added-mass coefficient of an equivalent sphere having a cross-sectional area equal to the area of the end of the cylinder and C_d is the viscous drag coefficient of an equivalent disc that has the same area as the end of the cylinder,

3) $\vec{t}$ is the unit vector in-line with the cylinder's axis,

4) P_D is the dynamic component of pressure,

5) $\forall$ is the volume of the equivalent sphere,

6) A is the area of the end of the cylinder, and

7) $\vec{u}_t$, $\dot{\vec{x}}_t$, $\dot{\vec{u}}_t$, and $\ddot{\vec{x}}_t$ are in-line components of the water-particle velocity, the cylinder's velocity, the water-particle acceleration, and the cylinder's acceleration respectively.

The water-particle velocities, accelerations, and pressures are required in Morison's equation. Furthermore, the free-suface elevation must be known so that the

hydrodynamic forces acting on all submerged cylinders can be calculated. Presently, the algorithm used to compute these quantities is very inefficient. In this paper, a more efficient method for computing these quantities will be developed.

1.4 SUMMARY OF CHAPTER ONE

The response of offshore structures to ocean waves can be analyzed in either the frequency domain or time domain. Frequency-domain analysis is best used during preliminary design, whereas time-domain analysis is best used during final design. Time-domain analysis is not used as often as it should be because it is inefficient, but it can become more efficient. For certain offshore structures, Morison's equation can be used to model the hydrodynamic forces. Presently, the algorithm used to compute the wave properties required by Morison's equation is very inefficient. A more efficient method will be developed in this paper. First, Airy wave theory will be reviewed. Then a theory of irregular waves will be developed which is based on Airy wave theory. This theory is more efficient than what is used today.

CHAPTER 2

REGULAR AND IRREGULAR WAVES

2.1 AIRY WAVE THEORY

Subject to certain limitations, Airy wave theory can be a very useful model of ocean waves. To understand those limitations, we must review the theory's derivation. Our final objective will be a model for irregular waves. Since irregular waves are a superposition of regular waves, we will use many Airy waves to simulate irregular waves. Therefore, the theory of irregular waves which we will develop will have limitations similiar to those of Airy waves.

We will define our coordinate system such that the Z-axis is positive up and the X-axis positive to the right. Furthermore, we will fix the origin at the mean waterline (figure F.4).

The first assumption we will make is that the fluid is inviscid or ideal.

$$\gamma = 0. \tag{2.1}$$

where γ is the kinematic viscosity. Since we have assumed an ideal fluid, there will be no energy dissipation due to viscous damping. This is valid because we are only interested in waves that travel short distances in the neighborhood of the offshore structure. For these short distances, we do not expect that the viscous damping will have a significant effect.

The second assumption we will make is that the fluid is incompressible.

$$\frac{\partial \rho}{\partial t} = \frac{\partial \rho}{\partial x} = \frac{\partial \rho}{\partial z} = 0. \tag{2.2}$$

where ρ is the density of the fluid. Intuitively, this seems to be a reasonable assumption. However, it is possible to model the compressibility of the fluid. In fact, even for water, compressibility can significantly affect added-mass and wave-damping calculations.

The third assumption we will make is that the fluid is irrotational.

$$\nabla \times \vec{V} \tag{2.3}$$

where ∇ is the del operator and $\vec{V}$ is the fluid particle

velocity vector. This important assumption enables us to express the velocity field in terms of the gradient of a scalar function Φ .

$$\vec{V} = \nabla\Phi \tag{2.4}$$

where Φ is defined as the velocity potential. Le Mehaute in his book An Introduction to Hydrodynamics and Water Waves, gives a good discussion of irrotational motion:

> A deep water swell, i.e., wave generated by wind traveling out of the generating area, is probably the motion which most closely approaches the condition of irrotationality. But under wind action the free surface shearing stress induces rotationality (and turbulence) in the direction of wave travel... Also, in shallow water, the bottom friction induces rotationality.... Rotationality at the crest in the direction of wave travel will reduce the limit wave steepness... Rotationality in the oposite direction will theoretically increase the limit wave steepness.

Using these arguments, we expect our theory to become less valid as the wave becomes steeper and the water shallower. These are limitations to the theory we propose. However, as we will soon discover, they are not very strong limitations.

By the continuity principle, equal amounts of fluid must enter and exit a control volume. Therefore,

$$\nabla^2\Phi = 0. \qquad \text{in the fluid.} \tag{2.5}$$

This equation is called Laplace's equation. It is the governing differential equation.

We must solve Laplace's equation and also satisfy the free-surface and bottom-boundary conditions. The bottom-boundary condition is that no fluid can move across the bottom - the normal component of fluid velocity must be zero.

$$\frac{\partial \Phi}{\partial z} = 0. \qquad \text{on } z=-h, \quad (2.6)$$

where h is the water depth. This boundary condition does not allow for sloped bottoms. However, in the neighborhood of the offshore structure the bottom will be horizontal. For rigid, hard, horizontal bottoms, this boundary condition is exact.

The kinematic boundary condition on the free surface is that the fluid particles near the free surface can only move tangentially to the free surface. The nonlinear boundary condition is

$$\frac{D(z-\eta)}{Dt} = -\frac{\partial \eta}{\partial t} - \frac{\partial \eta}{\partial x}\frac{\partial \Phi}{\partial x} + \frac{\partial \Phi}{\partial z} = 0. \qquad \text{on } z=\eta, \quad (2.7)$$

where $\frac{D}{Dt}$ is the substantial derivative, and η is the free-surface elevation. This equation can be linearized if we assume that that the product of $\frac{\partial \eta}{\partial x}$ and $\frac{\partial \Phi}{\partial x}$ is very small compared to the other terms in the equation. (This is the fourth assumption we have made.) This is a limitation on the steepness of the waves we can model because $\frac{\partial \eta}{\partial x}$ and $\frac{\partial \Phi}{\partial x}$ are measures of the slope of the wave. It is a much stronger

limitation on steepness than that due to irrotationality. The linearized kinematic boundary condition on the free surface becomes

$$\frac{\partial \Phi}{\partial z} = \frac{\partial \eta}{\partial t} \qquad \text{on } z=0. \qquad (2.8)$$

Unlike the fully nonlinear boundary condition, the linear boundary condition is satisfied on the mean waterline. Since the steepness of the wave is small, the potential, the free-surface elevation, and their derivatives evaluated on the free surface can be expanded in a Taylor series expansion about the mean waterline.

The dynamic boundary condition on the free surface is that the pressure must be continuous across the free surface - the water pressure immediately below the free surface must be equal to the air pressure immediately above. We can use Bernoulli's equation to show

$$\frac{\partial \Phi}{\partial t} + \frac{1}{2} \nabla \Phi \cdot \nabla \Phi + g\eta = 0. \qquad \text{on } z=\eta, \qquad (2.9)$$

where g is the acceleration of gravity. Since it is consistent with our earlier assumption that the slope of the wave is small, we can neglect the nonlinear terms. Then the linearized dynamic boundary condition on the free surface becomes

$$\eta = -\frac{1}{g} \frac{\partial \Phi}{\partial t} \qquad \text{on } z=0. \qquad (2.10)$$

This boundary condition is also satisfied on the mean waterline.

The kinematic and dynamic boundary conditions on the free surface can be combined into

$$\frac{\partial^2 \Phi}{\partial t^2} + g\frac{\partial \Phi}{\partial z} = 0. \qquad \text{on } z=0. \qquad (2.11)$$

This is called the free-surface boundary condition or the wave equation.

A solution of Laplace's equation which satisfies the bottom and free-surface boundary conditions is

$$\Phi = Re\, -\frac{i\omega A}{k}\frac{\cosh(k(z+h))}{\sinh(kh)} e^{i(kx-\omega t)} \qquad (2.12)$$

where ω is the wave frequency, k is the wave number, A is the wave amplitude, and t is time. (In equation (2.12) we have used complex notation. Throughout this report we will use the symbol Re to indicate that the real part must be taken.) Furthermore, the wave frequency and wave number must satisfy the dispersion relation.

$$\omega^2 = kg\tanh(kh) \qquad (2.13)$$

We can use the dispersion relation to find the speed of a wave crest.

$$c = \frac{\omega}{k} = \sqrt{\frac{g}{k}\tanh(kh)} \qquad (2.14)$$

where c is called the phase velocity. The phase

velocity is a nonlinear function of frequency and wavelength because

$$k = 2\pi/\lambda \tag{2.15}$$

where λ is the wavelength. In general, for the same water depth, longer waves will travel faster than shorter waves. This phenomenon is called dispersion, and it explains why equation 2.13 is called the dispersion relation.

The derivation of Airy wave theory requires us to assume:

1) the wave's amplitude is much smaller than the wavelength,

2) the fluid is irrotational,

3) the fluid is ideal, and

4) the fluid is incompressible.

These assumptions limit the type of wave motion we can model well. Basically, Airy wave theory is not a good model of steep waves or waves traveling in shallow water. In general, Airy wave theory is a good model of long ocean waves in a region slightly below the free surface and slightly above the bottom. Le Mehaute has suggested a range for which Airy wave theory would be suitable (figure F.5).

The results of Airy wave theory for finite and infinite water depths respectively are summarized in tables G.1 and G.2. Airy wave theory is the basis for the theory of irregular waves which will be developed in this paper.

2.2 THEORY OF IRREGULAR WAVES

Presently, a finite number of regular waves are superposed to model irregular seas. Each regular wave has a distinct frequency and random phase. For example, the free surface elevation in two dimensions is given by

$$\eta = Re \sum_{n=1}^{N} A_n e^{i(k_n x - \omega_n t)} \qquad (2.16)$$

where N is the number of regular wave components, A_n is a complex wave amplitude with random phase, k_n is a wave number, x is the distance propagated, ω_n is a wave frequency, and t is time. Other wave properties can also be represented in this manner. This technique is called sum of sinusoids. It is based on the principle of superposition. It is inefficient because it requires many multiplications and additions. Another, less obvious, and undesireable characteristic is the discrete representation of the seastate. Consequently, the distribution of wave energy is not continuous. Furthermore, this method does not allow for wave breaking. When a wave becomes too steep, it will break. Sum of sinusoids can

create waves that are so steep they are physically impossible. This paper will demonstrate an alternative method to sum of sinusoids whcih is more efficient and gives a continuous distribution of energy. However, it also does not allow for wave breaking. Furthermore, since it is based on Airy wave theory, it is subject to the same limitations as that theory.

2.3 SUMMARY OF CHAPTER TWO

Subject to certain limitations, Airy wave theory can be a very useful model of ocean waves. In general, Airy wave theory is not a good model of very steep waves or waves in very shallow water. Airy wave theory is a good model of long waves in deep water. Since Airy wave theory is linear, many regular waves can be superposed to model irregular seas. As the number of regular waves approaches infinity, the distribution of wave energy becomes continuous, and the Fourier series becomes a Fourier transform. In the next chapter it will be shown how Fourier transforms and convolution integrals can be used to model waves more efficiently than sum of sinusoids.

CHAPTER 3

THE CONTINUOUS SPECTRUM OF OCEAN WAVES

3.1 FOURIER TRANSFORMS AND INVERSE FOURIER TRANSFORMS

To begin this problem, the Fourier transform and its inverse will be defined. This will not be a rigorous analysis, but it will be a good introduction to the applications of the Fourier transform. For example, suppose we know a function in the time domain. The fourier transform of this function can be used to find its expression in the frequency domain as follows:

$$F(\omega) = \int_{-\infty}^{\infty} f(t)\, e^{i\omega t}\, dt \tag{3.1}$$

where $f(t)$ is in the time domain and $F(\omega)$ is in the frequency domain. $f(t)$ might represent the free-surface elevation, the water-particle velocity or acceleration, or the water pressure. The inverse Fourier transform is defined as

$$f(t) = \frac{1}{2\pi} \int_{-\infty}^{\infty} F(\omega)\, e^{-i\omega t}\, dt \tag{3.2}$$

Therefore, equation (3.1) can now be expressed as

$$f(t) = \frac{1}{2\pi} \int_{-\infty}^{\infty} \int_{-\infty}^{\infty} f(\tau)\, e^{i\omega\tau}\, d\tau\, e^{-i\omega t}\, d\omega \qquad (3.3)$$

In certain cases the order of integration can be changed.

$$f(t) = \int_{-\infty}^{\infty} d\tau\, f(\tau) \frac{1}{2\pi} \int_{-\infty}^{\infty} d\omega\, e^{-i\omega(t-\tau)} \qquad (3.4)$$

Since the second integral is a delta function,

$$f(t) = \int_{-\infty}^{\infty} d\tau\, f(\tau)\, \delta(t-\tau) = f(t) \qquad (3.5)$$

Therefore, it has been shown that the inverse fourier transform of the transform of $f(t)$ is $f(t)$. This is very convenient because the wave properties we know in the frequency domain, as a result Airy wave theory, can also be expressed in the time domain. However, there are limitations to this theory. In general, the Fourier transform of a function will exist if the absolute value of the function integrated over the range from $-\infty$ to ∞ exists. This rather modest beginning leads to a very important result - the convolution theorem.

3.2 THE CONVOLUTION THEOREM IN THE TIME DOMAIN

Having defined the fourier transform and its inverse, the convolution theorem can now be derived. For example, suppose we know a transfer function in the frequency domain which will convert the horizontal component of water-particle velocity into the vertical component of water-particle velocity. This relationship can be expressed as

$$W(\omega) = H(\omega)\, U(\omega) \tag{3.6}$$

where $W(\omega)$ is the vertical component, $U(\omega)$ is the horizontal component, and $H(\omega)$ is the transfer function. All of these functions are in the frequency domain, and in general, they are complex.

But $H(\omega)$ and $U(\omega)$ can be expressed in terms of their Fourier transforms. Therefore, equation 3.6 becomes

$$W(\omega) = \int_{-\infty}^{\infty} h(\tau)\, d\tau \int_{-\infty}^{\infty} u(\sigma)\, e^{i\omega\sigma}\, d\sigma \tag{3.7}$$

where $h(t)$ and $u(t)$ are real functions in the time domain.

This equation can be rearranged.

$$W(\omega) = \int_{-\infty}^{\infty} h(\tau) \int_{-\infty}^{\infty} u(\sigma)\, e^{i\omega(\sigma+\tau)}\, d\sigma\, d\tau \tag{3.8}$$

Now let $\sigma + \tau = t$. Then equation 3.8 becomes

$$W(\omega) = \int_{-\infty}^{\infty} h(\tau) \int_{-\infty}^{\infty} u(t-\tau) e^{i\omega t} dt d\tau \qquad (3.9)$$

Under certain conditions the order of integration can be changed. Then equation 3.9 becomes

$$W(\omega) = \int_{-\infty}^{\infty} \int_{-\infty}^{\infty} h(\tau) u(t-\tau) d\tau e^{i\omega t} dt \qquad (3.10)$$

But this is by definition the Fourier transform of $w(t)$. Therefore,

$$w(t) = \int_{-\infty}^{\infty} h(\tau) u(t-\tau) d\tau \qquad (3.11)$$

The final integral is called the convolution of $h(t)$ with $u(t)$. The convolution integral enables us to generate a time series of the vertical component of water-particle velocity directly from the time series of the horizontal component of water-particle velocity.

3.3 THE FOURIER TRANSFORM AND CONVOLUTION INTEGRAL

The Fourier transform and the convolution integral will be used in this paper to develop efficient algorithms for modeling ocean waves. For instance, the vertical attenuation and horizontal propagation of ocean waves can be modeled by Fourier transforms.

A time series represents a history of events at a single point in space. A time series can be transformed so that it represents another time series at the same point in space or at a different point in space. Some operations which do not "move" a time series of ocean waves in space include differentiation, integration, and Hilbert transforms. (A Hilbert transform is a phase shift of ninety-degrees in the frequency domain.) The operations which do "move" a time series through space include vertical attenuation and horizontal propagation.

A time series of the free-surface elevation will be convolved with transfer functions to generate time series of the dynamic water pressure, and the horizontal and vertical components of water-particle velocity and acceleration. Transfer functions will also be developed to model the vertical attenuation and horizontal propagation of ocean waves. The six time series that are required for a wave-force analysis will be known everywhere in space and they will be generated from one time series.

3.4 THE TIME AND WAVE-FREQUENCY DOMAIN

As the number of discrete waves N goes to infinity while the difference between neighboring wave frequencies and wave numbers goes to zero, the summation in equation 2.16 approaches its integral representation,

$$\eta = Re \frac{1}{2\pi} \int_{-\infty}^{\infty} A(\omega)\, e^{i(kx - \omega t)}\, d\omega \qquad (3.12)$$

where $A(\omega)$ is a complex amplitude which varies continuously with wave frequency and has a random phase. Equation 2.16 is a Fourier transform in the time and wave-frequency domain. As long as $A(\omega)$ has certain properties, we are now free to use the very powerful tools of Fourier transform analysis. Specifically, we will be most interested in the convolution of equation 3.12 with the inverse fourier transforms of transfer functions which we will develop in the frequency domain. Those transfer functions will be based on Airy wave theory.

3.5 THE SPACE AND WAVE-NUMBER DOMAIN

Equation 3.12 can alternatively be expressed as

$$\eta = Re \frac{1}{2\pi} \int_{-\infty}^{\infty} A(k)\, e^{i(kx - \omega t)}\, dk \qquad (3.13)$$

where $A(k)$ is a complex amplitude which varies continuously with wave number and has a random phase. Therefore, we can also express equation (2.16) as a Fourier transform in the space and wave-number domain. Both equations (3.12) and (3.13) have certain advantages and disadvantages.

The disadvantage of equation (3.13) is that its inverse Fourier transform requires an integration along the X-axis. Physically, this is a very difficult thing to do because it

would require many samples of the ocean wave along a straight line. However, this method is used to solve the Cauchy-Poisson problem. The advantage of equation (3.12) is that it represents the free-surface elevation at a single point in space. In the real world, wave-rider buoys have been doing this measurement for a long time. But this method does require long time records to model the horizontal propagation of irregular waves over long distances. However, time-domain analysis of offshore structures will not require us to simulate the propagation of irregular waves over long distances.

3.6 SUMMARY OF CHAPTER THREE

Given a time series of the free-surface elevation at one point in space, time series of water particle velocities and accelerations, and pressure can be generated at other points in space. The given time series can be either measured or simulated data. The generated time series can represent wave kinematics at points in a grid. During a time-domain simulation, the wave kinematics required by Morison's equation can be interpolated from the grid. The convolution integrals necessary to perform this analysis are usually more efficient than sum of sinusoids.

CHAPTER 4

TRANSFER FUNCTIONS FOR ANALYSIS OF OCEAN WAVES

4.1 EFFICIENT MODELING OF OCEAN WAVES

For very complicated offshore structures, calculating the wave kinematics at grid points is more efficient than calculating wave kinematics for every finite element. This would be especially true for offshore platforms. (However, for risers, it is probably more efficient to calculate the wave kinematics for every finite element instead of a mesh of points.) In particular, the methods of digital-signal processing are well-suited for a grid.

The coordinate system we will adopt for the grid is given in figure F.6. The X-axis is positive to the right, and the Z-axis is positive upwards. The number of grid points along the horizontal is ℓ, and the number along the vertical is d. The free-surface elevation at the upper-left corner of the grid is given. It is required to know the wave kinematics at every grid point at each time step.

To move from one grid point to another grid point parallel to the mean waterline will be called horizontal propagation. To move downward will be called vertical attenuation.

There are numerous ways to calculate time series of the wave kinematics at all grid points when the the free-surface elevation at one grid point is the only known time series. However, there are very few good methods. For instance, using one convolution integral to generate the time series of the horizontal-water particle acceleration at the bottom-right corner from the time series of the free-surface elevation at the origin is not very efficient. It is not very efficient because evaluating the convolution integral would require many multiplications and additions.

A far more efficient method is to do the convolution integral in steps. For instance, use an impulse response function that models horizontal propagation to move the free-surface elevation at the left side of the grid to the right side. This is a very good first step because the impulse response function that models horizontal propagation requires many sample points. It is best to do the the convolution integrals that require the most effort first. Even though the ultimate goal is to find the horizontal water-particle acceleration at the bottom-right corner, there are many time series that can be calculated at

intermediate steps. This is what makes this particular method so efficient. Now that the free-surface elevation is known at the right side of the grid, the horizontal water-particle velocity at the mean waterline can be found. The impulse response function that performs this operation requires fewer sample points than the impulse response function for horizontal propagation. Then use an impulse response function that models vertical attenuation to move the horizontal water-particle velocity at the mean waterline down to the bottom of the grid. This impulse response function requires very few sample points. To find the water-particle acceleration, differentiate the water-particle velocity with respect to time. This operation requires only two sample points. Therefore, in addition to calculating the horizontal water-particle at the bottom corner, three other time series were calculated at intermediate steps. Those three other time series were also required, and they can also be used to generate other time series within the same column of grid points. This is what makes this method much more efficient than using one impulse response function to do horizontal propagation, vertical attenuation, etc. Figures F.7 and F.8 give the algorithms used for generating time series in this paper.

4.2 THE TRANSFER FUNCTIONS IN DEEP WATER

The dispersion relation in deep water is

$$\omega^2 = kg \tag{4.1}$$

where ω is the wave frequency, k is the wave number, and g is the acceleration of gravity.

The transfer function for modeling horizontal propagation is

$$H(\omega) = e^{ik\Delta x} \tag{4.2}$$

where Δx is the distance propagated to the right. This transfer function is used to move the free-surface elevation at the origin horizontally.

The transfer function for modeling vertical attenuation is

$$H(\omega) = e^{|k|\Delta z} \tag{4.3}$$

where Δz is the negative distance below the mean waterline. This transfer function is used to find water-particle velocities and pressure below the mean waterline.

The transfer function for differentiation is

$$H(\omega) = i\omega \tag{4.4}$$

This transfer function is used to find the vertical

water-particle velocity on the mean waterline from the free-surface elevation. It is also used to convert water-particle velocities into accelerations.

The transfer function for converting the free-surface elevation into the horizontal water-particle velocity on the mean waterline is

$$H(\omega) = |\omega| \tag{4.5}$$

This transfer function is similiar to a differentiator, but it does not induce a phase shift.

4.3 THE TRANSFER FUNCTIONS IN WATER OF FINITE DEPTH

The transfer functions in water of finite depth are similiar to those in water of infinite depth. However, one major difference is the dispersion relation. The dispersion relation in water of finite depth is

$$\omega^2 = kg\tanh(kh) \tag{4.6}$$

where ω is the wave frequency, k is the wave number, g is the acceleration of gravity, and h is the water depth.

The transfer function for modeling horizontal propagation is

$$H(\omega) = e^{ik\Delta x} \tag{4.7}$$

where ΔX is the distance propagated to the right. It is a positive number. This transfer function is used move the free-surface elevation at the origin horizontally.

The transfer function for modeling vertical attenuation of the horizontal water-particle velocity and the dynamic pressure is

$$H(\omega) = \frac{\cosh(k(\Delta Z + h))}{\cosh(kh)} \tag{4.8}$$

where ΔZ is the negative distance below the mean waterline.

The transfer function for modeling vertical attenuation of the vertical water-particle velocity is

$$H(\omega) = \frac{\sinh(k(\Delta Z + h))}{\sinh(kh)} \tag{4.9}$$

The transfer function for differentiation is

$$H(\omega) = i\omega \tag{4.10}$$

This transfer function is used to find the vertical water-particle velocity on the mean waterline from the free-surface elevation. It is also used to convert water-particle velocities into accelerations.

The transfer function for converting the free-surface elevation into the horizontal water-particle velocity on the mean waterline is

$$H(\omega) = \frac{|\omega|}{\tanh(|K|h)} \qquad (4.11)$$

4.4 SUMMARY OF CHAPTER FOUR

An efficient algorithm for calculating wave kinematics in a grid has been discussed. The transfer functions in water of infinite and finite depth have been presented. The resulting impulse response functions will now be discussed in detail.

CHAPTER 5

DIFFERENTIATING TIME SERIES OF OCEAN WAVES

A time series of the free-surface elevation can be differentiated with respect to time to generate a time series of the vertical water particle velocity. This is true for both infinite and finite water depths. Physically, there is no justification for performing this operation. However, according to Airy wave theory differentiating the free-surface elevation with respect to time gives the vertical water-particle velocity. Similiarly, time series of the water particle accelerations can be generated from time series of the water particle velocities by differentiation with respect to time.

5.1 THEORY OF DIFFERENTIATION OF SINUSOIDAL WAVES

The equation for a sinusoidal wave in complex notation is

$$f(t) = e^{i\omega t} \tag{5.1}$$

where ω is the frequency and t represents time.

Differentiating this function with respect to time gives

$$f'(t) = i\omega e^{i\omega t} \tag{5.2}$$

where $f'(t)$ is the first derivative of $f(t)$.

In this manner, time series of the vertical water-particle velocity on the mean waterline can be generated from time series of the free-surface elevation. Similiarly, the horizontal and vertical water-particle accelerations can be generated from the horizontal and vertical water-particle velocities respectively.

5.2 NUMERICAL DIFFERENTIATION OF SINUSOIDAL WAVES

The approximate derivative of $f(t)$ as given by the central difference method is

$$f'(t) \sim \frac{f(t+\Delta t) - f(t-\Delta t)}{2\Delta t} \tag{5.3}$$

where Δt is the time step and n is an index.

As discussed in appendix A, there are two types of errors associated with this approximation. The first type of error is due to truncation. The truncation error is reduced by taking smaller time steps or by using a higher order differentiator. The second type of error is due to

roundoff or noise. This type of error is best eliminated by a filter. Furthermore, this method becomes less accurate as the number of sample ponts per wave is reduced.

5.3 SUMMARY OF CHAPTER FIVE

Numerical differentiation is a very efficient method for generating time series. However, it must be used carefully because it does amplify noise.

CHAPTER 6

THE HORIZONTAL WATER-PARTICLE VELOCITY

A time series of the free-surface elevation can be differentated with respect to time to generate a time series of the vertical water-particle velocity on the mean waterline. This is true in water of either infinite or finite depth. A time series of the horizontal water-particle velocity can be generated in a similiar manner.

6.1 HORIZONTAL WATER-PARTICLE VELOCITY - DEEP WATER

The dispersion relation in deep water is

$$\omega^2 = kg \tag{6.1}$$

where ω is the wave frequency, k is the wave number, and g is the acceleration of gravity.

The transfer function for converting the free-surface elevation into the horizontal water-particle velocity on the mean waterline is

$$H(\omega) = |\omega| \tag{6.2}$$

This transfer function does not have a Fourier transform, but it does have a fourier series. The coefficients of the impulse response function have been derived in appendix B, equation B.6.

$$h(n\Delta t) = \begin{cases} \frac{\pi}{2\Delta t^2} & \text{zero} \\ 0. \quad \text{for} \quad n & \text{even} \\ \frac{-2}{\pi (n\Delta t)^2} & \text{odd} \end{cases} \tag{6.3}$$

where Δt is the time step.

A plot of this function is given in figure F.9. It is a symmetric function which rapidly approaches zero as the time becomes large. In fact, the coefficients of the impulse response function are inversely proportional to the square of time.

When the convolution integral is evaluated numerically, the range of integration should not extend beyond the time when the amplitude of the impulse response function becomes less than a certain tolerance. The time at which this function is less than a certain tolerance is

$$T \geq \frac{2\Delta t}{\pi} \frac{1}{\sqrt{\theta}} \tag{6.4}$$

where θ is a fraction of $h/(n\Delta t)$ at $n=0$.

The corresponding number of sample points is

$$n \geq \frac{2}{\pi} \frac{1}{\sqrt{\theta}} \tag{6.5}$$

where $T = n\Delta t$.

6.2 HORIZONTAL WATER-PARTICLE VELOCITY - FINITE DEPTH

The dispersion relation in water of finite depth is

$$\omega^2 = kg \tanh(kh) \tag{6.6}$$

where ω is the wave frequency, k is the wave number, g is the acceleration of gravity, and h is the water depth.

The transfer function for converting the free-surface elevation into the horizontal water-particle velocity on the mean waterline is

$$H(\omega) = \frac{|\omega|}{\tanh(|k|h)} \tag{6.7}$$

This function does not have a Fourier transform, but it does have a Fourier series. But even the Fourier series solution cannot be expressed in terms of elementary

functions. However, the fast Fourier transform can be used to evaluate the Fourier coefficients. Figure F.10 compares the impulse response functions for infinite and finite water depths. Even though the water depth is very shallow, the two functions are very similiar. Therefore, the behaviour of the function for infinite water depth case can be used to size the function for the finite water depth case.

6.3 SUMMARY OF CHAPTER SIX

The impulse response function for transforming a time series of the free-surface elevation into a time series of the horizontal water-particle velocity on the mean waterline in deep water has been derived. The impulse response function for water of finite depth must be evaluated numerically. However, the theoretical solution for deep water can be used to size the numerical solution for water of finite depth.

CHAPTER 7

THE VERTICAL-ATTENUATION PROBLEM

A point far below the free surface does not feel a wave's disturbance as much as a point near the free surface. This phenomenon is called vertical attenuation. According to Airy wave theory, the vertical attenuation of waves varies exponentially as a function of the distance from the free surface.

7.1 VERTICAL ATTENUATION IN DEEP WATER

The dispersion relation in deep water is

$$\omega^2 = kg \tag{7.1}$$

where ω is the wave frequency, k is the wave number, and g is the acceleration of gravity.

The transfer function for vertical attenuation in deep water is

$$H(\omega) = e^{k/\Delta z} \tag{7.2}$$

where Δz is the negative distance below the mean waterline.

The inverse Fourier transform of this transfer function has been derived in appendix C, equation C.15.

$$h(t) = \frac{1}{2}\sqrt{\frac{-g}{\pi \Delta z}}\ \exp\left(\frac{g t^2}{4 \Delta z}\right) \tag{7.3}$$

A plot of this function is given in figure F.11. It is a symmetric function which rapidly approaches zero as the time becomes large. In fact, the function converges exponentially.

When the convolution integral is evaluated numerically, the range of integration should not extend beyond the time when the amplitude of the function in equation 7.3 becomes less than a certain tolerance. The time at which this function is less than a certain tolerance is

$$|T| \geq 2\sqrt{\frac{\Delta z \ln \theta}{g}} \tag{7.4}$$

where θ is a fraction of the value of $h(t)$ at $t = 0$.

The corresponding number of sample points is

$$|n| \geq \frac{2}{\Delta t}\sqrt{\frac{\Delta z \ln \theta}{g}} \tag{7.5}$$

where $T = n \Delta t$.

7.2 VERTICAL ATTENUATION IN WATER OF FINITE DEPTH

The dispersion relation in water of finite depth is

$$\omega^2 = kg \tanh(kh) \tag{7.6}$$

where ω is the wave frequency, k is the wave number, g is the acceleration of gravity, and h is the water depth.

The transfer functions for vertical attenuation in water of finite depth are

$$H_1(\omega) = \frac{\cosh(k(z+h))}{\cosh(kh)}$$

$$H_2(\omega) = \frac{\sinh(k(z+h))}{\sinh(kh)} \tag{7.7}$$

where the first transfer function models the vertical attenuation of the dynamic pressure, and the horizontal water-paticle velocity and acceleration. The second transfer function models the vertical attenuation of the vertical water-particle velocity and acceleration. These transfer functions cannot be expressed in terms of elementary functions. However, the fast Fourier transform can be used to evaluate their inverse Fourier transforms. Figure F.12 compares the impulse response functions for infinite and finite water depths. Even though the water depth is very shallow in these examples, the two functions are very similiar. Therefore, the behaviour of the function

for attenuation in deep water case can be used to size the impulse response functions for the finite water depth case.

7.3 SUMMARY OF CHAPTER SEVEN

The inverse Fourier transform for vertical attenuation in deep water has been derived. The impulse response functions for water of finite depth must be evaluated numerically. However, the theoretical solution for deep water can be used to size the numerical solutions for water of finite depth.

CHAPTER 8

THE HORIZONTAL-PROPAGATION PROBLEM

A single wave moves horizontally at a rate equal to its phase velocity. A wave's phase velocity is a function of the wave's frequency and the water depth. This phenomenon is called dispersion. The front of a wave group moves at a rate equal to its group velocity. For waves traveling over short distances, the phase velocity is a good measure of a wave's speed. (The model proposed in this paper does not simulate group effects.) Given a time history of the free-surface elevation at a point in space, the free-surface elevation at neighboring points can be found by convolving the original time series with the impulse response function of the appropiate transfer function.

8.1 HORIZONTAL PROPAGATION IN DEEP WATER

The dispersion relation in deep water is

$$\omega^2 = kg \tag{8.1}$$

where ω is the wave frequency, κ is the wave number, and g is the acceleration of gravity.

The transfer function for horizontal propagation in deep water is

$$H(\omega) = e^{i\kappa\Delta x} \tag{8.2}$$

where Δx is the positive distance propagated.

The inverse Fourier transform of this transfer function has been derived in appendix D, equation D.10.

$$h(t) = \sqrt{\frac{g}{2\pi\Delta x}}\left[\left(\frac{1}{2} + C\left(\sqrt{\frac{g}{2\pi\Delta x}}\,t\right)\right)\cos\left(\frac{gt^2}{4\Delta x}\right) + \left(\frac{1}{2} + S\left(\sqrt{\frac{g}{2\pi\Delta x}}\,t\right)\right)\sin\left(\frac{gt^2}{4\Delta x}\right)\right] \tag{8.3}$$

where $C(y)$ and $S(y)$ are the cosine and sine Fresnel integrals.

Figure F.13 shows that for this function the period of oscillation becomes smaller while the amplitude of oscillation remains constant as the time goes to positive infinity. As time goes to negative infinity, the function approaches zero very rapidly. The method of asymptotics will now be used to explain these phenomena.

The cosine and sine Fresnel integrals approach 0.5 as their arguments go to infinity. Therefore,

$$h(t) \rightarrow \sqrt{\frac{g}{\pi \Delta x}} \cos\left(\frac{g t^2}{4 \Delta x} - \frac{\pi}{4}\right) \text{ as } \sqrt{\frac{g}{2\pi \Delta x}}\, t \rightarrow +\infty \qquad (8.4)$$

The amplitude of oscillation is constant and the period of oscillation becomes smaller because of the the argument of the cosine function is an nonlinear function of time. This is in agreement with figure F.13.

In fact, if one is given the apparent period of oscillation, the time at which it occurs is given by

$$\frac{g(T_+ + T_A)}{4\Delta x} - \frac{g T_+^2}{4 \Delta x} = 2\pi \qquad (8.5)$$

where T_A is the apparent period.

Now solve for the time in terms of the apparent period.

$$T_+ = \frac{4\pi \Delta x}{g T_A} - \frac{T_A}{2} \qquad (8.6)$$

In particular, if the apparent period is chosen as $2\Delta t$ which is the period of ocillation of a wave sampled at the nyquist rate, equation 8.5 becomes

$$T_+ = \frac{2\pi \Delta x}{g \Delta t} - \Delta t \qquad (8.7)$$

Therefore, the time at which the apparent period equals $2\Delta t$ is directly proportional to the distance propagated and inversely proportional to the time step. As

the distance of propagation increases, the amount of effort required to evaluate the convolution integral increases linearly. For very large distances, the effort required to evaluate the convolution integral could become enormous. But this particular model is not meant for simulating the propagation of waves over large distances. For very large distances wave group effects would become important.

When the convolution integral for horizontal propagation is evaluated numerically, the range of integration for positive time should not extend beyond the time when the apparent period equals two times the time step. Therefore, the number of sample points of the impulse response function for positive time is

$$n_+ \geq \frac{2\pi\Delta x}{g\Delta t^2} - 1 \tag{8.8}$$

where $T_+ = n_+ \Delta t$.

Since the first term is much greater than one,

$$n_+ \approx \frac{2\pi\Delta x}{g\Delta t^2} \tag{8.9}$$

For negative arguments, the cosine and sine Fresnel integrals behave like

$$C(z) = -\frac{1}{2} - f(z)\sin\left(\frac{\pi}{2}z^2\right) + g(z)\cos\left(\frac{\pi}{2}z^2\right)$$
$$S(z) = -\frac{1}{2} + f(z)\cos\left(\frac{\pi}{2}z^2\right) + g(z)\sin\left(\frac{\pi}{2}z^2\right) \tag{8.10}$$

where the functions $f(z)$ and $g(z)$ are defined in chapter seven of Abramowitz and Stegun.

As time goes to negative infinity the cosine and sine Fresnel integrals approach -0.5. The leading order behaviour of equation 8.3 is

$$h(t) \rightarrow -\frac{2\Delta x}{\pi g t^3} \quad as \quad \sqrt{\frac{g}{2\pi\Delta x}}\, t \longrightarrow -\infty \qquad (8.11)$$

Therefore, the amplitude of the function is directly proportional to the distance propagated and inversely proportional to the time cubed.

When the convolution integral is evaluated numerically, the range of integration for negative time should not extend beyond the time when the amplitude of the impulse response function becomes less than a certain tolerance. The time at which this function is less than a certain tolerance is

$$T_- \leq -\left(\frac{32}{\theta^2\pi}\right)^{1/6}\left(\frac{\Delta x}{g}\right)^{1/2} \qquad (8.12)$$

where θ is a fraction of the value of $h(t)$ at $t=0$.

The corresponding number of sample points is

$$n_- \geq \left(\frac{32}{\theta^2\pi}\right)^{1/6}\left(\frac{\Delta x}{g}\right)^{1/2}\frac{1}{\Delta t} \qquad (8.13)$$

where $T_- = -n_- \Delta t$.

Equations 8.9 and 8.12 are very useful for evaluating the convolution integral when the inverse Fourier transform is given by equation 8.3. However, equation 8.3 is only applicable when the cut-off frequency is infinite. But the impulse response function for finite depth will be evaluated numerically. Its cut-off frequency will be finite. For deep water, the inverse Fourier transform of equation 8.2 for a finite cut-off frequency is (equation D.11)

$$h(t)=\sqrt{\frac{g}{2\pi\Delta x}}\left[\left(C\left(\sqrt{\frac{2\Delta x}{\pi g}}\,\omega_c-\sqrt{\frac{g}{2\pi\Delta x}}\,t\right)+C\left(\sqrt{\frac{g}{2\pi\Delta x}}\,t\right)\right)\cos\left(\frac{gt^2}{4\Delta x}\right)\right.$$
$$\left.+\left(S\left(\sqrt{\frac{2\Delta x}{\pi g}}\,\omega_c-\sqrt{\frac{g}{2\pi\Delta x}}\,t\right)+S\left(\sqrt{\frac{g}{2\pi\Delta x}}\,t\right)\right)\sin\left(\frac{gt^2}{4\Delta x}\right)\right] \qquad (8.14)$$

where ω_c is the cut-off frequency.

Figure F.14 shows that the behaviour of this function is quite different from the function plotted in figure F.13. As the time goes to positive infinity the function approaches zero. If the time at which the function goes to zero is less than the time at which the apparent period equals $2\Delta t$, the convolution integral will give incorrect results. The function goes to zero when the argument of the cosine and sine Fresnel integrals changes sign.

$$T_o = \frac{2\Delta x}{g}\omega_c \qquad (8.15)$$

where T_o represents the time at which the function approaches zero.

When the Fast Fourier trnasform is used to evaluate the impulse response function,

$$\omega_c = \frac{\pi}{\Delta t} \tag{8.16}$$

Therefore,

$$T_o = \frac{2\pi\Delta X}{g\Delta t} \tag{8.17}$$

Consequently, T_o and T_t are equal, and the error caused by the finite cut-off frequency affects the convolution integral very little.

8.2 HORIZONTAL PROPAGATION IN WATER OF FINITE DEPTH

The dispersion relation in water of finite depth is

$$\omega^2 = kg\tanh(Kh) \tag{8.18}$$

where ω is the wave frequency, K is the wave number, g is the acceleration of gravity, and h is the water depth.

The transfer function for horizontal propagation in water of finite depth is

$$H(\omega) = e^{iK\Delta X} \tag{8.19}$$

where ΔX is the positive distance propagated.

This inverse Fourier transform does not have a solution in closed form. However, the fast Fourier transform can be used to evaluate it. Figure F.15 compares the impulse response functions for infinite and finite water depths. Even though the water depth is very shallow, the two functions are very similiar. At shallower water depths, Airy wave theory would not be valid. Therefore, the asymptotic analysis performed for the deep water case can be used to size the impulse response function for the finite water depth case.

8.3 SUMMARY OF CHAPTER EIGHT

An aysmptotic analysis has been made of the inverse Fourier transforms of the transfer functions for performing horizontal propagation. The function for deep water has a closed form solution. The impulse response function for water of finite depth must be evaluated numerically. However, the theoretical solution for deep water can be used to size the numerical solution for water of finite depth.

CHAPTER 9

CONCLUSIONS

An alternative to sum of sinusoids has been presented. Instead of a discrete sum of sinusoids, the Fourier transform and convolution integrals are used to represent a continuous distribution of sinusoids. In some cases the method proposed in this paper is much faster than sum of sinusoids.

9.1 LIMITATIONS OF THE PROPOSED METHOD

The proposed model of ocean waves is linear. It will not model wave breaking and other nonlinear phenomena. Wave grouping is also not modeled. The proposed method could be used to simulate wave spreading, but it would require assembling many two-dimensional problems. The proposed method is not good for propagating waves over large distances. Sum of sinusoids also has these same limitations. For risers, the proposed method for simulating

ocean waves may not be very efficient because the wave kinematics would be evaluated at too many points. Sum of sinusoids would probably be more efficient because the wave kinematics could be evaluated at fewer points.

9.2 ADVANTAGES OF THE PROPOSED METHOD

Unlike sum of sinusoids, the proposed model of ocean waves gives an continuous distribution of wave energy. In fact, data taken from a waver-rider buoy can be used directly. Alternatively, data generated by an ARMA model can be used. For very complex offshore structures that would require the wave kinematics at many points in a grid, the proposed method is much more efficient than sum of sinusoids. Figures F.16 and F.17 show a comparison of the two methods for different size grids and for different numbers of discrete waves used by sum of sinusoids. For very large problems, the proposed method is significantly faster than sum of sinusoids. Typically, the proposed method is ten to twenty times faster than sum of sinusoids.

APPENDIX A

DIFFERENTIATION

Differentiation with respect to time is used to generate time series of the vertical water-particle velocity and acceleration, and the horizontal water-particle acceleration. The differentiation is done by using the central difference method. Whenever differentiation is performed numerically, the accuracy and noise amplification should be carefully investigated. The central difference method is

$$f'(t) \sim \frac{f(t+\Delta t) - f(t-\Delta t)}{2\Delta t} \qquad \text{(A.1)}$$

where $f'(t)$ is the derivative of the function $f(t)$ at time t. Δt is the time step.

If $f(t+\Delta t)$ and $f(t-\Delta t)$ are expanded in a Taylor series, the truncation error can be found. Then

$$f'(t) = \frac{f(t+\Delta t) - f(t-\Delta t)}{2\Delta t} - \frac{\Delta t^2}{6} f^{(3)}(\xi) \qquad \text{(A.2)}$$

where $f^{(3)}(\xi)$ is the third derivative of $f(t)$ evaluated

anywhere in the interval from $t-\Delta t$ to $t+\Delta t$.

Therefore, the truncation error is inversely proportional to the square of the time step. Furthermore, functions which do not have smooth second derivatives will have first derivatives that are not well predicted by the central difference method.

In particular, let us investigate the accuracy of the central difference method when it is applied to sinusoidal functions. Suppose the sinusoidal function is given by

$$f(t) = e^{i\omega t} \tag{A.3}$$

where ω is the frequency. Then the derivative of this function is simply

$$f'(t) = i\omega e^{i\omega t} \tag{A.4}$$

where the above equation is exact.

The approximate derivative as given by the central difference method is

$$f'(t) \sim \frac{e^{i\omega(t+\Delta t)} - e^{i\omega(t-\Delta t)}}{2\Delta t} \tag{A.5}$$

This can be expressed as

$$f'(t) \sim \frac{i\sin(\omega\Delta t)\, e^{i\omega t}}{\Delta t} \tag{A.6}$$

Now calculate the ratio of the approximate derivative to the exact derivative

$$R(\omega) = \frac{\sin(\omega\Delta t)}{\omega\Delta t} \qquad \text{(A.7)}$$

where $R(\omega)$ is the relative error. When $R(\omega)$ equals one, the approximate solution is exact. As ω approaches zero, the central difference method becomes a very poor approximation.

The relative error is plotted in figure F.18. There is no error as the frequency goes to zero. But as the frequency approaches two samples per wave period, the relative error goes to zero. This is called the nyquist rate. In theory, the highest wave frequency that can be modeled by the methods of digital-signal processing is the nyquist frequency. In practice, the sampling rate should never become lower than eight samples per wave period.

The derivative of a function contaminated with noise can have very large errors. In fact, the error can go up as the time step decreases. For instance, suppose $f(t+\Delta t)$ and $f(t-\Delta t)$ are contaminated with noise. Then

$$\begin{aligned} f(t+\Delta t) &= \tilde{f}(t+\Delta t) + n(t+\Delta t) \\ f(t-\Delta t) &= \tilde{f}(t-\Delta t) + n(t-\Delta t) \end{aligned} \qquad \text{(A.8)}$$

where $n(t+\Delta t)$ and $n(t-\Delta t)$ represent noise. The formula for the first derivative then becomes

$$f'(t) = \frac{\tilde{f}(t+\Delta t) - \hat{f}(t-\Delta t)}{2\Delta t} + \frac{n(t+\Delta t) - n(t-\Delta t)}{2\Delta t} \qquad \text{(A.9)}$$

$$-\frac{\Delta t^2}{6} f^{(3)}(\xi)$$

Therefore, noise leads to an error in the derivative that is inversely proportional to the time step. (Figures F.19, F.20 and F.21 show a time series contaminated with noise and the derivative that time series for two different time steps.) For the second derivative, the additional error term would be inversely proportional to the square of the time step. This is a very undesireable phenomenon. However, there are two relatively easy ways of avoiding this problem. The first way is to filter the noise out of the original time series and then differentiate. The second way is to create a differentiator that removes the noise as it differentiates. Of the two methods, the first method is more desireable for our purposes because it only requires that the preventive measures be taken only once.

APPENDIX B

THE HORIZONTAL WATER-PARTICLE VELOCITY

The free-surface elevation convolved with an impulse response function gives the horizontal water-particle velocity on the mean waterline. The convolution integral has the following form:

$$u(t) = \int_{-\infty}^{\infty} h(\tau)\,\eta(t-\tau)\,d\tau \qquad \text{(B.1)}$$

where $u(t)$ represents the time series of the horizontal water-particle velocity, $\eta(t)$ represents the time series of the free-surface elevation, and $h(t)$ is the inverse Fourier transform of the transfer function. In fact, the inverse Fourier transform is not defined. However, the Fourier series solution does exist.

This integral can be evaluated numerically as

$$u(m\Delta t) = \sum_{n=-\infty}^{\infty} h(n\Delta t)\,\eta(m\Delta t - n\Delta t)\,\Delta t \qquad \text{(B.2)}$$

where Δt is the time step, and m and n are indices. $u(t)$ and $\eta(t)$ are both sinusoidal functions of time. In

fact, in deep water $u(t)$ and $\eta(t)$ can be expressed as

$$u(t) = |\omega| e^{i\omega t}$$
$$\eta(t) = e^{i\omega t} \qquad \text{(B.3)}$$

where ω represents the frequency of the sinusoid.

Now equation B.2 can be expressed as

$$|\omega| e^{im\Delta t\omega} = \sum_{n=-\infty}^{\infty} h(n\Delta t)\, e^{i(m\Delta t\omega - n\Delta t\omega)}\, \Delta t \qquad \text{(B.4)}$$

But the above equation is a complex fourier series. Therefore,

$$h(n\Delta t) = \frac{1}{2\pi} \int_{-\pi/\Delta t}^{\pi/\Delta t} |\omega| e^{in\Delta t\omega}\, d\omega \qquad \text{(B.5)}$$

The evaluation of this integral gives

$$h(n\Delta t) = \begin{cases} \dfrac{\pi}{2\Delta t^2} & \text{zero} \\ 0. \quad \text{for } n & \text{even} \\ \dfrac{-2}{\pi (n\Delta t)^2} & \text{odd} \end{cases} \qquad \text{(B.6)}$$

It is now clear that the impulse response function is inversely proportional to the square of time. This is a more rapid convergence rate than some other alternatives that could have been used to generate time series of the horizontal water-particle velocity on the mean waterline. For instance, a Hilbert transform could have been used to transform the vertical water-particle velocity into the

horizontal. But the Hilbert transform is only inversely proportional to time.

APPENDIX C

VERTICAL ATTENUATION

For very deep water, the transfer function in the frequency domain is

$$H(\omega) = \exp(|K|\Delta Z) \tag{C.1}$$

where ω is the wave frequency, K is the wave number, and ΔZ is the change in water depth (measured positive upwards). Since the transfer function is a real and symmetric function of frequency, the impulse response function will be a real and symmetric function of time. The inverse Fourier transform of the transfer function is given by

$$h(t) = \frac{1}{2\pi} \int_{-\infty}^{\infty} \exp\left(\frac{\omega^2 \Delta Z}{g}\right) e^{i\omega t} d\omega \tag{C.2}$$

where t represents time. The dispersion relation for infinite water depth has been substituted for K.

As expected, the imaginary part of the integrand is an odd function of frequency, and it will not make a contribution to the inverse Fourier transform. The Fourier transform can now be expressed as

$$h(t) = \frac{1}{\pi}\int_{-\infty}^{\infty} \exp\left(\frac{\omega^2 \Delta z}{g}\right)\cos(\omega t)\,d\omega \qquad \text{(C.3)}$$

Now integrate by parts.

$$h(t) = \frac{1}{\pi}\exp\left(\frac{\omega^2 \Delta z}{g}\right)\frac{\sin(\omega t)}{t}\Bigg|_0^{\infty}$$

$$-\frac{2}{\pi}\frac{\Delta z}{gt}\int_0^{\infty} \omega \exp\left(\frac{\omega^2 \Delta z}{g}\right)\sin(\omega t)\,d\omega \qquad \text{(C.4)}$$

Since the first term is zero,

$$h(t) = -\frac{2}{\pi}\frac{\Delta z}{gt}\int_0^{\infty} \omega \exp\left(\frac{\omega^2 \Delta z}{g}\right)\sin(\omega t)\,d\omega \qquad \text{(C.5)}$$

The derivative with respect to time of equation C.3 gives

$$h'(t) = -\frac{1}{\pi}\int_0^{\infty} \omega \exp\left(\frac{\omega^2 \Delta z}{g}\right)\sin(\omega t)\,d\omega \qquad \text{(C.6)}$$

Therefore, the impulse response function and its derivative are related to each other as follows:

$$h'(t) = \frac{gt}{2\Delta z}\,h(t) \qquad \text{(C.7)}$$

Integrate this expression with respect to time.

$$h(t) = C \exp\left(\frac{g t^2}{4\Delta z}\right) \tag{C.8}$$

where C is a constant of integration.

To find the constant of integration, evaluate $h(t)$ at $t=0$. Therefore,

$$C = h(0) = \frac{1}{\pi} \int_0^\infty \exp\left(\frac{\omega^2 \Delta z}{g}\right) d\omega \tag{C.9}$$

A change of variables gives

$$C = \frac{1}{\pi}\sqrt{\frac{-g}{\Delta z}} \int_0^\infty \exp(-u^2)\, du \tag{C.10}$$

The square of this integral is

$$C^2 = \frac{-g}{\pi^2 \Delta z} \int_0^\infty \exp(-u^2)\, du \int_0^\infty \exp(-w^2)\, dw \tag{C.11}$$

This quantity can be expressed as

$$C^2 = \frac{-g}{\pi^2 \Delta z} \int_0^\infty \int_0^\infty \exp(-(u^2+w^2))\, du\, dw \tag{C.12}$$

Now introduce polar coordinates.

$$C^2 = \frac{-g}{\pi^2 \Delta z} \int_0^\infty \int_0^{\pi/2} r \exp(-r^2)\, d\theta\, dr \tag{C.13}$$

Therefore, the constant of integration is

$$C = \frac{1}{2}\sqrt{\frac{-g}{\pi \Delta z}} \tag{C.14}$$

Furthermore, the final expression for the impulse response function is

$$h(t) = \frac{1}{2}\sqrt{\frac{-g}{\pi \Delta z}}\, exp\left(\frac{g t^2}{4 \Delta z}\right) \tag{C.15}$$

APPENDIX D

HORIZONTAL PROPAGATION

For very deep water, the transfer function in the frequency domain is

$$H(\omega) = \exp(ik\Delta X) \tag{D.1}$$

where ω is the wave frequency, k is the wave number, and ΔX is a positive distance over which a wave is going to be propagated. Since the real part of the transfer function is even and the imaginary part is odd, the impulse response function will be a real function of time. The inverse Fourier transform of the transfer function is give by

$$h(t) = \frac{1}{2\pi}\int_{-\infty}^{\infty}\left[\cos\left(\frac{\omega^2 \operatorname{sgn}(\omega)\Delta X}{g}\right) - i\sin\left(\frac{\omega^2 \operatorname{sgn}(\omega)\Delta X}{g}\right)\right]e^{i\omega t}\,d\omega \tag{D.2}$$

where t represents time. The dispersion relation for infinite water depth has been substituted for k.

The integrand can be expanded as

$$h(t) = \frac{1}{2\pi}\int_{-\infty}^{\infty}\left[\cos\left(\frac{\omega^2 \operatorname{sgn}(\omega)\Delta X}{g}\right)\cos\omega t + i\cos\left(\frac{\omega^2 \operatorname{sgn}(\omega)\Delta X}{g}\right)\sin\omega t\right.$$

$$\left. -i\sin\left(\frac{\omega^2 \operatorname{sgn}(\omega)\Delta X}{g}\right)\cos\omega t + \sin\left(\frac{\omega^2 \operatorname{sgn}(\omega)\Delta X}{g}\right)\sin\omega t\right]d\omega \tag{D.3}$$

As expected, the imaginary part of the integrand is an odd function of frequency, and it will not make a contribution to the inverse Fourier transform. The Fourier transform can now be expressed as

$$h(t)=\frac{1}{\pi}\int_{-\infty}^{\infty}\cos\left(\frac{\omega^2 \Delta X}{g}-\omega t\right)d\omega \tag{D.4}$$

This integral is similiar to the indefinite integral given below.

$$I(x)=\int \cos(ax^2+2bx+c)\,dx \tag{D.5}$$

This integral can be arranged as

$$I(x)=\int \cos\left(\frac{(ax+b)^2}{a}-\frac{(b^2-ac)}{a}\right)dx \tag{D.6}$$

The expansion of the integral is

$$I(x)=\int\left[\cos\left(\frac{(ax+b)^2}{a}\right)\cos\left(\frac{(b^2-ac)}{a}\right)+\sin\left(\frac{(ax+b)^2}{a}\right)\sin\left(\frac{(b^2-ac)}{a}\right)\right]dx \tag{D.7}$$

This integral can be expressed as

$$I(x)=\sqrt{\frac{\pi}{2a}}\int\left[\sqrt{\frac{2a}{\pi}}\cos\left(\frac{\pi}{2}\left(\sqrt{\frac{2}{a\pi}}(ax+b)\right)^2\right)\cos\left(\frac{(b^2-ac)}{a}\right)+\sqrt{\frac{2a}{\pi}}\sin\left(\frac{\pi}{2}\left(\sqrt{\frac{2}{a\pi}}(ax+b)\right)^2\right)\sin\left(\frac{(b^2-ac)}{a}\right)\right]dx \tag{D.8}$$

Now express this integral in terms of Fresnel integrals.

$$I(x)=\sqrt{\frac{\pi}{2a}}\left[C\left(\sqrt{\frac{2}{a\pi}}(ax+b)\right)\cos\left(\frac{(b^2-ac)}{a}\right)+S\left(\sqrt{\frac{2}{a\pi}}(ax+b)\right)\sin\left(\frac{(b^2-ac)}{a}\right)\right] \tag{D.9}$$

where $C(y)$ and $S(y)$ are defined as $\int_0^y \cos(\frac{\pi}{2}t^2)dt$ and $\int_0^y \sin(\frac{\pi}{2}t^2)dt$ respectively.

Therefore, the integral for $h(t)$ can be expressed as

$$h(t)=\sqrt{\frac{g}{2\pi\Delta x}}\left[\left(\frac{1}{2}+C\left(\sqrt{\frac{g}{2\pi\Delta x}}t\right)\right)\cos\left(\frac{gt^2}{4\Delta x}\right)+\left(\frac{1}{2}+S\left(\sqrt{\frac{g}{2\pi\Delta x}}t\right)\right)\sin\left(\frac{gt^2}{4\Delta x}\right)\right] \tag{D.10}$$

For finite cut-off frequencies, $h(t)$ can be expressed as

$$h(t)=\sqrt{\frac{g}{2\pi\Delta x}}\left[\left(C\left(\sqrt{\frac{2\Delta x}{\pi g}}\omega_c-\sqrt{\frac{g}{2\pi\Delta x}}t\right)+C\left(\sqrt{\frac{g}{2\pi\Delta x}}t\right)\right)\cos\left(\frac{gt^2}{4\Delta x}\right)+\left(S\left(\sqrt{\frac{2\Delta x}{\pi g}}\omega_c-\sqrt{\frac{g}{2\pi\Delta x}}t\right)+S\left(\sqrt{\frac{g}{2\pi\Delta x}}t\right)\right)\sin\left(\frac{gt^2}{4\Delta x}\right)\right] \tag{D.11}$$

where ω_c is the cut-off frequency. This expression is useful for comparing theory to numerical results generated by the fast Fourier transform.

APPENDIX E

BIBLIOGRAPHY

Abramowitz, M. and Stegun, I.A. 1965. Handbook of Mathematical Functions. Dover, New York.

Burke, Ben G. and Tighe, James T. 1972. "A Time Series Model for Dynamic Behavior of Offshore Structures," Society of Petroleum Engineers Journal, 156-170.

Fuchs, R.A. 1954. "On the Theory of Irregular Waves," Proceedings of the First Conference on Ships and Waves, SNAME, 1-10.

Le Mehaute, B. 1969. "An Introduction to Hydrodynamics and Water Waves - Volume II: Water Wave Theories," ESSA Technical Report ERL 118-pol 3-2, U.S. Government Printing Office.

Zienkiewicz, O.C., Lewis, R.W., and Stagg, K.G. 1978. Numerical Methods in Offshore Engineering, John Wiley and Sons, New York.

APPENDIX F

FIGURES

F.1 TYPICAL OFFSHORE STRUCTURES

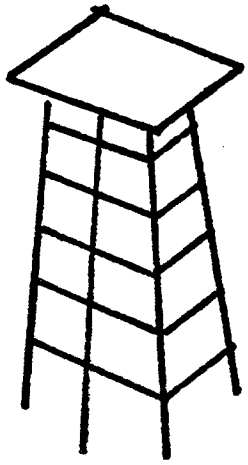

GRAVITY PLATFORM

RISER

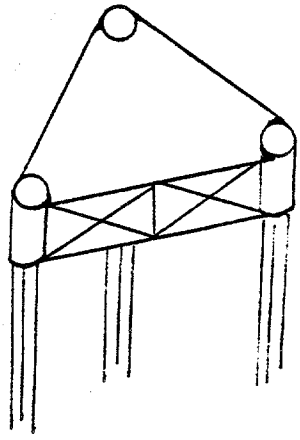

TENSION-LEG PLATFORM

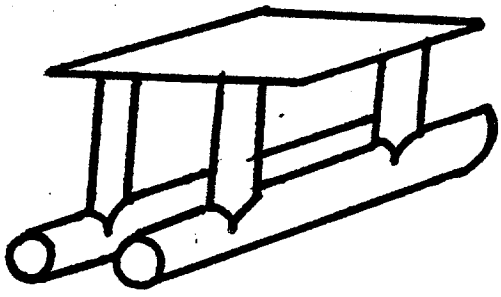

SEMISUBMERSIBLE

F.2 FLOW NORMAL TO A CYLINDER'S AXIS

This figure shows how Morison's equation is applied for flow normal to a cylinder's axis.

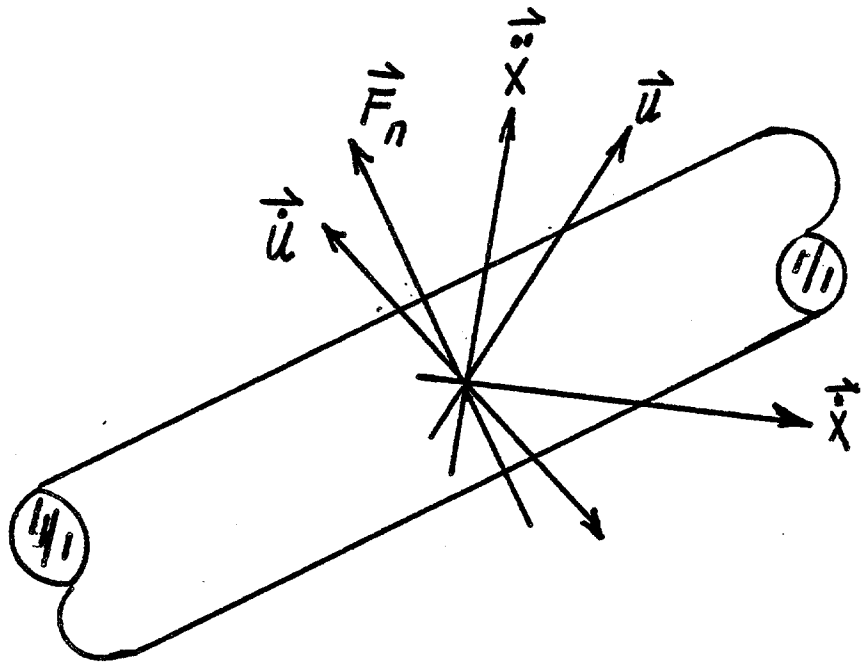

F.3 FLOW IN-LINE WITH A CYLINDER'S AXIS

This figure shows how Morison's equation is applied for flow in-line with a cylinder's axis.

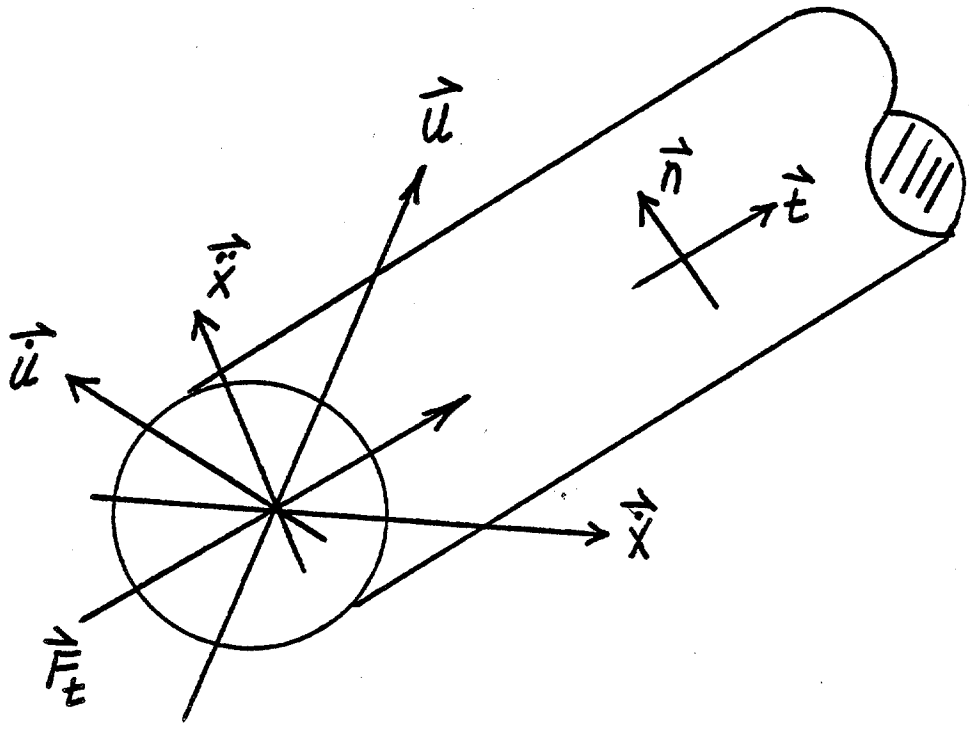

F.4 COORDINATE SYSTEM FOR AIRY WAVE THEORY

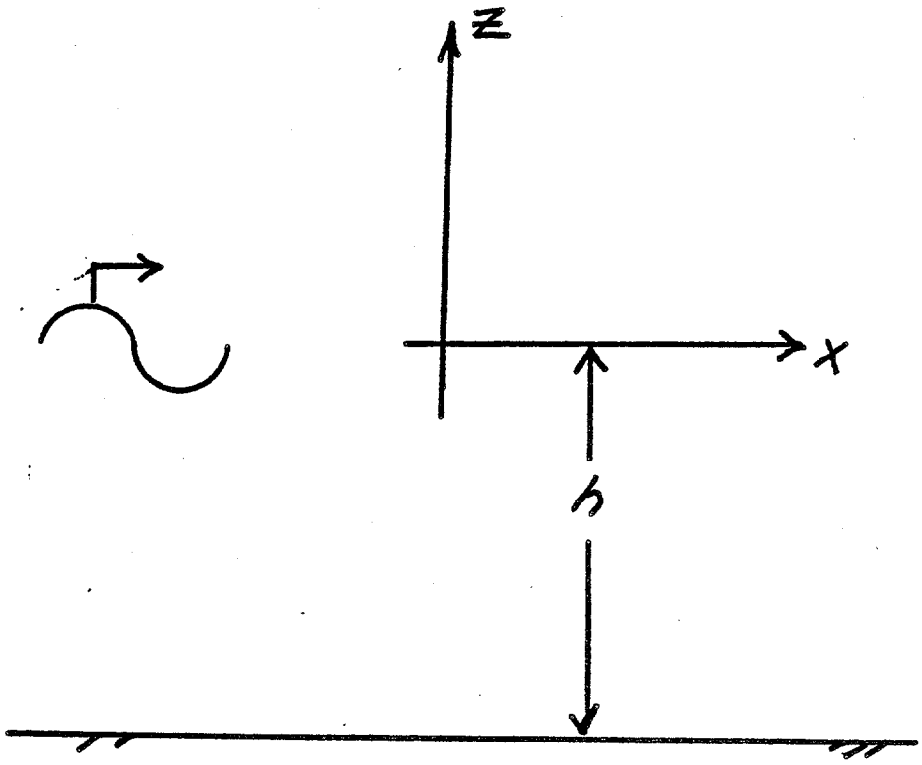

F.5 RANGE OF VALIDITY OF AIRY WAVE THEORY

(Adapted from Le Mehaute, 1969)

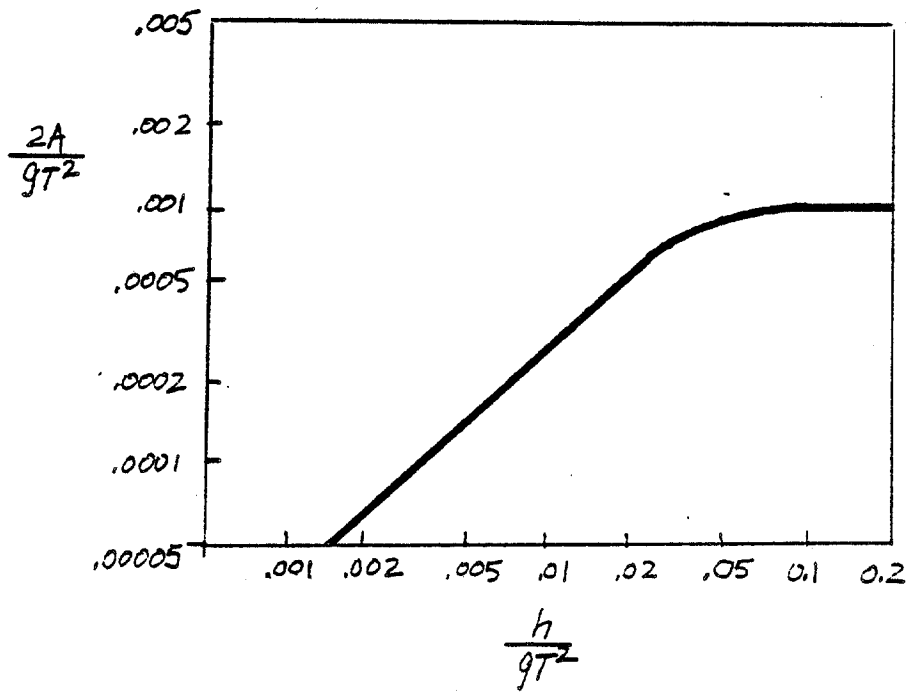

F.6 COORDINATE SYSTEM FOR THE GRID

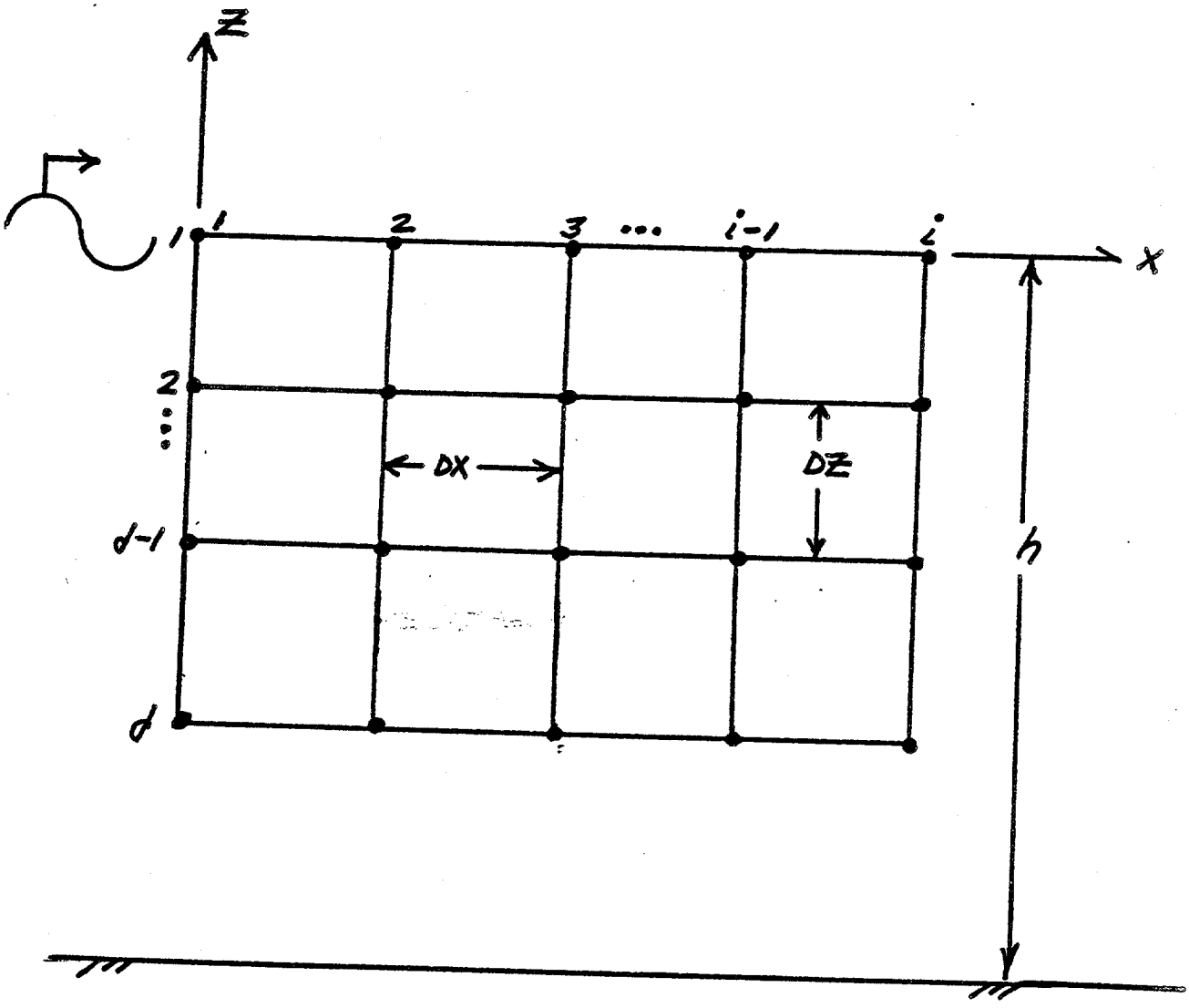

F.7 ALGORITHM FOR GENERATING WAVE KINEMATICS I

This figure describes an algorithm for finding the wave kinematics on the mean waterline.

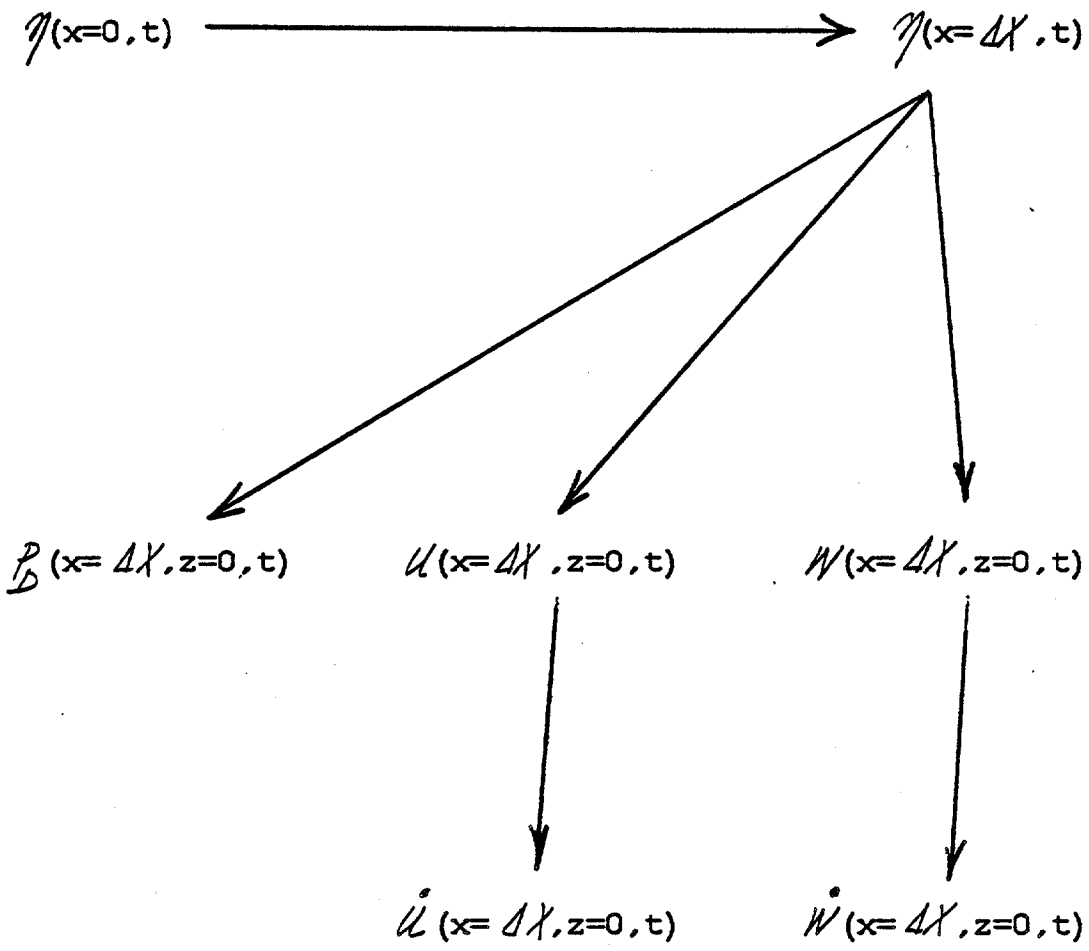

F.8 ALGORITHM FOR GENERATING WAVE KINEMATICS II

This figure describes an algorithm for finding the wave kinematics below the mean waterline.

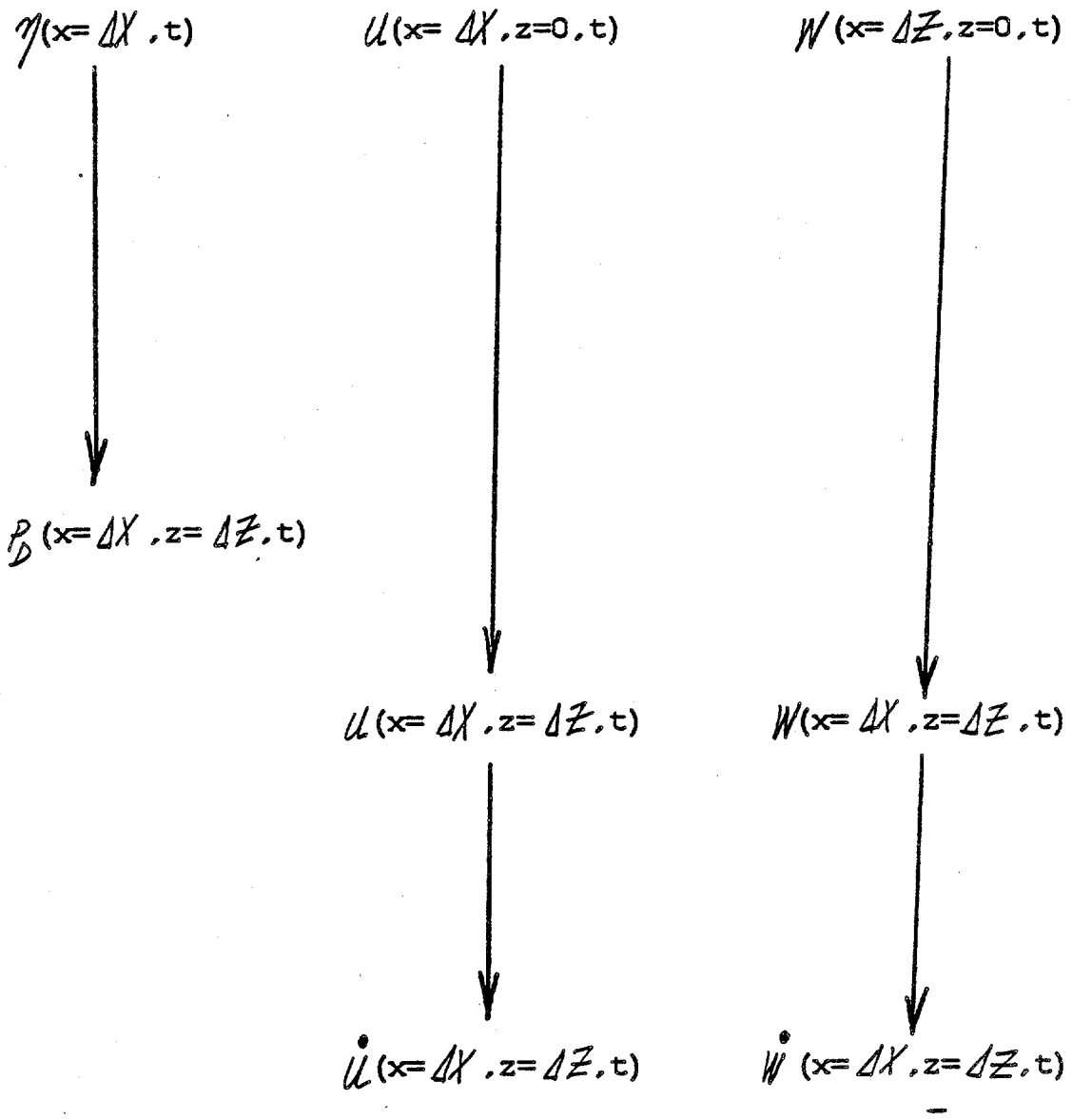

F.9 HORIZONTAL WATER-PARTICLE VELOCITY I

This figure shows an impulse response function for transforming the free-surface elevation into the horizontal water-particle velocity on the mean waterline in deep water. The time step is .25 seconds. Notice how rapidly the function approaches zero as the time becomes greater than or less than zero.

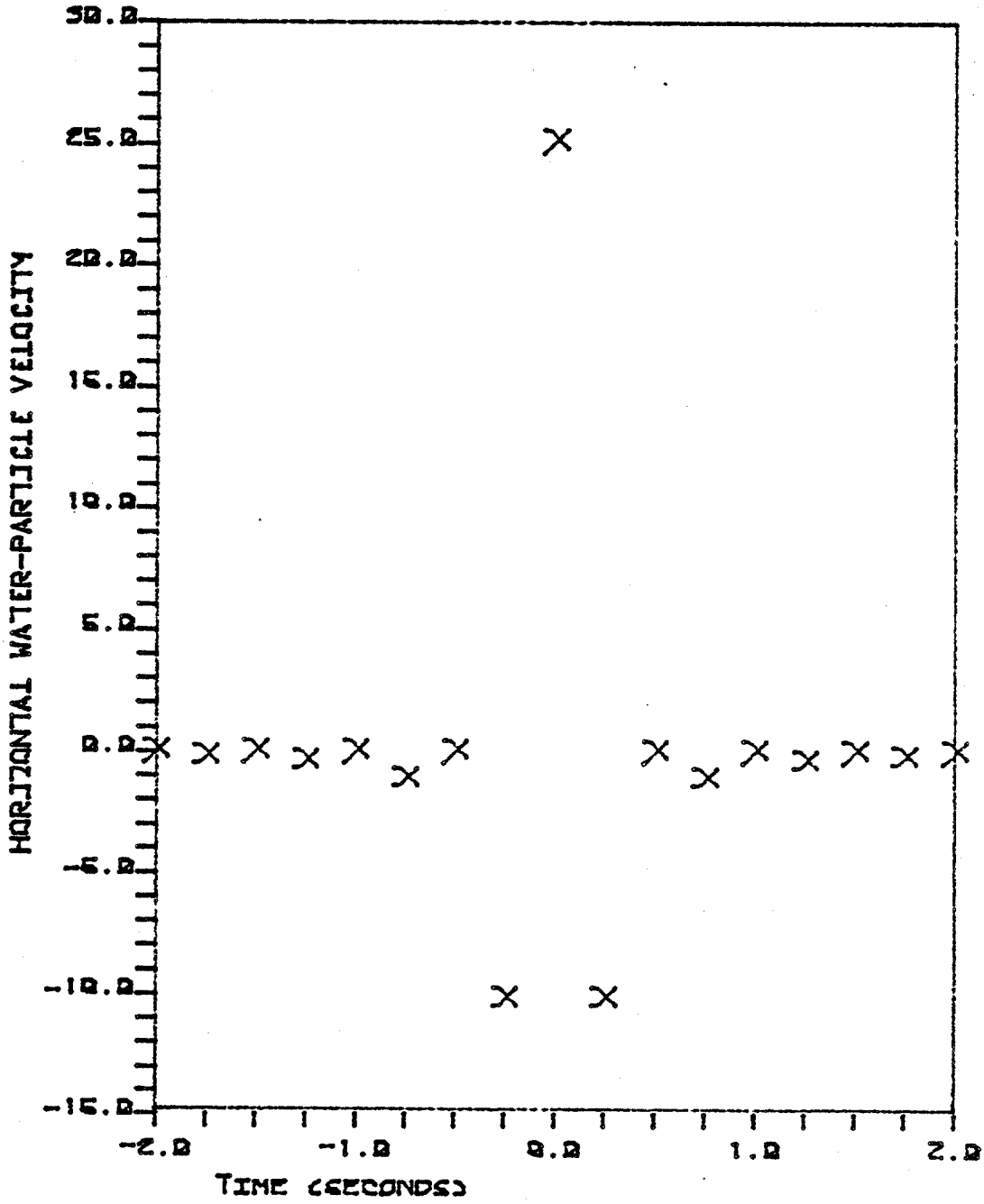

F.10 HORIZONTAL WATER-PARTICLE VELOCITY II

This figure shows an impulse response function for transforming the free-surface elevation into the horizontal water-particle velocity on the mean waterline in finite water depth. The time step is .25 seconds. The water depth is 25. feet. Even for this very shallow water depth the behaviour of the function differs very little from its behaviour in deep water.

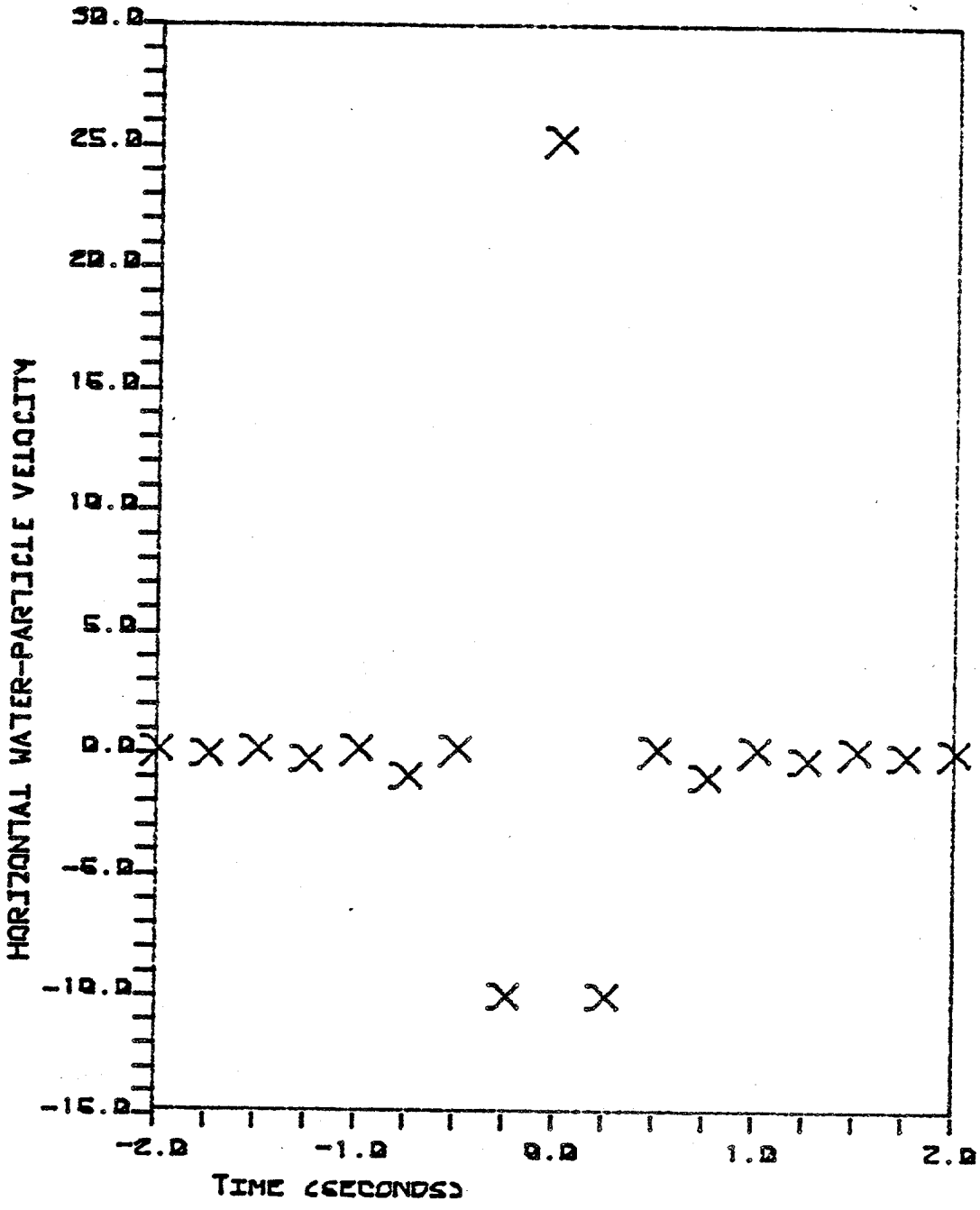

F.11 VERTICAL ATTENUATION IN DEEP WATER

This figure shows the inverse Fourier transform of the transfer function for modeling vertical attenuation in deep water. This function models the vertical attenuation over a change in depth of 25. feet.

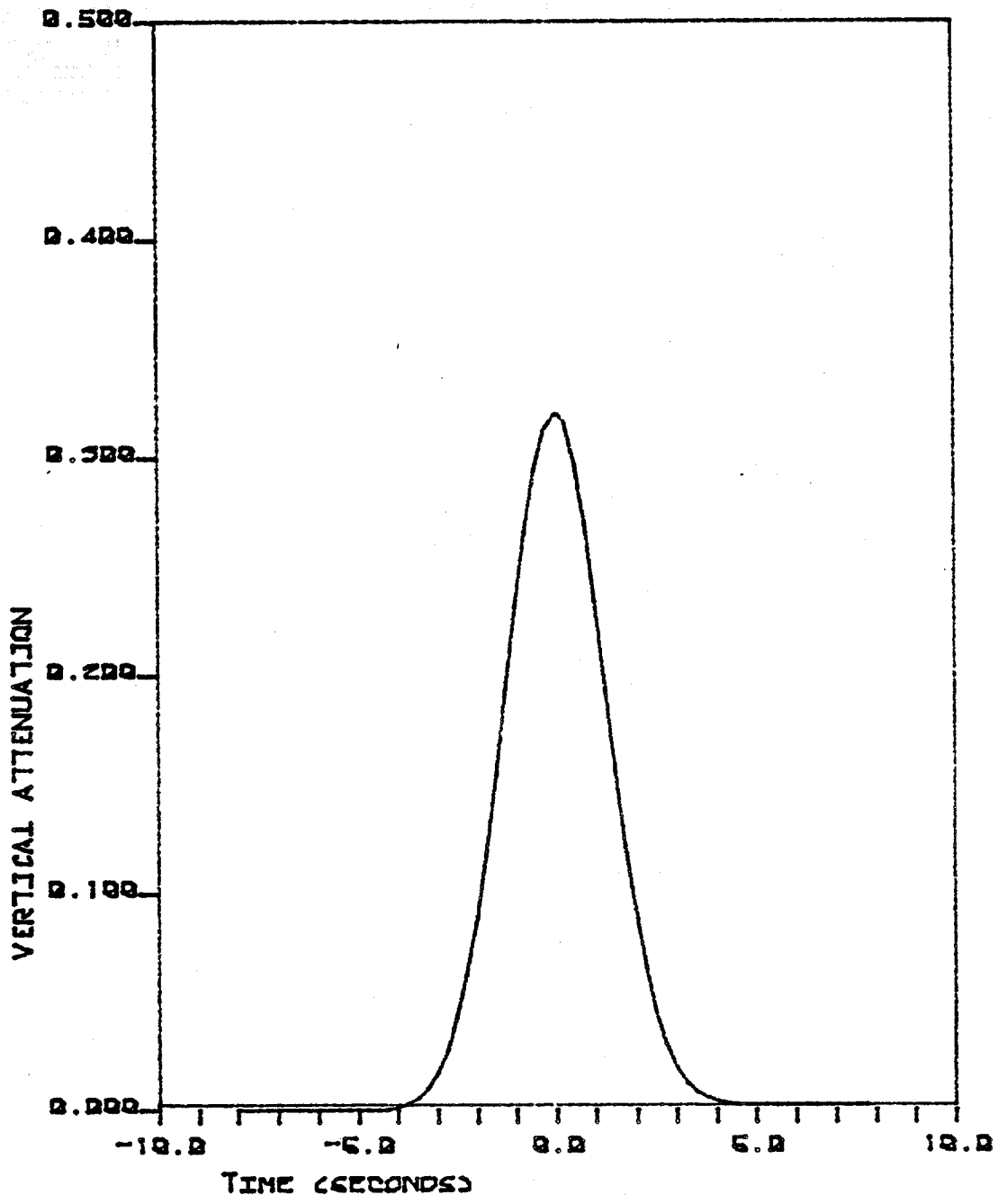

F.12 VERTICAL ATTENUATION IN WATER IN FINITE DEPTH

This figure shows impulse response functions for performing vertical attenuation in water of finite depth in comparison to the same function in deep water. The water depth is 50. feet. The distance over which the time series are attenuated is 25. feet. The time step is .25 seconds. The graph on the left is the impulse response function for the transfer function that contains the hyperbolic cosines. The graph on the right is the impulse response function for the transfer function that contains the hyperbolic sines. The symbols represent the finite depth results calculated by using the fast Fourier transform. The solid lines are deep water theory.

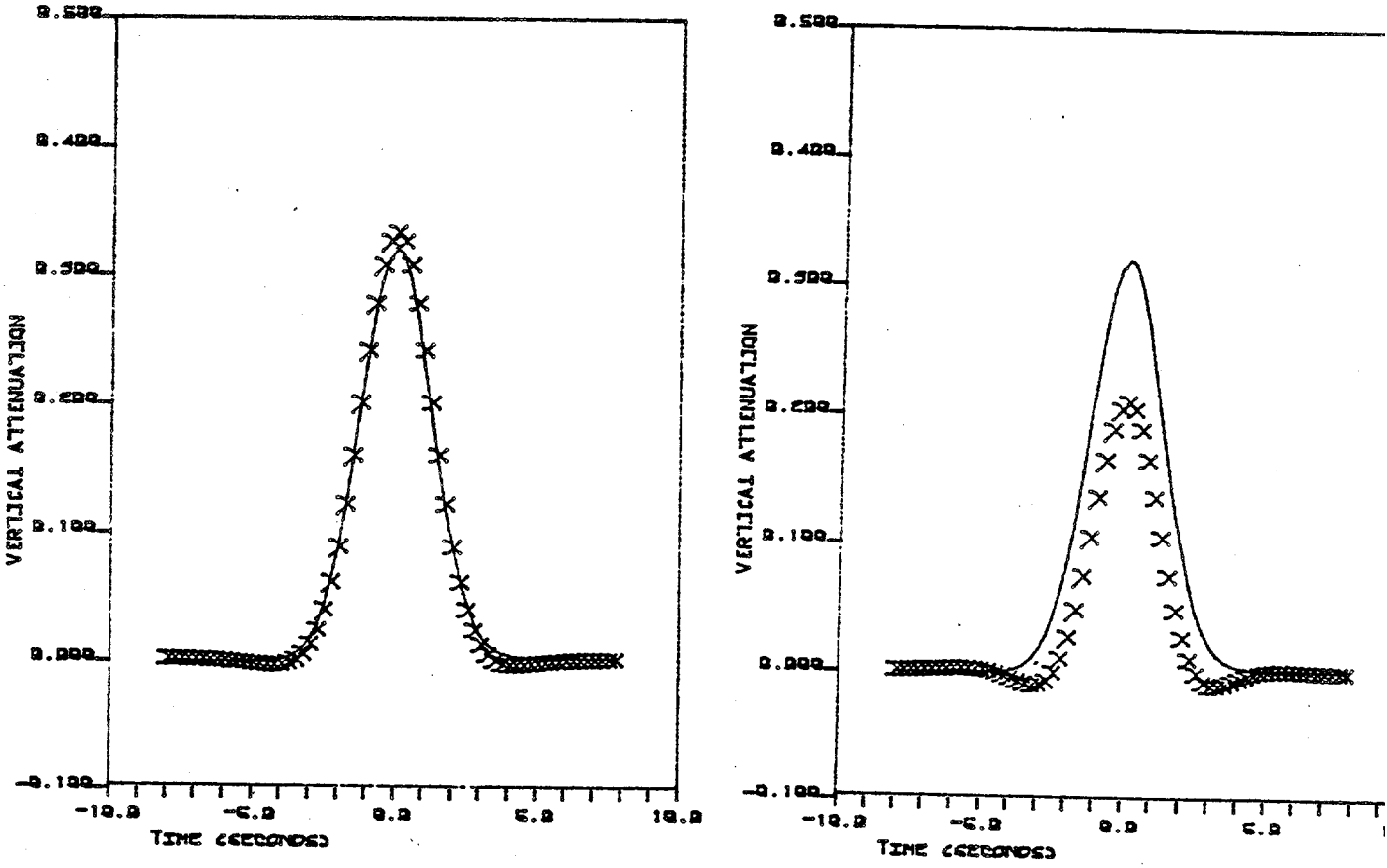

F.13 HORIZONTAL PROPAGATION IN DEEP WATER I

This figure shows the inverse fourier transform of the transfer function for horizontal propagation when there is no cut-off frequency. This function models the horizontal propagation over a distance of 25. feet.

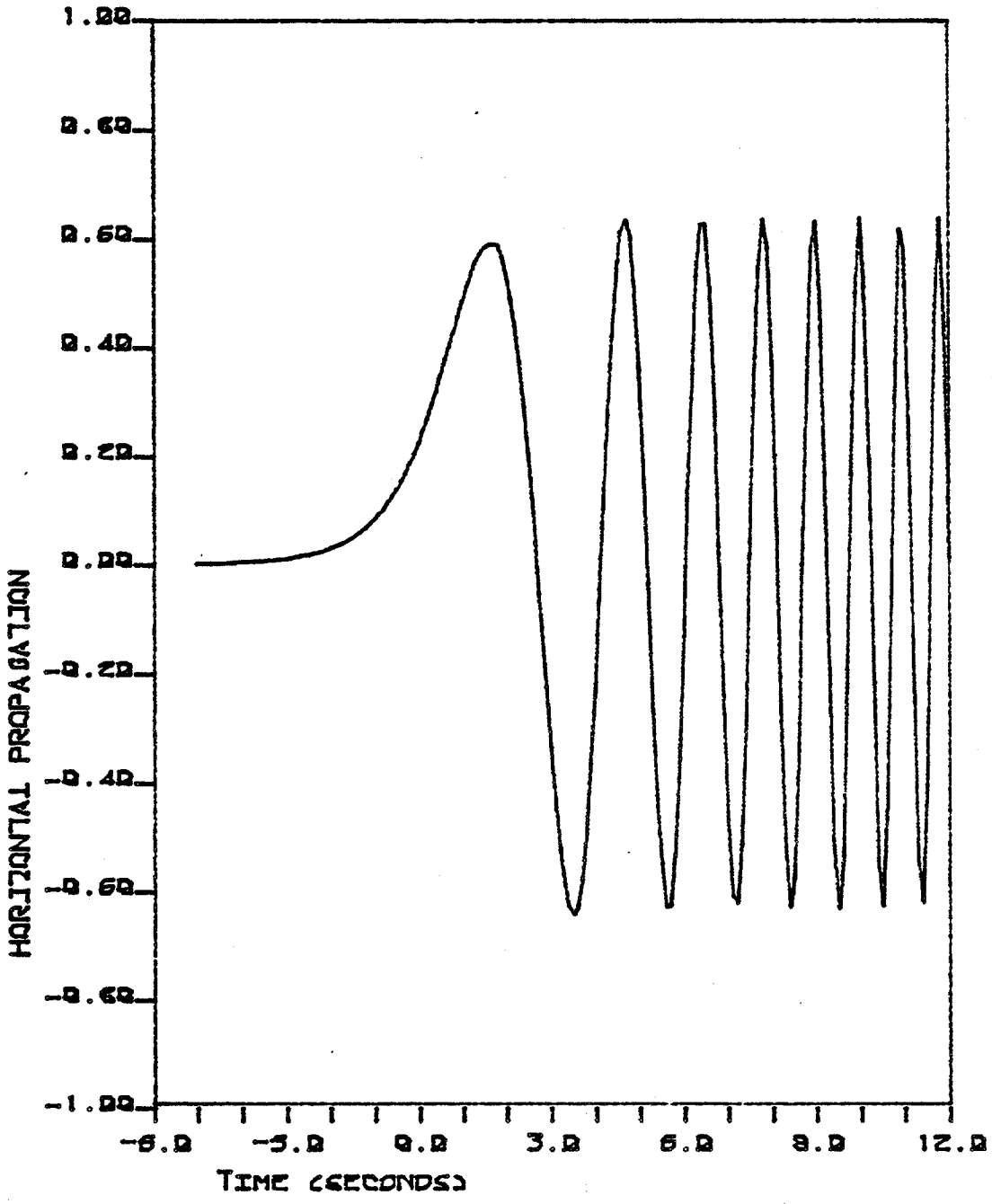

F.14 HORIZONTAL PROPAGATION IN DEEP WATER II

This figure shows the inverse fourier transform of the transfer function for horizontal propagation when there is a finite cut-off frequency. The cut-off frequency equals 1. Hz. The distance of propagation is 25. feet.

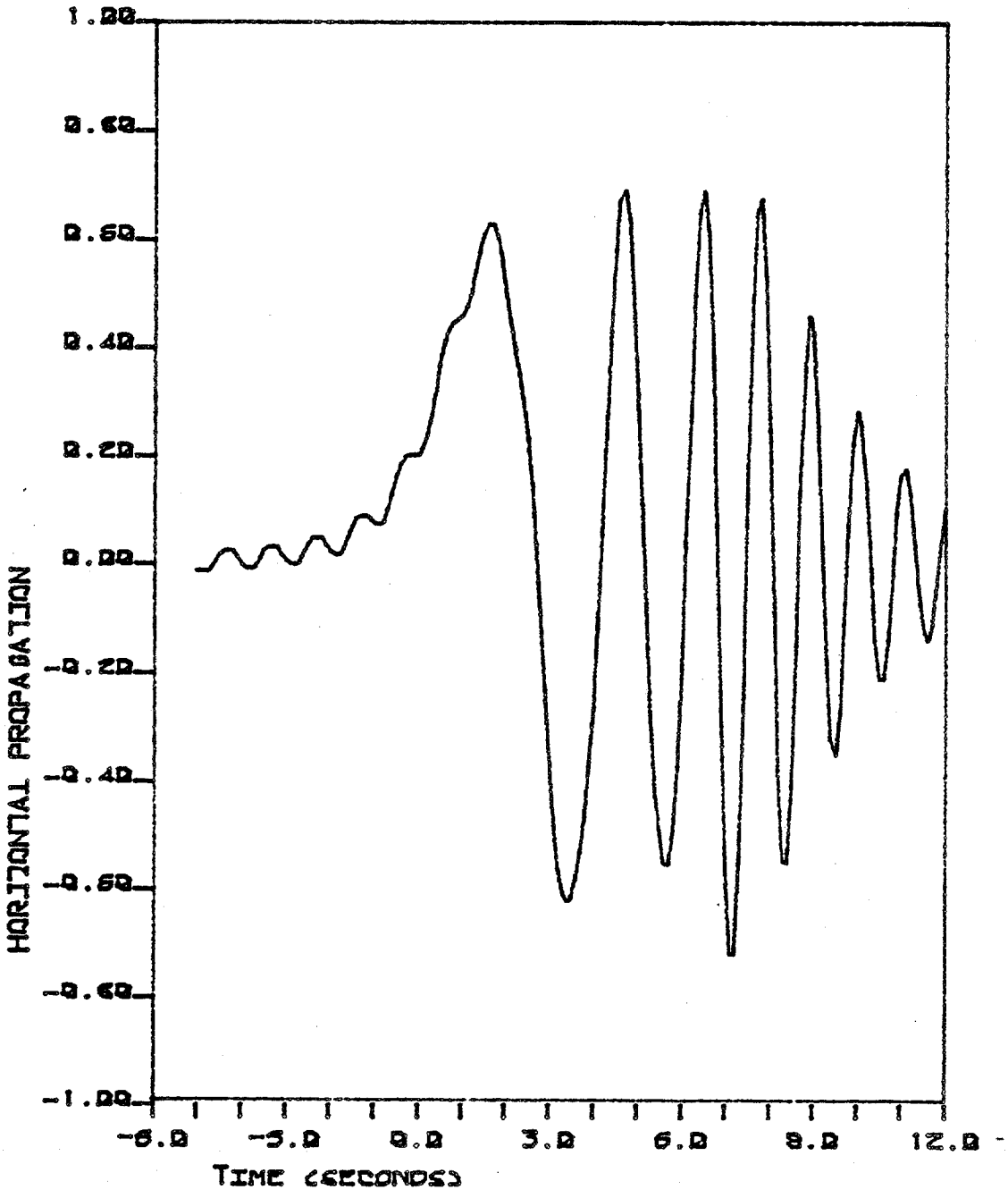

F.15 HORIZONTAL PROPAGATION IN FINITE WATER DEPTHS

This figure shows an impulse response function for performing horizontal propagation in water of finite depth in comparison to the same function in deep water. The water depth is 50. feet. The time step is 0.5 seconds. The distance of propagation is 25. feet. The symbols represent the finite depth results calculated by using the fast Fourier transform. The solid line is theory in deep water.

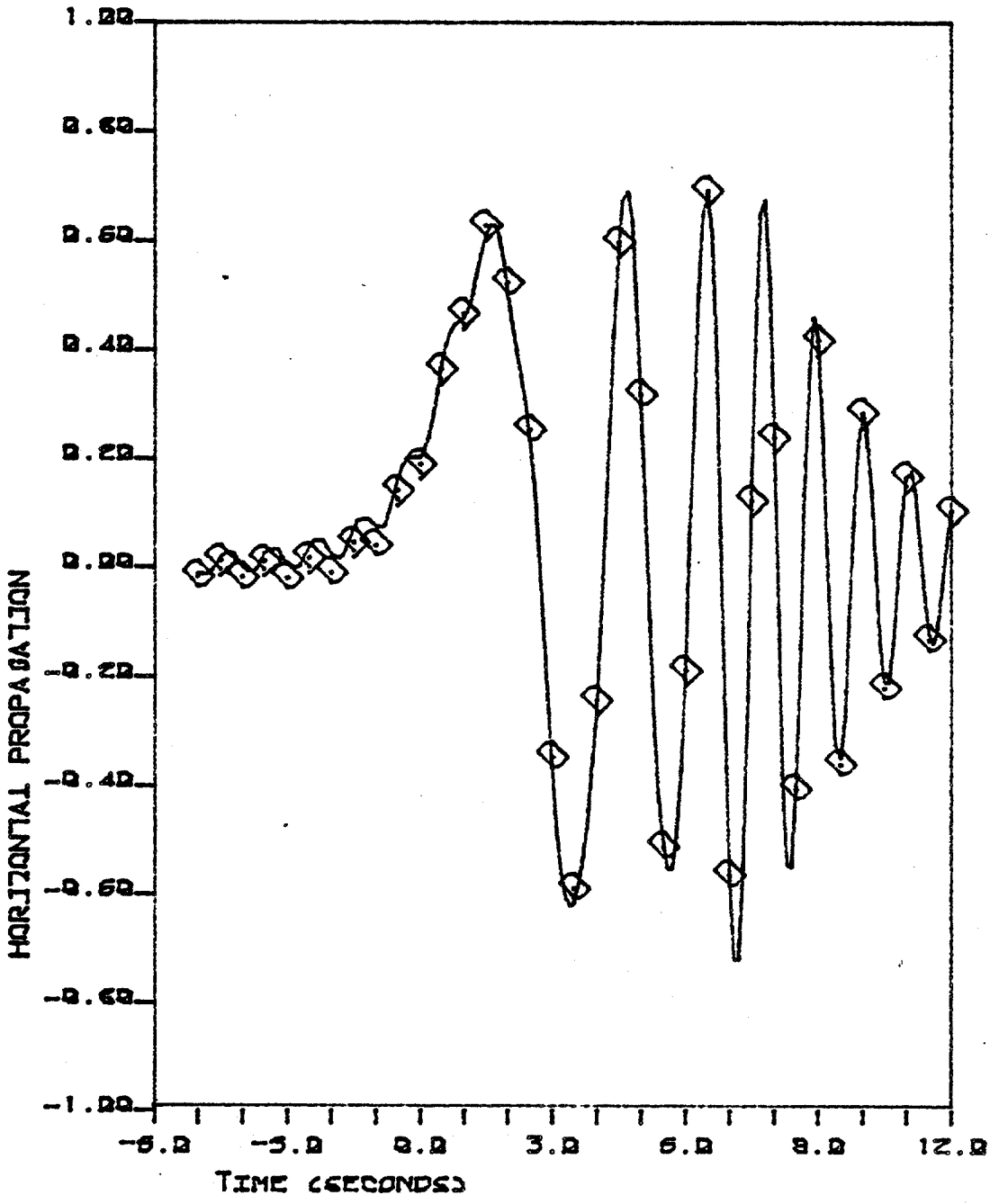

F.16 SUM OF SINUSOIDS VERSUS THE PROPOSED METHOD I

This figure compares the speed of sum of sinusoids to the proposed method for modeling ocean waves. A 3 by 3 grid has been chosen. The grid spacing on the horizontal axis is 150. feet, and the grid spacing on the vertical axis is 30. feet. The wave kinematics at each grid point have been calculated for 100 time steps. The number of discrete waves used by sum of sinusoids is plotted on the X-axis. On the Y-axis, the ratio of the speed of the proposed method to sum of sinusoids is plotted.

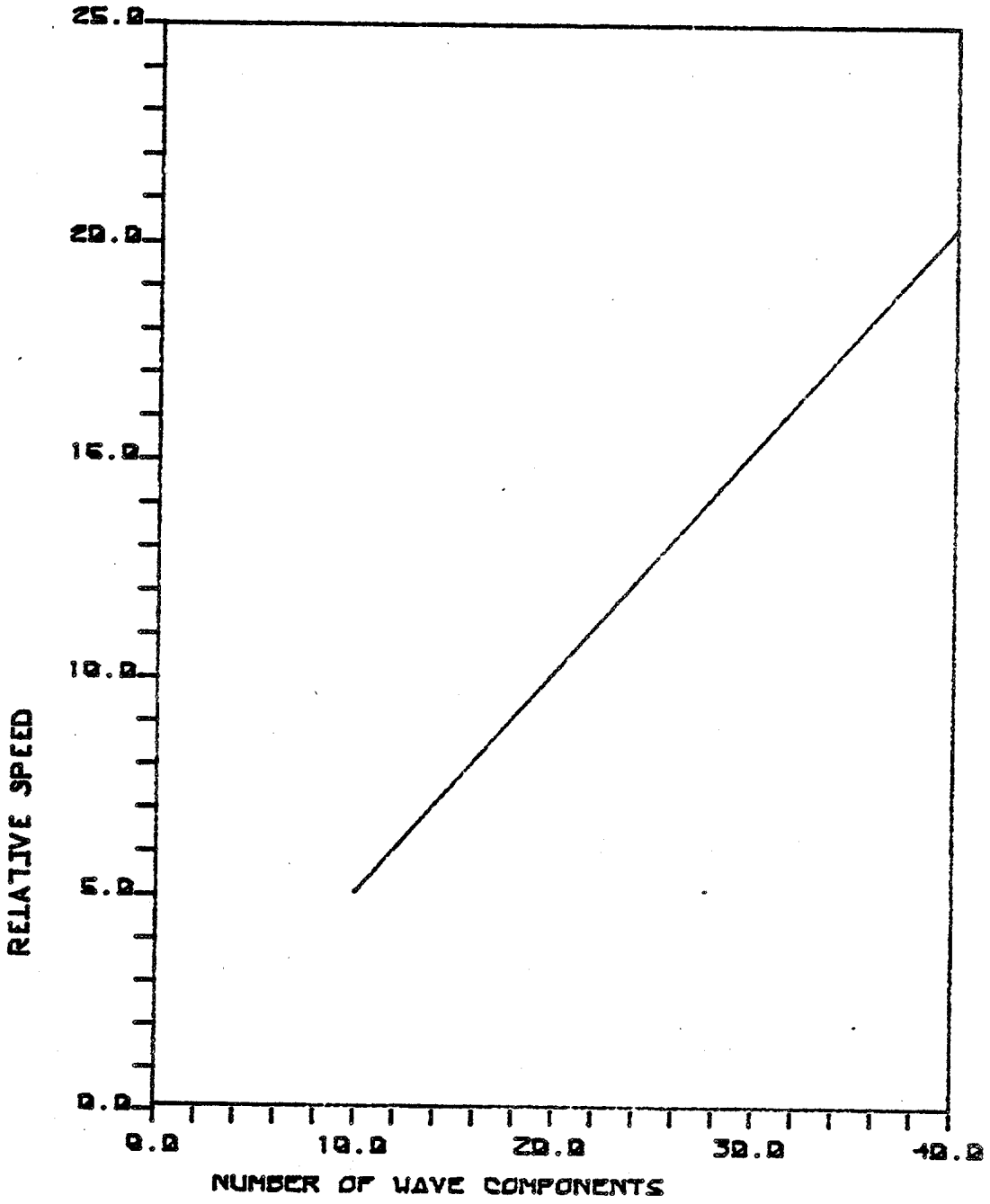

F.17 SUM OF SINUSOIDS VERSUS THE PROPOSED METHOD II

This figure compares the speed of sum of sinusoids to the proposed method for modeling ocean waves. A 5 by 10 grid has been chosen. The grid spacing on the horizontal axis is 25. feet, and the grid spacing on the vertical axis is 25. feet. The wave kinematics at each grid point have been calculated for 50 time steps. The number of discrete waves used by sum of sinusoids is plotted on the X-axis. On the Y-axis, the ratio of the speed of the proposed method to sum of sinusoids is plotted.

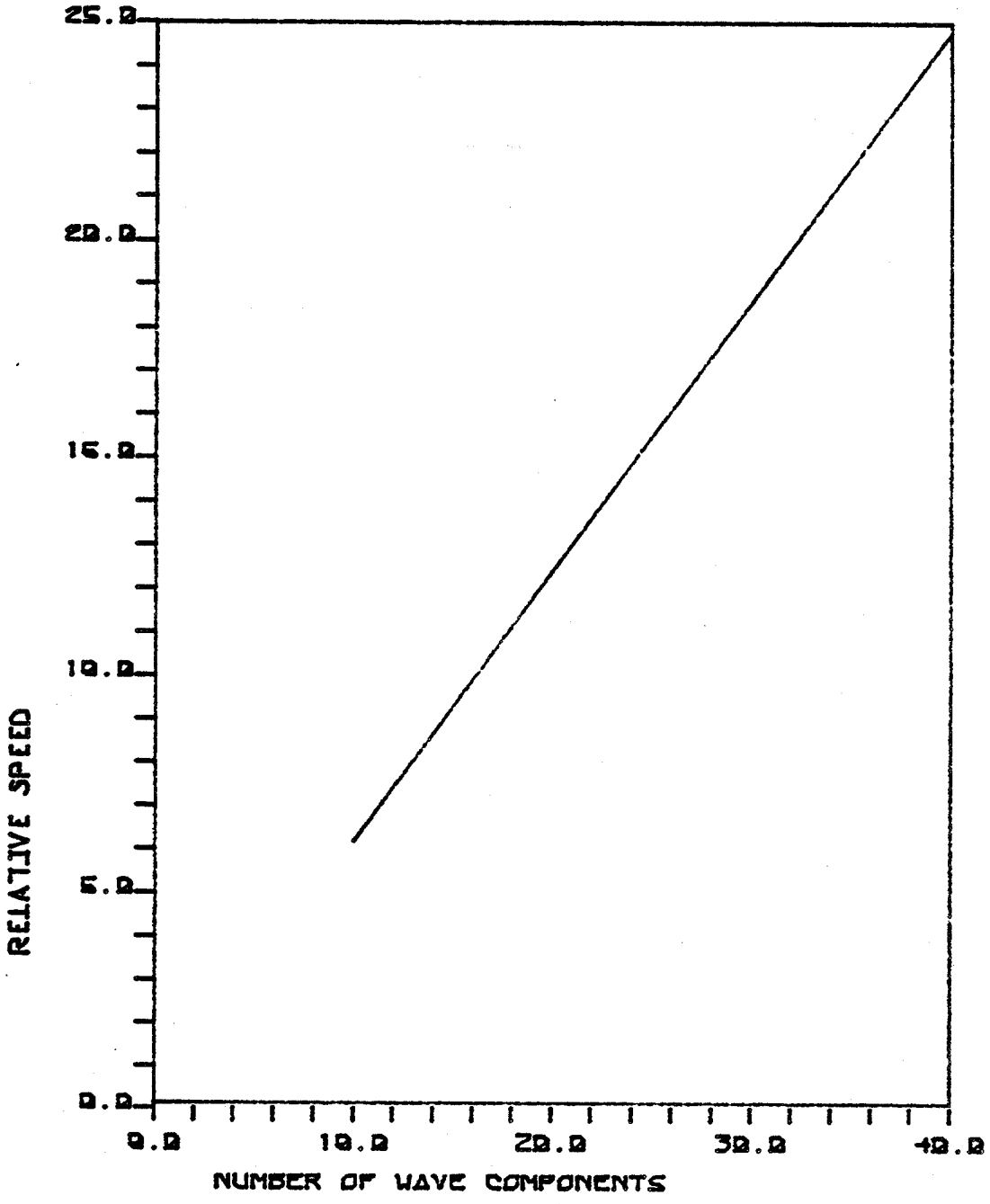

F.18 ERROR ANALYSIS OF CENTRAL DIFFERENCE METHOD

The relative error of the central difference method increases as the number of samples per wave decreases. As the sampling rate approaches infinity, the relative error error approaches one. As the sampling rate approaches two samples per wave, the relative error goes to zero.

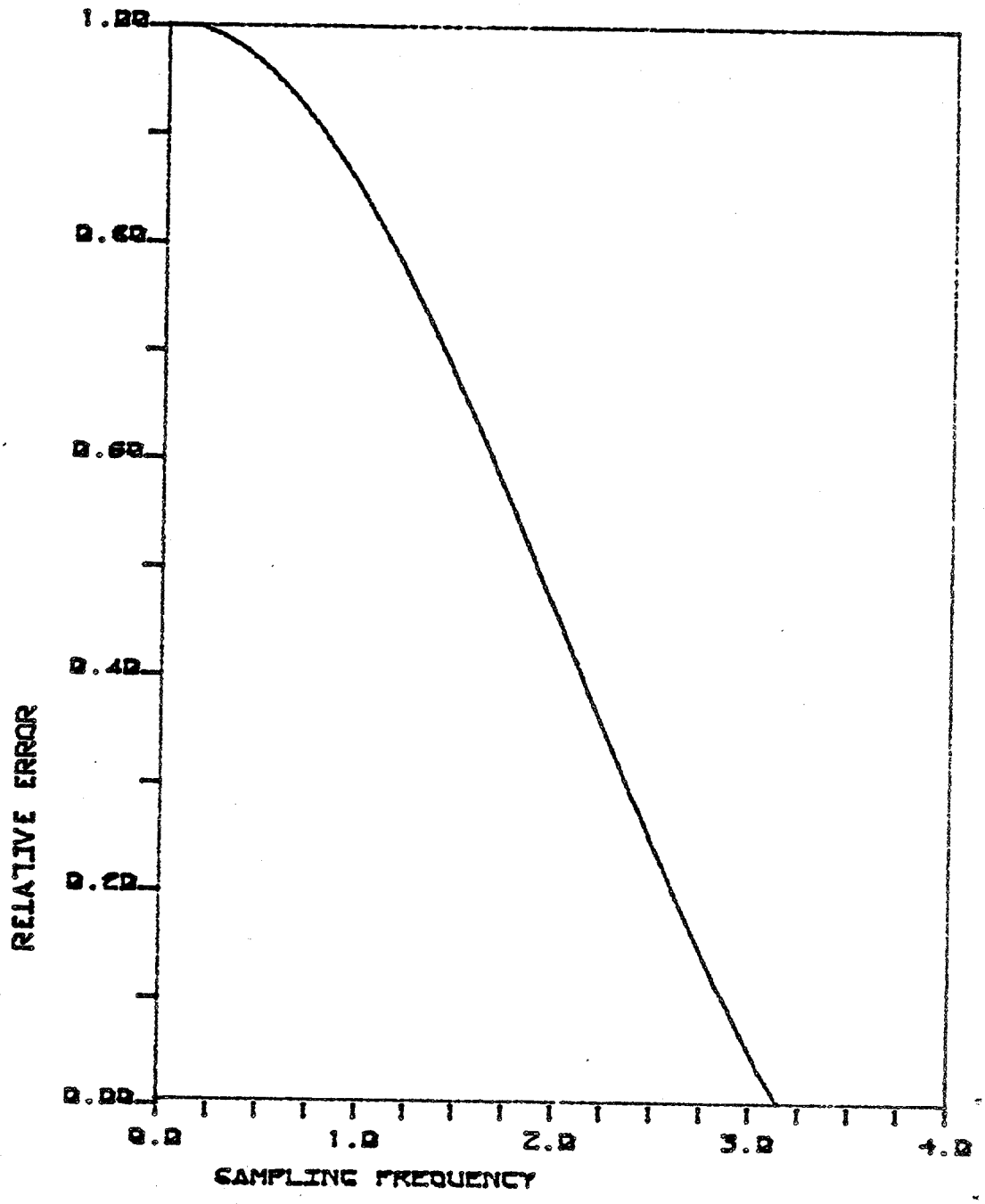

F.19 SINUSOIDAL WAVE CONTAMINATED WITH NOISE

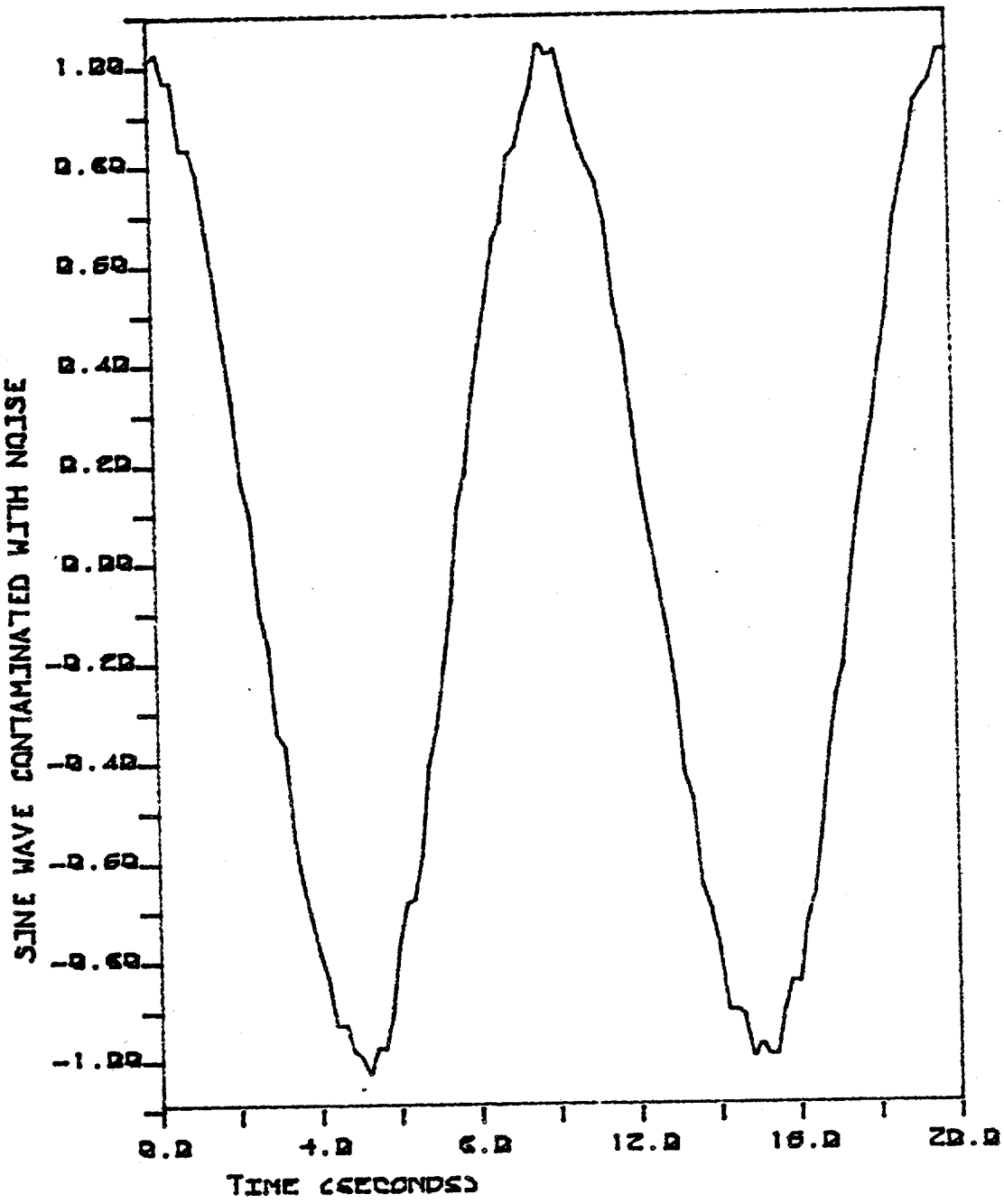

F.20 DERIVATIVE OF A WAVE CONTAMINATED WITH NOISE I

Numerical differentiation amplifies noise. In fact, the amplification increases as the number of sample points per wave increases. In this case, the central difference method has been used to evaluate the derivative of the function plotted in figure J.19. The sampling rate is 25 samples per wave. The solid line is the derivative of the function when it is not contaminated with noise. The symbols represent the derivative of the function as calculated by the central difference method.

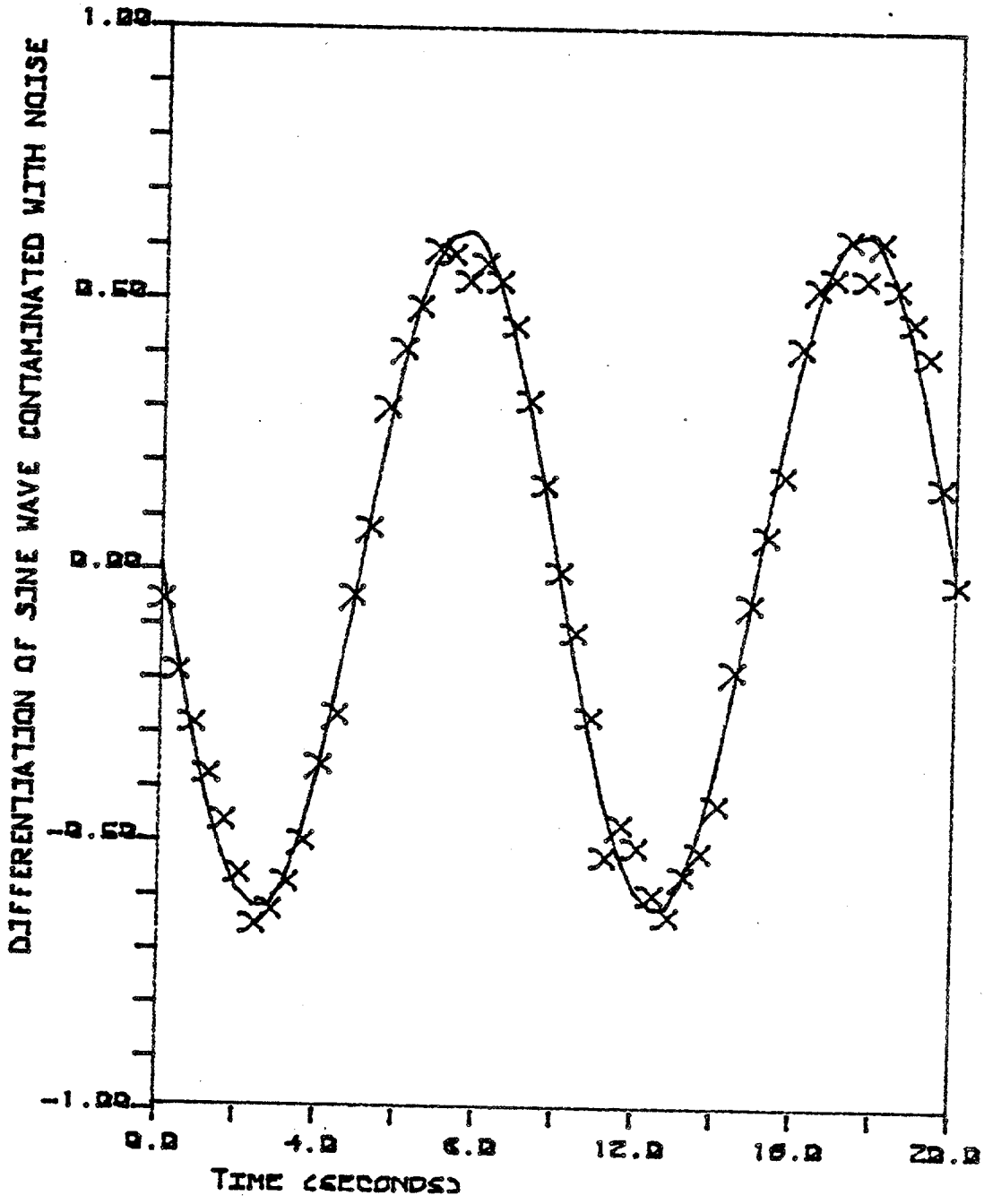

F.21 DERIVATIVE OF A WAVE CONTAMINATED WITH NOISE II

Numerical differentiation amplifies noise. In fact, the amplification increases as the number of sample points per wave increases. In this case, the central difference method has been used to evaluate the derivative of the function plotted in figure J.19. The sampling rate is 50 samples per wave. The solid line is the derivative of the function when it is not contaminated with noise. The symbols represent the derivative of the function as calculated by the central difference method. Clearly, the error at this sampling rate is greater than the error at the lower sampling rate shown on the preceding page.

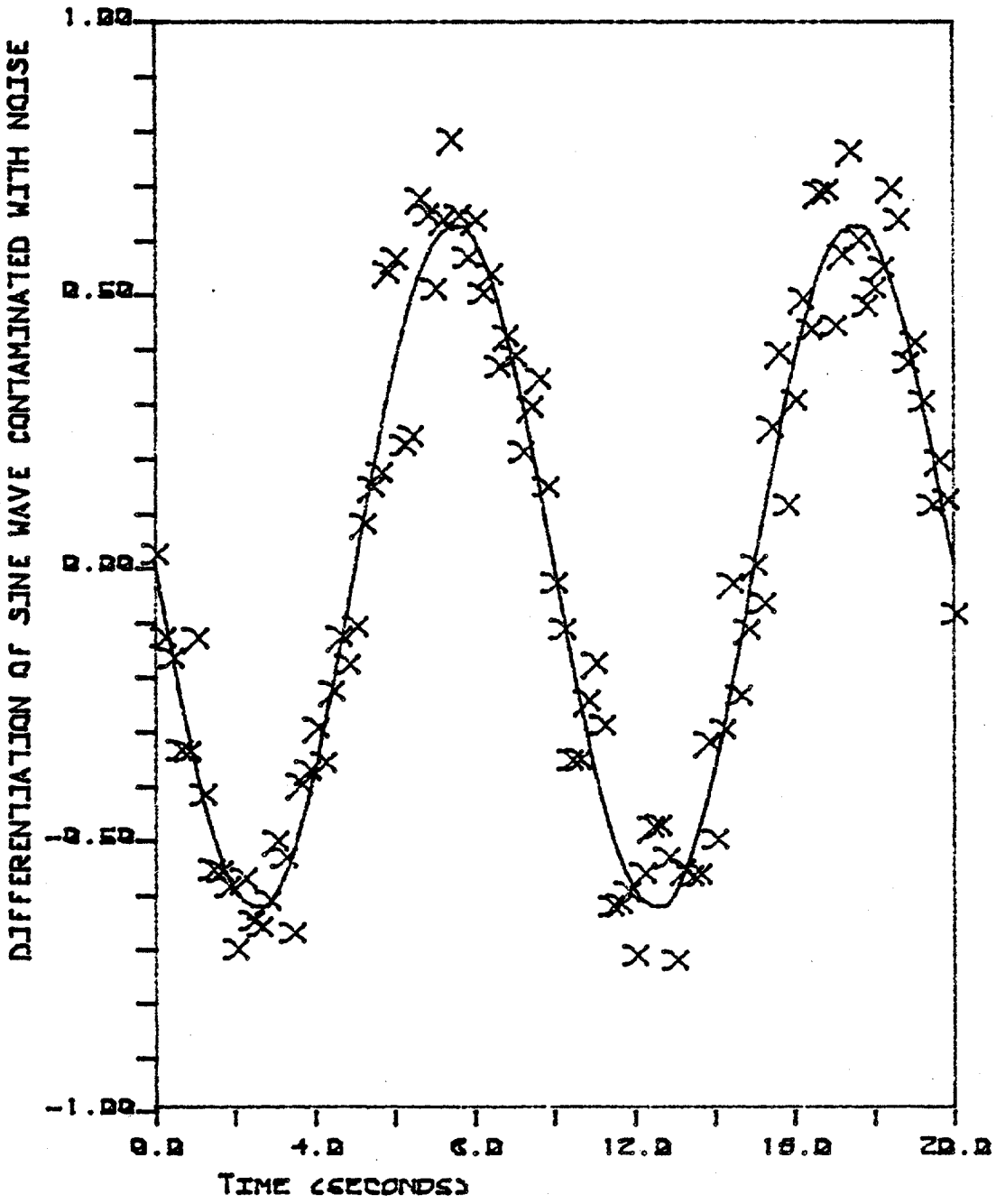

APPENDIX G

TABLES

G.1 AIRY WAVE THEORY IN FINITE WATER DEPTHS

Free surface elevation	$\eta = Re\, e^{i(kx-\omega t)}$
Horizontal particle velocity	$u = Re\, \omega A \frac{\cosh(k(z+h))}{\sinh(kh)} e^{i(kx-\omega t)}$
Vertical particle velocity	$w = Re\, -i\omega A \frac{\sinh(k(z+h))}{\sinh(kh)} e^{i(kx-\omega t)}$
Horizontal particle acceleration	$\dot{u} = Re\, -i\omega^2 A \frac{\cosh(k(z+h))}{\sinh(kh)} e^{i(kx-\omega t)}$
Vertical particle acceleration	$\dot{w} = Re\, -\omega^2 A \frac{\sinh(k(z+h))}{\sinh(kh)} e^{i(kx-\omega t)}$
Dynamic component of water pressure	$P_D = Re\, \rho g A \frac{\cosh(k(z+h))}{\cosh(kh)} e^{i(kx-\omega t)}$
Dispersion relation	$\omega^2 = kg \tanh(kh)$

G.2 AIRY WAVE THEORY IN DEEP WATER

Free surface elevation	$\eta = Re\, A e^{i(kx-\omega t)}$
Horizontal particle velocity	$u = Re\, \omega A e^{kz} e^{i(kx-\omega t)}$
Vertical particle velocity	$w = Re\, -i\omega A e^{kz} e^{i(kx-\omega t)}$
Horizontal particle acceleration	$\dot{u} = Re\, -i\omega^2 A e^{kz} e^{i(kx-\omega t)}$
Vertical particle acceleration	$\dot{w} = Re\, -\omega^2 A e^{kz} e^{i(kx-\omega t)}$
Dynamic component of water pressure	$P_D = Re\, \rho g A e^{kz} e^{i(kx-\omega t)}$
Dispersion relation	$\omega^2 = kg$

A Separable Cross-Entropy Approach to Power Spectral Estimation

by

Cheng-Yuan Liou

B.S., National Central University
(1974)

M.S., National Taiwan University
(1978)

Submitted in Partial Fulfillment
of the Requirements for the Degree of

Doctor of Philosophy

in

Ocean Engineering

at the

Massachusetts Institute of Technology
May 1985

Signature of Author Cheng-Yuan Liou
Department of Ocean Engineering

Certified by J. Kim Vandiver
J. Kim Vandiver
Thesis Supervisor

Accepted by A. Douglas Carmichael
Chairman, Department Committee

A SEPARABLE CROSS-ENTROPY APPROACH TO POWER SPECTRAL ESTIMATION

by

Cheng-Yuan Liou

Submitted to the Department of Ocean Engineering
on May 20, 1985 in partial fulfillment of the
requirement for the Degree of Doctor of Philosophy
in Ocean Engineering

ABSTRACT

A new approach is presented for power spectrum estimation based on a separable Cross-Entropy modeling procedure. We first develop a general model of a multi-channel, multi-dimensional stationary Gaussian random process which is sampled on a non-uniform grid. An approximate separable model is then fitted to this in which selected frequency samples of the process are modelled as independent random variables. Two cross-entropy-like criteria are used to select optimal approximations. One method yields a spectral estimation algorithm which is a generalized version of Capon's MLM method, and the other is similar to classical windowing methods. Examples are given demonstrating the performance of the new approach. One of the methods is particularly powerful at resolving harmonic signals in the presence of noise. The methods can be used for mode shape and multi-dimensional wave number estimation.

Thesis Supervisor: Prof. J. Kim Vandiver
Title: Associate Professor of Ocean Engineering

Thesis Committee: Professor Bruce R. Musicus
Professor Greg L. Duckworth

ACKNOWLEDGEMENT

I thank J. Kim Vandiver for his guidance and supervision during my study at M.I.T. I thank Gregory Lynn Duckworth for valuable dicussions which particularly aided this work. I thank Bruce Ronald Musicus for valuable discussions. The idea of this thesis was first discussed with him. Without his encouragement and help, this thesis would still be several pages in my notebook. I thank Jen-Yi Jong for helping my study and stay during last 3 years. I thank Yang-Hann Kim, Douglas Dummermuth, and Kamyab Samii for making my stay here pleasant and rewarding. I would also like to thank Anna Markowitz for her kind help during the past three years.

TABLE OF CONTENTS

		Page
Abstract		2
Acknowledgement		3
Table of Contents		4
Chapter 1	INTRODUCTION	5
Chapter 2	APPROACH	8
	Section 2.1 General Theory	10
	Section 2.2 Power Spectrum Estimation	18
Chapter 3	APPLICATIONS	38
	Section 3.1 Cross Spectrum Estimation	38
	Section 3.2 Modal Analysis	41
	Section 3.3 Wavenumber Spectrum Estimation	52
Chapter 4	CONCLUSION	58
APPENDIX		61
A Technical Approach for Improving the Resolution Ability		
REFERENCES		66

Due to the limitation of using an inexpensive printer, some of the mathematical symbols in this work are assembled conventional typewriter characters. These symbols are listed below.

/
\ = $\int$: integral ; @ = $\oint$: contour integral
/

$\overline{\Sigma} = \sum$: sum ; $\overline{\Pi} = \prod$: multiply

/ \
| | = [ ] : matrix
| |
\ /

CHAPTER 1

INTRODUCTION

Due to the finite length and finite samples of the correlation function, past research has concentrated on the subject of spectral estimation in order to achieve high performance in both resolution and stability. Due to the availability of the FFT (fast Fourier transform) for calculating unsmoothed spectra and correlation functions, the windowing methods and adaptive methods [5] are popular and well-developed. The variance of the unsmoothed spectrum obtained by the windowing method can be reduced by a smoothing procedure, such as averaging over a neighboring frequency band or over several independent unsmoothed spectra. The design of a window focuses on undertaking the effects of sidelobes [4]. The windowing method can not take advantage of the intrinsic structure of a particular stationary random process. The adaptive method can incorporate a model for the data and through that model the spectrum can be estimated. The adaptive methods are the maximum entropy method (MEM) [2] and MLM as said in [9]. Both MEM and MLM are capable of high resolution performance. (See reference [7] for a list of these diverse methods.) The spectrum estimated by MLM has an additional potential usage. Since the spectrum estimated by MLM is unbiased, an estimated spectrum which has less variance can be obtained simply by averaging over several independent estimates.

This averaging procedure leads to an accumulated knowledge about the true spectrum. These diverse methods have given much insight into the character of spectral analysis. The interpretation in reference [13] is a nice example in this sense and MEM has also been included in [17] as a special case. In order to make progess in both understanding these diverse methods and exploring new methods we present this new approach to the subject of spectral estimation.

Motivated by the success of sample cases, we start with a rough intuitive model for the data and increase its precision through an inference principle. For reasons of simplicity the stationary Gaussian random processes (GRP) assumption is made throughout this work. By using a finite approximation of the cross entropy function, the estimated spectrum is obtained. The MCE principle [16] states that an a posteriori probability density function (PDF) Q can be inferred from an a priori PDF P by minimizing the cross entropy function H(Q,P) between Q and P. The roles of P and Q are reversed in Kullback's discriminant function (KDF) [8], which is equal to H(P,Q). The prior PDF P for the samples of a stationary GRP can be formulated using the available correlation function. In our approach, the PDF Q for the Fourier coefficients of the samples can be formulated [15] according to the GRP assumption. The variances of those Fourier coefficients form the spectrum of the samples. Since the available correlation function is

known only at a finite number of time lags, finite forms of P and Q are used in the cross entropy function H(Q,P). The spectrum derived by this method will correspond to that given by the windowing method and MLM in special cases.

Chapter 2 provides a general theory with four examples to demonstrate its usage. Chapter 3 discusses some applications in cross spectral estimation, modal analysis, and wavenumber estimation. Chapter 4 provides a brief summary of the results. The appendix gives an alternate technical approach for estimating the power spectrum which is different from that given in the main text.

CHAPTER 2

APPROACH

In this chapter we will first derive some basic formulas and then apply them to the subject of spectral analyses. The problem statement is as follows.

Let $\{ \underline{x}_1 ,\ldots,\underline{x}_i ,\ldots,\underline{x}_L \}$ be a set of joint Gaussian random vectors. Where $\underline{x}_i$ is an Ni dimension column vector and

$$E\{\underline{x}_i\}=\underline{mx}_i \quad , \quad Cov\{\underline{x}_i ,\underline{x}_j\}=E\{(\underline{x}_i -\underline{mx}_i)(\underline{x}_j -\underline{mx}_j)'\}=Rij .$$

E{.} denotes expectation value. A′ denotes the Hermitian of the matrix A. Where Rij is a Ni by Nj matrix.

Let $\underline{x}'= [\underline{x}_1' ,\underline{x}_2' ,\ldots,\underline{x}_L']$

$$Rx= \begin{pmatrix} R11 & \cdots & R1L \\ \vdots & & \vdots \\ RL1 & \cdots & RLL \end{pmatrix} \quad \text{and} \quad \underline{mx}' = [\underline{mx}_1' ,\underline{mx}_2' ,\ldots,\underline{mx}_L'].$$

$\underline{x}$ and $\underline{mx}$ are column vectors with dimension $N= \sum_{i=1}^{L} Ni$.

This Rx is a N by N matrix. Assume Rx is full rank and known. Then $P(\underline{x})= N(\underline{mx},Rx)$, where $N(\underline{m},R)$ denotes normal PDF with mean $\underline{m}$ and covariance R.

Let $\{ \underline{y}_1 ,\ldots,\underline{y}_i ,\ldots,\underline{y}_p \}$ be a set of random vectors.

Where each $\underline{y}_i$ is a Mi dimensional column vector which

depends linearly on the $\{ \underline{x}_i \}$, $\underline{y}_i = \sum_{k=1}^{L} Tik\ \underline{x}_k$; i=1,...p.

Tik is a Mi by Nk matrix.

Let $\underline{y}' = [\ \underline{y}_1' , \underline{y}_2' , \ldots , \underline{y}_p'\ ]$. Then $\underline{y}=T\underline{x}$, where

$\underline{y}$ is a column vector with dimension $M= \sum_{i=1}^{p} Mi$ and

$$T= \begin{pmatrix} T11 & \ldots & T1L \\ \vdots & & \vdots \\ Tp1 & \ldots & TpL \end{pmatrix} \text{ ; T is a M by N matrix.}$$

Assume T has rank $M \leq N$. Then $P(\underline{y})=N(T\underline{m}x, TRxT')$

$=N(\underline{m}y, Ry)$; where $\underline{m}y=T\underline{m}x$ and $Ry=TRxT'$.

We wish to model $\{\underline{y}_i\}$ as independent random vectors, so that the posterior PDF Q will be separable which will facilitate the computation. Example #1 in the following context will give us a little bit of sense about how good this model is. Essentially, the less correlation among the $\{\underline{y}_i\}$, the better the model is.

Now we can write Q as follows.

$$Q(\underline{y})=q_1(\underline{y}_1)q_2(\underline{y}_2)\ldots q_p(\underline{y}_p)$$

In the following two sections we will find the solution for this model and explain the results.

Section 2.1: General Theory

With the above problem statement the next step is to find a proper discriminant function which can describe the difference between Q and P quantitatively. Through minimizing that selected discriminant function we can fit our model Q to the a priori P. There are several candidates for this discriminant function. The one we prefer is the cross entropy function H(Q,P), essentially because it can handle the normal distribution and is well-founded [16]. Its counterpart KDF=H(P,Q) is also a good function for handling normal distribution and will be discussed in this context also. Now we derive Q using MCE principle:

$$\{q_i ; i=1,p\} \Longleftarrow \min_{Q} H(Q,P) = \min \int_{/} Q \log\frac{Q}{P}\, d\underline{y}$$

We now solve for Q by variational calculus:

$$H(Q,P) = \int_{/} Q \log Q \, d\underline{y} - \int_{/} Q \log P \, d\underline{y}$$

$$= \int_{/} \prod_{i=1}^{p} q_i(\underline{y}_i) \log \prod_{i=1}^{p} q_i(\underline{y}_i)\, d\underline{y} - \int_{/} \prod_{i=1}^{p} q_i(\underline{y}_i) \log P \, d\underline{y}$$

The constraint for each q_i is: $1 = \int_{/} q_i(\underline{y}_i)\, d\underline{y}_i$

Let c_k be the Lagrange multiplier for q_k. Then:

$$\delta H(Q,P) = \sum_{k=1}^{p} \{ \int_{/} \prod_{\substack{j=1 \\ j\neq k}}^{p} q_j(\underline{y}_j) \log \prod_{i=1}^{p} q_i(\underline{y}_i)\, \delta q_k(\underline{y}_k)\, d\underline{y} +$$

$$+ \int \left[\prod_{\substack{j=1 \\ j\neq k}}^{p} q_j(\underline{y}_j)\, \delta q_k(\underline{y}_k)\, d\underline{y} - \int \left[\prod_{\substack{j=1 \\ j\neq k}}^{p} q_j(\underline{y}_j) \log P\, \delta q_k(\underline{y}_k)\, d\underline{y} \right.$$

$$\left. + \int c\, \delta q_k(\underline{y}_k)\, d\underline{y}_k \right\}$$

$$\delta H(Q,P) = \sum_{k=1}^{p} \left\{ \int \left[\sum_{\substack{j=1 \\ j\neq k}}^{p} \int q_j(\underline{y}_j) \log q_j(\underline{y}_j)\, d\underline{y}_j + 1 + c_k \right.\right.$$

$$\left.\left. + \log q_k(\underline{y}_k) - \int \log P \prod_{\substack{j=1 \\ j\neq k}}^{p} q_j(\underline{y}_j)\, d\underline{y}_j \right] \delta q_k(\underline{y}_k)\, d\underline{y}_k \right\}$$

Since each $\delta q_k(\underline{y}_k)$ is an arbitrary function, set its coefficient to zero in order to get a stationary function $q_k(\underline{y}_k)$ and we obtain:

$$\log q_k(\underline{y}_k) = \int \log P(\underline{y}) \prod_{\substack{j=1 \\ j\neq k}}^{p} q_j(\underline{y}_j)\, d\underline{y}_j + \text{constant.}$$

Substitute data from $P(\underline{y})$ and $Q(\underline{y})$ in the above equation.

$$\log q_k(\underline{y}_k) = -0.5(\underline{y}_k - \hat{\underline{m}}_{y_k})' \left[Ry^{-1} \right]_{kk} (\underline{y}_k - \hat{\underline{m}}_{y_k})$$

$$-0.5 \sum_{\substack{j=1 \\ j\neq k}}^{p} \left\{ (\underline{y}_k - \hat{\underline{m}}_{y_k})' \left[Ry^{-1} \right]_{kj} (E[\underline{y}_j] - \hat{\underline{m}}_{y_j}) \right.$$

$$\left. + (E[\underline{y}_j] - \hat{\underline{m}}_{y_j})' \left[Ry^{-1} \right]_{jk} (\underline{y}_k - \hat{\underline{m}}_{y_k}) \right\} + \text{constant}$$

The $q_k(\underline{y}_k)$'s solution of the above equation is Gaussian:

$$q_i(\underline{y}_i)=N(\underline{\hat{m}}y_i,\{[Ry^{-1}]ii\}^{-1}) \text{ ; where} \qquad \text{(EQ 1)}$$

$[Ry^{-1}]kj$ is the $(k,j)^{\underline{th}}$ submatrix of Ry^{-1} when Ry^{-1} is partitioned by {M1,M2,M3,..,Mp} in both row and column.

All that remains is to solve for the $\underline{\hat{m}}y_i$. Substituting this $\underline{\hat{m}}y_i = E\{\underline{y}_i | q_i\}$ in the above equation, multiplying both sides by $[Ry^{-1}]ii$, and rearranging, gives:

$$\sum_{j=1}^{p}[Ry^{-1}]ij\,(\underline{\hat{m}}y_j-\underline{m}y_j)=\underline{0} \text{ for } i=1,..,p$$

Combining terms into matrix and vector in the obvious way:

$$Ry^{-1}(\underline{\hat{m}}y-\underline{m}y)=\underline{0}$$

Since Ry is assumed to be full rank:

$$\underline{\hat{m}}y=\underline{m}y$$

When $\underline{y}$ is a complex vector, the (EQ 2) and (EQ 4) need to be multiplied by 2.

The value of the minimum cross entropy is:

$$H(Q,P)=0.5\log\frac{|Ry|}{\prod_{i=1}^{p}|\{[Ry^{-1}]ii\}^{-1}|}=0.5\log\frac{\prod_{i=1}^{p}|[Ry^{-1}]ii|}{|Ry^{-1}|}, \qquad \text{(EQ 2)}$$

which is also a measure of goodness of fit.

The $q_i(\underline{y}_i)$ is equal to the conditional density of $\underline{y}$,

which is $P(\underline{y}_i \mid \underline{my}_1, \ldots \underline{my}_{i-1}, \underline{my}_{i+1}, \ldots, \underline{my}_p)$

where $E\{\underline{y}_j \mid q_j(\underline{y}_j)\} = \underline{my}_j$

This result is a consequence of the fact that $P(\underline{y})$ is a natural exponential family of the PDF.

Another approach using KDF=H(P,Q) is:

$$Q \leftarrow\!= \min_Q \int P \log \frac{P}{Q} \, d\underline{y}$$

$$KDF = \int P \log P \, d\underline{y} - \int P \log Q \, d\underline{y}$$

$$\delta KDF = \sum_{k=1}^{p} \int \left[\frac{-P}{q_k(\underline{y}_k)} + c_k \right] \delta q_k(\underline{y}_k) \, d\underline{y}$$

Setting the coefficient of $\delta q_k(\underline{y}_k)$ equal to zero in order to get a stationary q_k and we obtain:

$$q_i(\underline{y}_i) = \int P(\underline{y}) \, d\underline{y}_1 \, d\underline{y}_2 \ldots d\underline{y}_{i-1} \, d\underline{y}_{i+1} \ldots d\underline{y}_p$$

$$= P(\underline{y}_i) = \text{marginal density of } \underline{y}_i$$

$$= N(\underline{my}_i, [Ry]ii) \, . \qquad \text{(EQ 3)}$$

$$\text{Value of minimum KDF} = -0.5 \log \frac{|Ry|}{\prod_{i=1}^{p} |[Ry]ii|} \qquad \text{(EQ 4)}$$

When Ry is a diagonal matrix with submatrices {[Ry]ii} along

its diagonal, the minimum values of both H(Q,P) and KDF are zero. Note that the (EQ 1) is a conditional PDF and (EQ 3) is a marginal PDF. A sharper PDF can always be obtained from the conditional PDF. This is because the marginal PDF is obtained by a smoothing integration which smooths some distinguishable characters of the PDF. So, we expect that (EQ 1) will give more distinguishable information about its variables than (EQ 3) will. The above four equations, (EQ 1 to 4), complete the basic theory. The following three examples will lead to formulas for spectral analysis.

Example #1:

In this example we will test our model for the case where $\underline{x}$ is 2 real, jointly Gaussian random variables.

$\underline{x}' = [\ \underline{x}1\ ,\ \underline{x}2\ ]$

$$E\{\underline{x}\} = \underline{m}x = \begin{pmatrix} \underline{m}1 \\ \underline{m}2 \end{pmatrix} \quad ; \quad Var(\underline{x}) = E\{\underline{x}\underline{x}'\} = \begin{pmatrix} R11 & R12 \\ R21 & R22 \end{pmatrix}$$

$P(\underline{x}) = N(\ \underline{m}x,\ Var(\underline{x})\ )$

We will model $\underline{x}1$ and $\underline{x}2$ as two independent variables.

Let $Q(\underline{x}) = q_1(\underline{x}1)\ q_2(\underline{x}2)$

(i) By Johnson-Shore's MCE principle:

Substitute the data from P and Q into (EQ 1) and obtain:

$$q_1(\underline{x}1) = N(\underline{m}1,\ R11 - R12\ R22^{-1}\ R21)$$

$$q_2(\underline{x}2)=N(\underline{m}2,\ R22-R21\ R11^{-1}\ R12\ )$$

$$\text{value of MCE}=0.5\log\frac{|R11|}{|R11-R12\ R22^{-1}\ R21|}$$

When $\underline{x}1$ and $\underline{x}2$ are approximately uncorrelated $R12=R21'\approx 0$, the value of MCE is close to 0 and the independence assumption is valid. When $\underline{x}1$ and $\underline{x}2$ are highly correlated, the value of MCE is large and the separable approximation is poor. The goodness of the separable model heavily depends on R12, because the variance of the separable model is proportional to the quadrature of R12 or R21.

(ii) By Kullback's minimum discriminant principle:

Substitute the data from P and Q into (EQ 3) to obtain:

$$q_1(\underline{x}1)=N(\underline{m}1,\ R11\ )$$

$$q_2(\underline{x}2)=N(\underline{m}2,\ R22\ \ )$$

In this case the minimum values are the same for both H(Q,P) and KDF. And the separable variance obtained by the KDF method is always no less than that obtained by the MCE. method.

Example #2:

Now we derive the formula for the special case where M=N and T is an invertible orthogonal matrix.

By definition: $TT' = T'T = I$; I is an identity matrix.

Then Ry is : $Ry = T\ Rx\ T'$

$$Ry = T^{-1}\ Rx^{-1}\ T'$$

Let

$$T = \begin{pmatrix} \underline{t}1 \\ \vdots \\ \underline{t}i \\ \vdots \\ \underline{t}p \end{pmatrix}$$; where $\underline{t}i$ is a Mi by N submatrix.

i.e. $\underline{y}_i = \underline{t}i\ \underline{x}$

Substituting the above data in (EQ 1,3), we get:

By the MCE principle:

$$q_i(\underline{y}_i) = N(\underline{my}_i\ ,\ [\underline{t}i\ Rx^{-1}\ \underline{t}i'\ ]^{-1}) \qquad \text{(EQ 5)}$$

By KDF:

$$q_i(\underline{y}_i) = N(\underline{my}_i\ ,\ \underline{t}i\ Rx\ \underline{t}i'\ ) \qquad \text{(EQ 6)}$$

Note that the density estimator for $\underline{y}_i$ depends only on the linear transformation $\underline{t}i$ that generated $\underline{y}_i$, not on any other

$\underline{t}j$. This is because T is orthogonal.

Example #3:

In this example we will derive the formulas when the T matrix in example #2 is invertible but not orthogonal. When T is not orthogonal, then

$Ry = TRxT'$ and

$$Ry = T'^{-1}\, Rx^{-1}\, T^{-1}.$$

Let the inverse of T be partitioned as follows:

$$T^{-1} = \left(\underline{t}1^{-1} \mid \underline{t}2^{-1} \mid \ldots \mid \underline{t}p^{-1} \right)$$

; where $\underline{x} = T^{-1}\, \underline{y} = \sum_{i=1}^{p} \underline{t}i^{-1}\, \underline{y}i$.

$\underline{t}i^{-1}$ is a N by Mi submatrix of T^{-1}.

$$T'^{-1} = \begin{pmatrix} (\underline{t}1^{-1})' \\ \vdots \\ (\underline{t}p^{-1})' \end{pmatrix}$$

; where $\underline{t}i^{-1}\, \underline{t}i = I$,

$\underline{t}j^{-1}\, \underline{t}i = 0$ for $i \neq j$.

$\underline{t}i^{-1}$ is orthogonal to all $\underline{t}j$ for $i \neq j$, and has a unit projection on $\underline{t}i$.

Then,

By Johnson-Shore's MCE:

$$q_i(\underline{y}_i) = N(\underline{my}_i, [(\underline{ti}^{-1})' \; Rx^{-1} \; \underline{ti}^{-1}]^{-1}) \qquad \text{(EQ 7)}$$

By Kullback's minimum discriminant:

$$q_i(\underline{y}_i) = N(\underline{my}_i, \underline{ti} \; Rx \; \underline{ti}') \qquad \text{(EQ 8)}$$

Note that the Johnson-Shore solution for the $i^{\underline{th}}$ variance depends on $\underline{ti}^{-1}$, which in turn depends on the choice of all the linear transformations $\underline{t}1, \underline{t}2\ldots,\underline{t}p$. The Kullback solution depends only on $\underline{t}i$.

Section 2.2: Power Spectrum Estimation

Now we can use the previous results for estimating power spectra. The physical meaning for all the random variables is given as following.

Let $\underline{x}_i = \underline{x}(\underline{t}_i)$ be a set of samples at time $\underline{t}_i$ of a wide sense stationary GRP with zero mean and covariance $R(\underline{t})$. In this case $\underline{t}_i' = [t1_i, t2_i, \ldots, tD_i]$ and $\underline{x}(\underline{t})$ is a D-dimensional Ni vector GRP.

Each $\underline{x}_i$ is an Ni dimensional column vector with

$$\underline{mx}_i = E(\underline{x}_i) = 0 \quad \text{and}$$

$$[Rx]ij = E(\underline{x}_i \underline{x}_j') = R(\underline{t}_i - \underline{t}_j) \; ; \; j,i=1,\ldots,L \; .$$

Let $\underline{x}' = [\underline{x}_1', \ldots, \underline{x}_i', \ldots, \underline{x}_L']$

The PDF of $\underline{x}$ is $N(\underline{0}, Rx)$, where

Rx is a LNi by LNi covariance matrix of $\underline{x}$. Let N=LNi.

Let the rows, $\{\underline{t}i; i=1,p\}$, of the transformation matrix T be a set of disjoint narrow bandpass filters. Then, the outputs $\underline{y}_i$ of the filters are independent random variables according to the GRP assumption. Their variances can be thought of as the power spectrum when the filters are very narrow in their pass band. Since the filters are finite in length, they can not be ideal, narrow, bandpass filters, and the $\{\underline{y}_i : i=1,p\}$ can not be independent exactly. We now model $\{\underline{y}_i; i=1,p\}$ as independent random variables. Assume T has rank $pNi=M \leq N$.

Then, $P(\underline{y}) = N(\underline{0}, Ry)$, where $Ry = TRxT'$ and

Ry is a M by M covariance matrix.

According to our model

$\underline{y}_i$ is independent of all others, then we get:

(i) By Johnson-Shore's MCE (EQ 1):

$$q_i(\underline{y}_i) = N(\underline{0}, [(Ry^{-1})ii]^{-1})$$

If M=N, then we use (EQ 7) and get:

$$q_i(\underline{y}_i) = N(0, [(\underline{t}i^{-1})' \; Rx^{-1} \; (\underline{t}i^{-1})]^{-1}). \qquad \text{(EQ 9)}$$

If M=N and T is orthogonal, then we get:

$$q_i(\underline{y}_i) = N(\underline{0}, [\underline{t}_i \, Rx^{-1} \, \underline{t}_i']^{-1}) \quad . \qquad \text{(EQ 10)}$$

(ii) By Kullback's minimum discriminant:

$$q_i(\underline{y}_i) = N(\underline{0}, [Ry]ii), \text{ where } [Ry]ii = \underline{t}_i \, Rx \, \underline{t}_i' \qquad \text{(EQ 11)}$$

We will discuss more on the above three equations and look for a good spectral estimator. All the three formulas fulfil the positive definite requirement and can be spectral estimators. Since our method can only estimate the power spectrum at a finite number of frequencies, we are very concerned with the spectrum at the other frequencies. An easy way to do this is to generalize the formula for finite frequencies to other frequencies when the formula can be written as a function of frequency. Obviously, (EQ 9) is not a good choice for spectral analysis, because the spectrum depends on a particular set of filters in T. (EQ 10,11) are both capable of doing this.

If the disjoint bandpass filters are design by TW=I, where I is an identity matrix and W has submatrices

$$Wik = e^{j\underline{w}_i' \, \underline{t}_k} \, I \; ;\{i=1,p;k=1,L\},$$

(EQ 9) is identical to MLM. With this kind of T (EQ 9) will be as good as the other two. The reason is that the matrix T is just a discrete Fourier transform (DFT) matrix, and is therefore orthonormal for uniform samples, W=T'. The set of

filters in both T and W are narrow bandpass with little overlap in the frequency domain. Unfortunately, this simple reason does not carry over for non-uniform samples.

(EQ 11) reveal that we are free to design a set of narrow banpass filters to get a spectrum, because the spectrum estimated by each filter will not be related to any others. When we use an adaptive filter (formula (12) in [9]), $\underline{t}=R^{-1}\underline{e}/(\underline{e}'R^{-1}\underline{e})$; $\underline{e}$ is a sinusoidal vector, (EQ 11) is equal to MLM. We now discuss two special cases and the meaning of (EQ 1).

Special Case #1:

Whenever the finite Fourier transformation can be thought of as a set of good bandpass filters, we can use the above equations (EQ 9,10,11) to obtain the following results. This transformation allows us to rewrite the $\underline{y}_i$ as follows.

Let $\underline{y}_i=\underline{X}(\underline{w}_i)$ be the finite Fourier transform of the known data samples at specific frequencies $\{\underline{w}_1, \underline{w}_2, \ldots, \underline{w}_p\}$, where $\underline{w}_i'=[w1_i, w2_i, \ldots, wD_i]$. Then,

$$\underline{y}_i = \underline{X}(\underline{w}_i) = \sum_{k=1}^{L} \underline{x}(\underline{t}_k)\, e^{j\underline{w}_i' \underline{t}_k} \quad ; j^2 = -1 \ .$$

Thus $T_{ik} = e^{j\underline{w}_i' \underline{t}_k} I$.

If M=N and T is an invertible orthogonal transformation, such as uniform sampling in space and frequency, then we use (EQ 10) and get the following solution by MCE:

$$q_i(\underline{X}(\underline{w}_i)) = N(\underline{0}, [\underline{t}_i R_x^{-1} \underline{t}_i']^{-1}), \text{ where} \qquad \text{(EQ 12)}$$

$$[\underline{t}_i R_x^{-1} \underline{t}_i'] = \sum_{m=1}^{L} \sum_{n=1}^{L} [R_x^{-1}]_{mn} e^{j\underline{w}_i' (\underline{t}_m - \underline{t}_n)} .$$

In this case the $[\underline{t}_i R_x^{-1} \underline{t}_i']^{-1}$ correspond to that of MLM [9]. Since (EQ 12) is a function of frequency, this suggests using (EQ 12) to estimate the whole spectrum.

If p=1 and L>p, then from (EQ 1)

$$q_1(\underline{X}(\underline{w}_1)) = N(\underline{0}, [R_y^{-1}]^{-1}) = N(\underline{0}, R_y),$$

where $R_y = TR_xT' = \underline{t}_1 R_x \underline{t}_1'$. Expand R_y and get:

$$\underline{t}_1 R_x \underline{t}_1' = \sum_{m=1}^{L} \sum_{n=1}^{L} R_{mn} e^{j\underline{w}_1' (\underline{t}_m - \underline{t}_n)}$$

$$= \sum_{m=1}^{L} \sum_{n=1}^{L} R(\underline{t}_m - \underline{t}_n) e^{j\underline{w}_1' (\underline{t}_m - \underline{t}_n)} .$$

When $\{t_1, .., t_L\}$ are uniformly spaced, $\underline{t}_i = i\underline{\Delta}$, and

$$[\underline{t}_1 R_x \underline{t}_1'] = \sum_{k=0}^{L-1} (L-k) R(k\underline{\Delta}) e^{j\underline{w}_1' k\underline{\Delta}}$$

This is the same solution as that given by Bartlett's method (triangle window).

The solution by Kullback's minimum discriminant is:

$$q_i(\underline{X}(\underline{w}_i)) = N(\underline{0}, [Ry]ii),$$

which is also same as that given by Bartlett's method.

Since the estimation of spectra by the windowed periodogram method is popular, we discuss how to incorporate a window into (EQ 12). Let $\tilde{T}ki = Wi\ Tki$, where $Wi = hi\ I$; hi is a scalar, I is the identity matrix and Tki is the same as before. {Wi, i=1,L} are the window coefficients.

Let $W = \begin{pmatrix} W1 & & & \\ & W2 & & 0 \\ & & \ddots & \\ & 0 & & WL \end{pmatrix}$ where all of the off-diagonal submatrices are 0.

Replacing Tki with $\tilde{T}ki$ in (EQ 12) and (EQ 11) gives:

$$[Ry^{-1}]ii = \underline{t}i\ W^{-1}\ Rx^{-1}\ W'^{-1}\ \underline{t}i' = (\underline{t}i\ W^{-1})\ Rx^{-1}\ (\underline{t}i\ W^{-1})'$$

$$= \sum_{m=1}^{L}\sum_{n=1}^{L} [Rx^{-1}]mn\ hm^{-1}\ hn^{-1}\ e^{j\underline{w}'(\underline{t}_i - \underline{t}_m + \underline{t}_n)}$$

This works poorly, unless we replace hm^{-1} with hm.

$$[Ry]ii = \underline{t}i\ W\ Rx\ W'\ \underline{t}i' = (\underline{t}i\ W)\ Rx\ (\underline{t}i\ W)'$$

$$= \sum_{m=1}^{L}\sum_{n=1}^{L} [Rx]mn\ hm\ hn\ e^{j\underline{w}'(\underline{t}_i - \underline{t}_m + \underline{t}_n)}$$

Since W^{-1} is also a diagonal matrix, it has the inverse of

the corresponding diagonal elements of W as its diagonal elements.

Special Case #2:

When the irregular sampling time {tn} does not allow the design of a good bandpass filter, the formulas we developed will be useless. In order to remedy this defect, we have to remodel x(tn) to meet the assumption of independence through some way other than bandpass filters. Certainly, the context will lose consistency by remodeling x(tn). However, the new modeling procedure will have the same spirit as the previous aim. We will use the single channel one dimension signal x(tn) as an example to illustrate this new modeling procedure. It is easy to generalize this example to multichannel multidimensional signals with some notational complexity. In this case we will estimate the power spectrum at one frequency. The signal is assumed to have the form: x(tn)= {term #1} + {term #2}. We attempt to build a model Q, Q({x(tn)})= q1(term #1) q2(term #2). Because the MCE principle requires independence between term #1 and term #2, we must arrange them to be as independent as possible. Since we are interested in spectral analyses, the two terms in x(tn) are arranged in the following ways.

Let $\underline{e}' = [\, e^{jwt1}, e^{jwt2}, \ldots, e^{jwtN} \,]$ and

$\underline{x}' = [\, x(t1), x(t2), \ldots, x(tN) \,]$.

Arrange the terms as follows:

$$x(tn) = \{ a(w)\, e^{-jwtn} \} + \{ \tilde{x}(tn) \} \qquad \text{(EQ 13)}$$

$$x(tn) = \{ [a(w)+\tilde{a}(w)]\, e^{-jwtn} \} + \{ \bar{x}(tn) \} \qquad \text{(EQ 14)}$$

Where $\tilde{a}(w) = \underline{e}' \cdot \tilde{\underline{x}}$, $\underline{e}' \cdot \bar{\underline{x}} = 0$ and

$\bar{x}(tn)$ can be represented by a subspace $\bar{\underline{e}}$ which is

orthogonal to $\underline{e}$. (EQ 13) can be thought of as a signal plus a correlated noise. (EQ 14) can be thought of as a modified signal plus an uncorrelated noise. Obviously, (EQ 14) is a better choice for our model, because (EQ 14) makes independence of the terms likely. Now we construct the matrix T:

Let $T = \begin{pmatrix} \underline{e}' \\ \hline \text{subspace } \bar{\underline{e}} \\ \text{orthogonal} \\ \text{to } \underline{e}' \end{pmatrix}$ and $\underline{t}1' = \underline{e}'$.

We formulate the Q for $\underline{y} = T\underline{x}$. So, $y1 = \underline{t}1'\underline{x} = \underline{e}'\underline{x} = a(w)+\tilde{a}(w)$ and $Ry = TRxT'$, where $Rx = E[\underline{x}\underline{x}']$ and $Ry = E[\underline{y}\underline{y}']$. The variance of $a(w)+\tilde{a}(w)$ can possibly represent the spectrum of x(tn) at frequency w. Now our model has the form: $Q(\underline{y}) = q1(y1)\,q2(\{yk; k \neq 1\})$. Apply the MCE principle and get:

$$S(w) = Var(y1) = Var\{a(w)+\tilde{a}(w)\} = \{\underline{t}1'\, Rx^{-1}\, \underline{t}1\}^{-1} = \{\underline{e}'\, Rx^{-1}\, \underline{e}\}^{-1}$$

; which is still (EQ 12) and MLM.

In the above formula we can see that the $\underline{e}$ vector is not a bandpass filter. When a vector $\underline{e}$ is also a good narrow bandpass filter, this $\underline{e}$ is meaningfull. This also suggests that whenever we can not design a good narrow bandpass filter $\underline{t1}$ to estimate the spectrum at w, we still can use $\underline{e}$ or MLM to obtain the spectrum.

The result of using KDF is:
$S(w)=\underline{e}'Rx\underline{e}$. Note that this works poorly.

In this case we remodel the x(tn) and the result can explain why MLM still works reasonably even when the irregularly spaced sampling does not allow us to design a good bandpass filter $\underline{t1}$.

Meaning of (EQ 1):

We now discuss the meaning of the formula (EQ 1), so that we can precisely know the relation between our theory and that for the linear least square estimation (LLSE). This relation will allow us reach the formula (EQ 1) by knowing LLSE only. In the following analysis, the Ry has the following partition form. We assume every yi is a single random variable for simplicity.

Let $\underline{y}=[y1,y2,\ldots,yN]=[y1, \underset{\sim}{\underline{y1}}]$; where

$\underline{yi}=[y1,y2,..,yi-1,yi+1,..,yN]=[\{yk;k\neq i\}]$ and $yi=\underline{y}_i$.

Let $Ry=E[\underline{y}\underline{y}']$, $\underline{y}=T\underline{x}$. If i=1, then

$$Ry=\begin{pmatrix} Ry11 & \tilde{Ry1} \\ \tilde{Ry1}' & \tilde{Ry11} \end{pmatrix};$$

where $Ryii= \underline{t}i'Rx\ \underline{t}i$,

$\tilde{Ryi}=E(yi\ \underline{y}i')$ and

$\tilde{Ryii}=E(yi\ \underline{y}i')$.

$\tilde{Ry11}$ can be thought of as the covariance of noise and Ry11 is the covariance of the signal.

The MCE's result for qi(yi) is $qi(yi)=N(0,\{\ [Ry^{-1}]ii^{-1}\ \})$.

$\{[Ry^{-1}]ii^{-1}\}$ is equal to $Ryii-\tilde{Ryi}\{\tilde{Ryii}\}^{-1}\tilde{Ryi}'$, which can be obtained by manipulating the matrix Ry.

We now discuss the meaning of si, where

$$si=\{[Ry^{-1}]ii^{-1}\}=Ryii-\tilde{Ryi}\{\tilde{Ryii}\}^{-1}\tilde{Ryi}'. \quad \text{(EQ 15)}$$

Obviously, si is equal to the error covariance Var(error), where Var(error)=Var(yi-$\hat{y}$i) and $\hat{y}$i is the linear estimation of yi given {yk;k≠i}. And this error is independent of the rest of the variables {yk;k≠i}. This means the si obtained for yi through the MCE is the energy (variance) which are perpendicular to (independent of) the variables {yk;k≠i}. (EQ 15) also tells us that the si are

proportional to the quadrature of the cross-correlation matrix E{yi [{yk;k≠i}]}. So, when the GRP $\underline{x}(\underline{t}n)$ can not be separated into independent parts properly, the result obtained through MCE will deviate from its original meaning. The above interpretation also shows that we can reach the MCE result with a common linear least square estimate.

The above idea can be modifed when $\underline{y}i$ is a vector. In this case si is a positive matrix. We say matrix A is less than matrix B when $\underline{v}'A\underline{v} < \underline{v}'B\underline{v}$ for any vector $\underline{v}$.

From the above discussion and the meaning in case #2, we may use a well-designed filter/vector $\underline{g}$ to represent the appearance of a signal. For instance, when $\underline{g}$ is the vector (or the signature of a signal) which will make this signal distinguishable from its background, the energy in $\underline{g}$ will be a good indicator for the appearance of this signal. This idea plus the idea that the MLM filter can make the Bartlett method as good as MLM encourages us to use the MLM filter, formula (12) in [9], in (EQ 14) to indicate the appearance of a sinusoidal signal $\underline{e}$. This filter is $\underline{\tilde{e}} = (R^{-1}\underline{e})/(\underline{e}'R^{-1}\underline{e})$. Replacing the $\underline{\tilde{e}}=\underline{t}1$ in (EQ 13&14 or 12) with $\underline{e}$, we get:

$$\text{Var}(y1)= \frac{(\underline{e}'R^{-1}\underline{e})^2}{(\underline{e}'R^{-3}\underline{e})},$$ which shall be defined as the 'indicator'.

We now compare some results of using this indicator with those using three other methods. In figures #1 to #6

we plot results for the following four methods.
They are:

$$N^{-2}\,\underline{e}'R^{-1}\underline{e}\;;\qquad \frac{1}{\underline{e}'R^{-1}\underline{e}}\;;\qquad \frac{(\underline{e}'R^{-1}\underline{e})}{\underline{e}'R^{-2}\underline{e}}\;;\qquad \frac{(\underline{e}'R^{-1}\underline{e})^{2}}{\underline{e}'R^{-3}\underline{e}}$$

Bartlett MLM Lagunas[10] indicator

Note that whenever the minimum eigenvalue of the matrix R is close to zero, adding extra white noise to R is very helpful for the numerical computation of Lagunas's spectra and the indicator. This extra white noise should be subtracted after the computation. In figure #1 the estimated spectra by these 4 methods are plotted for the the correlation function sampled at 11 equally spaced lags, {r(t)= δ(t)+ 5.33cos(0.3πt)+ 10.66cos(0.4πt); where t=0,1,2,...,10}. This correlation function is the same as that used in [9]. The signal-to-noise ratios in r(t) are 7.26 and 10.27 dB. In figure #2 we use this r(t) but sampled at unequally spaced lags, namely the differences between all possible pairs of the following numbers: 0, 1.9, 2.76, 3.78, 4.08, 4.81, 4.98, 5.73, 7.91, 8.05, 10.0. Figure #3 shows the spectra for this r(t), computed at lags which are the differences divided by 1.27 between any pair of the following numbers: 0, 0.1, 0.2, 0.3, 0.5, 0.7, 1.5, 3.1, 6.3, 10.0, 12.7. Figure #4 shows the spectra for {r(t)+14 δ(t); t=0,1,..,10}, where the white noise increases from 1 to 15. The signal-to-noise ratios are -4.49 and

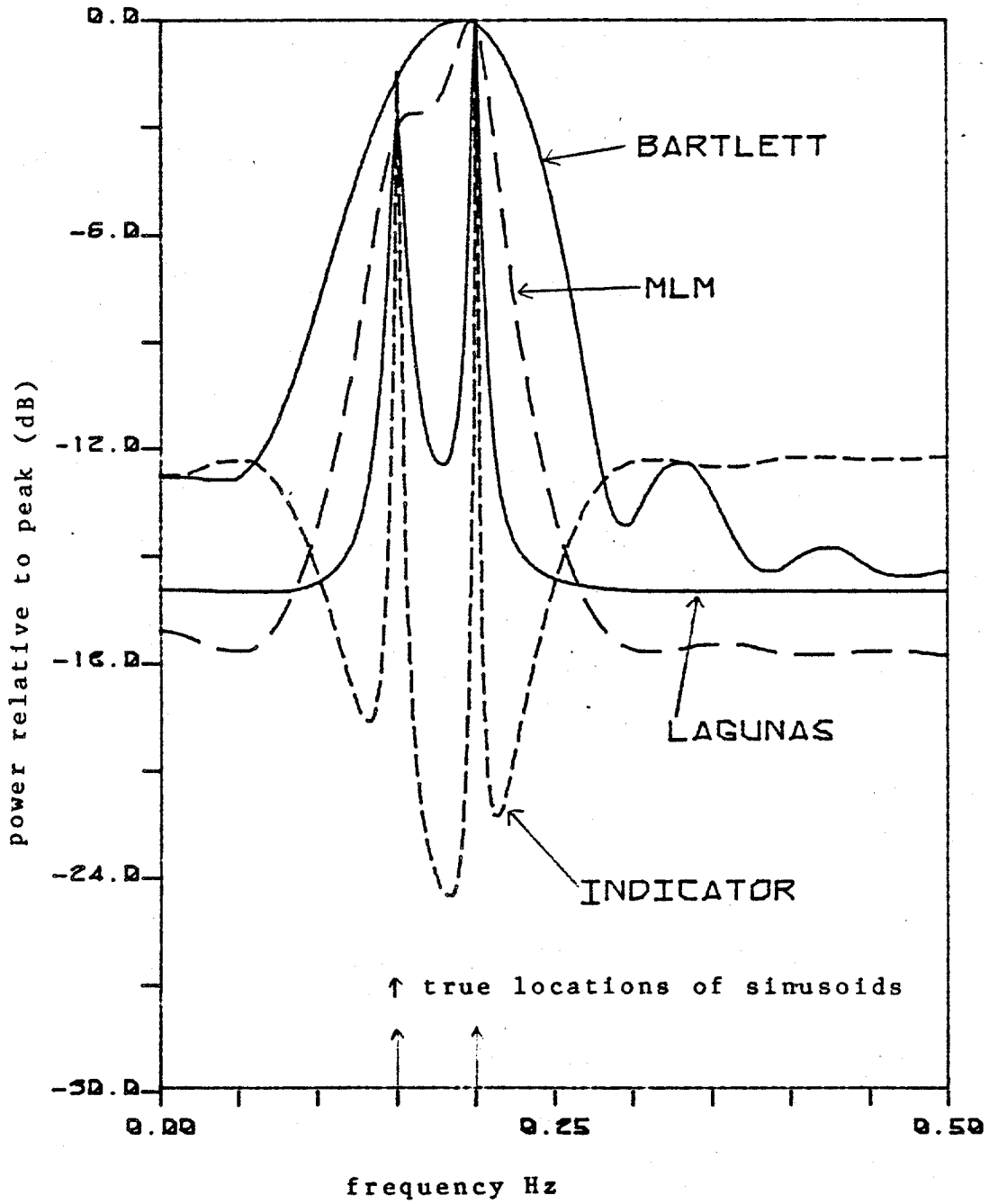

Figure #1: spectra for $\{r(t)=\zeta(t)+5.33\cos(0.3\pi t)+10.66\cos(0.4\pi t);t=0,1,2,\ldots,10.\}$

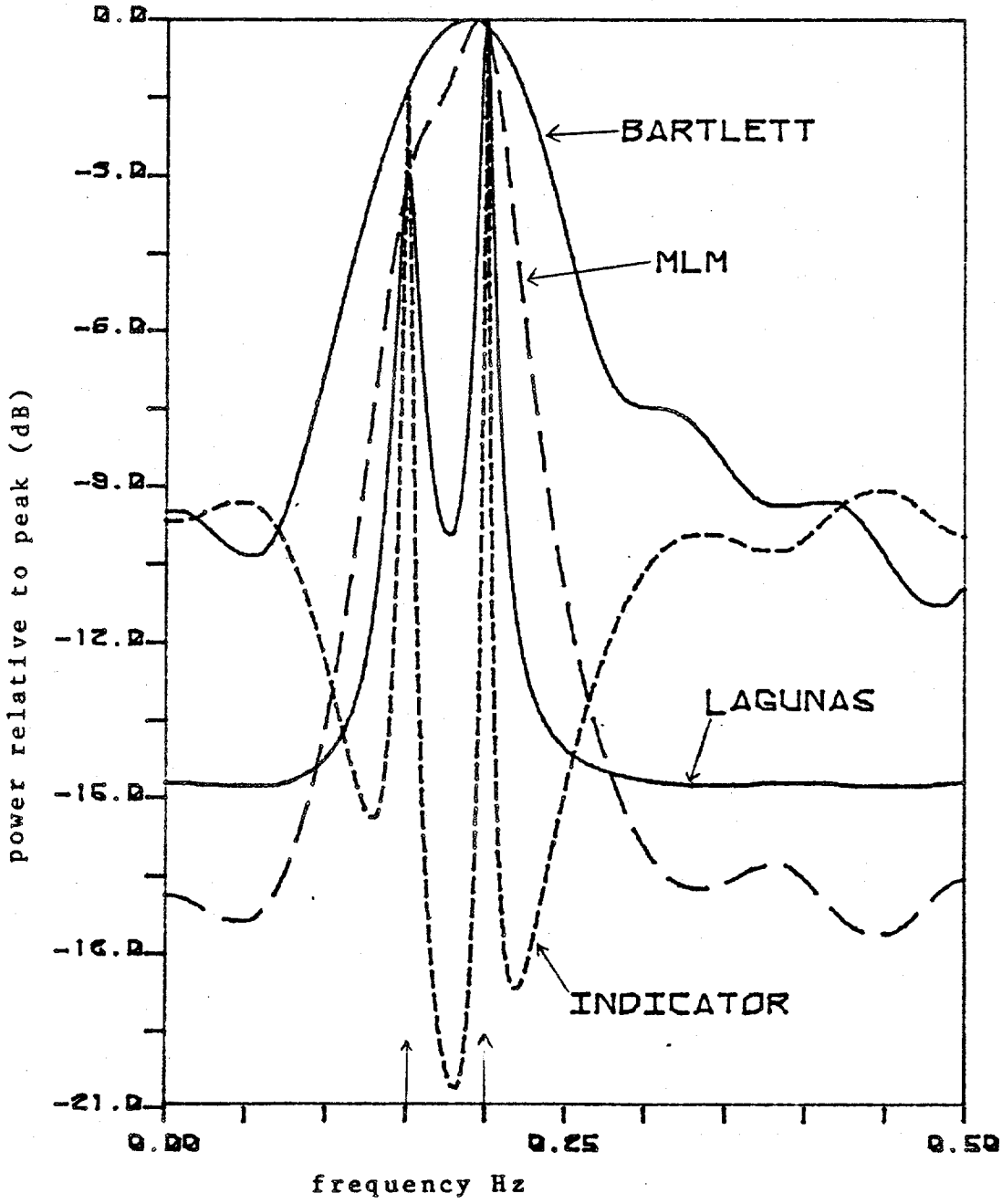

Figure #2: spectra for {r(t)=ȝ(t)+5.33cos(0.3πt)
+10.66cos(0.4πt);t=ti-tj;i,j=1,2,..11} where ti=
[0,1.9,2.76,3.78,,4.08,4.81,4.98,5.73,7.91,8.05,10]

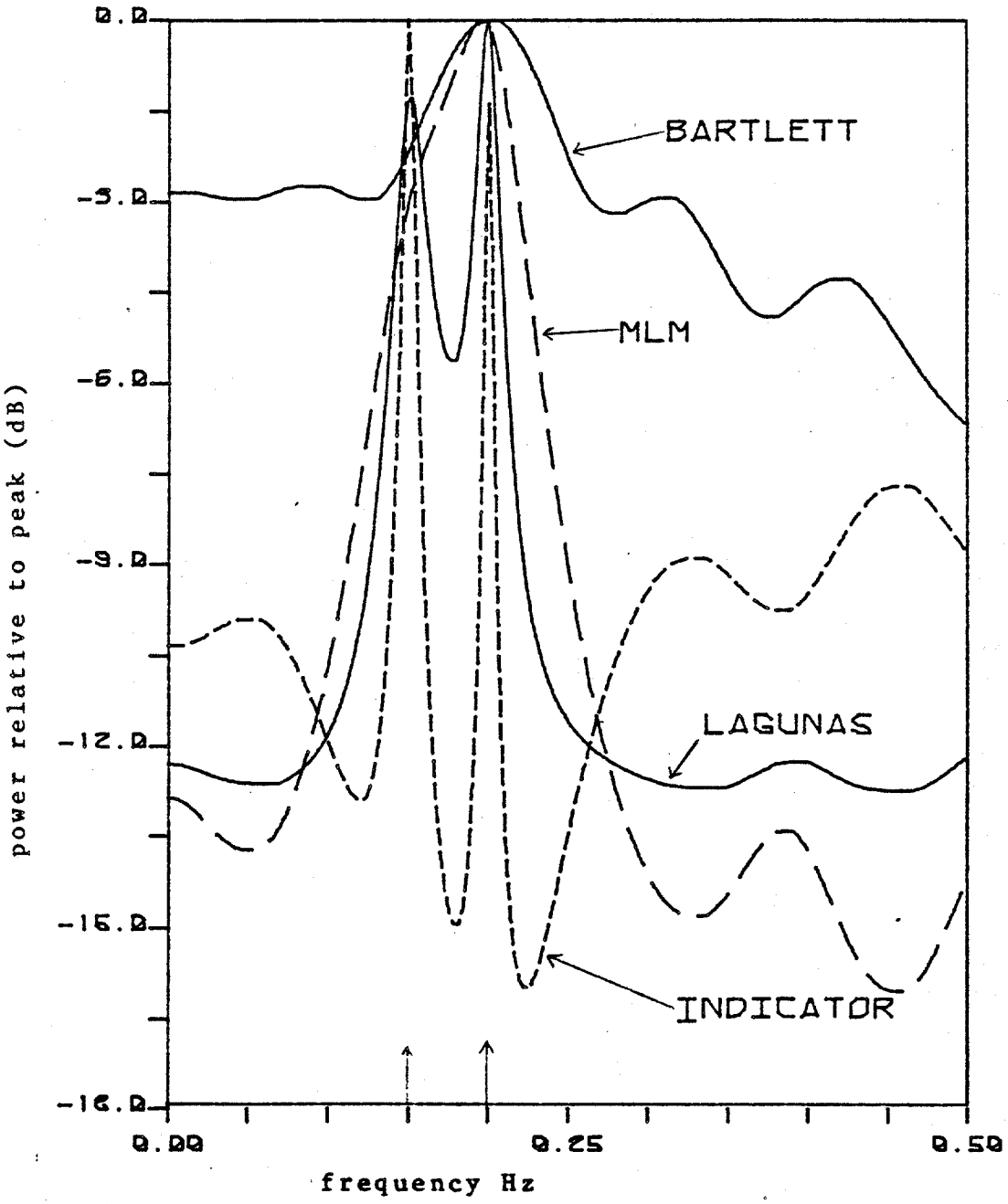

Figure #3: spectra for {r(t)=δ(t)+5.33cos(0.3πt)
+10.66cos(0.4πt);t=(ti-tj)/1.27 i,j=1,2,..,11}
ti=[0,0.1,0.2,0.3,0.5,0.7,1.5,3.1,6.3,10,12.7]

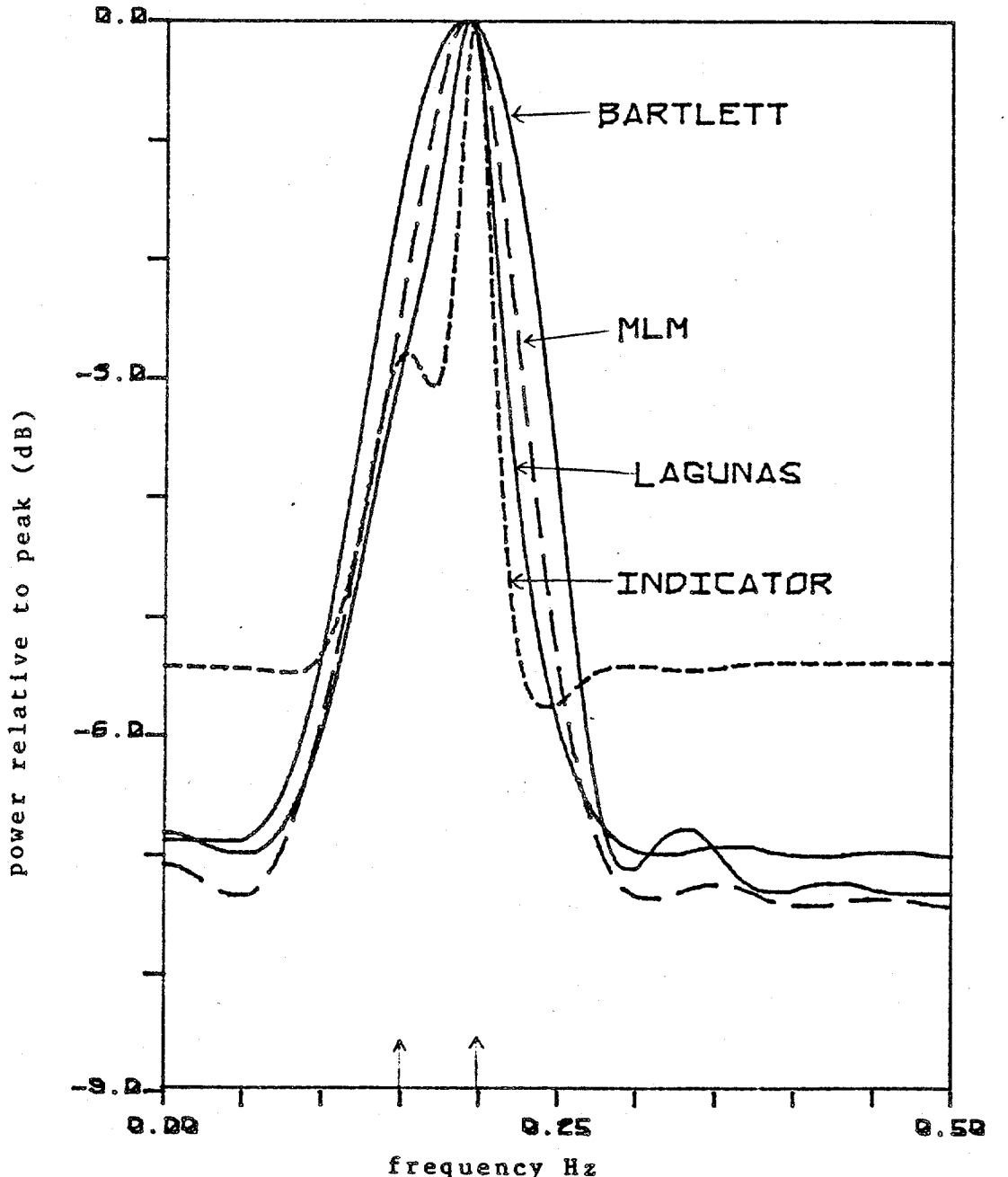

Figure #4: spectra for $\{r(t)=15\delta(t)+5.33\cos(0.3\pi t)+10.66\cos(0.4\pi t);t=0,1,2,\ldots,10.\}$

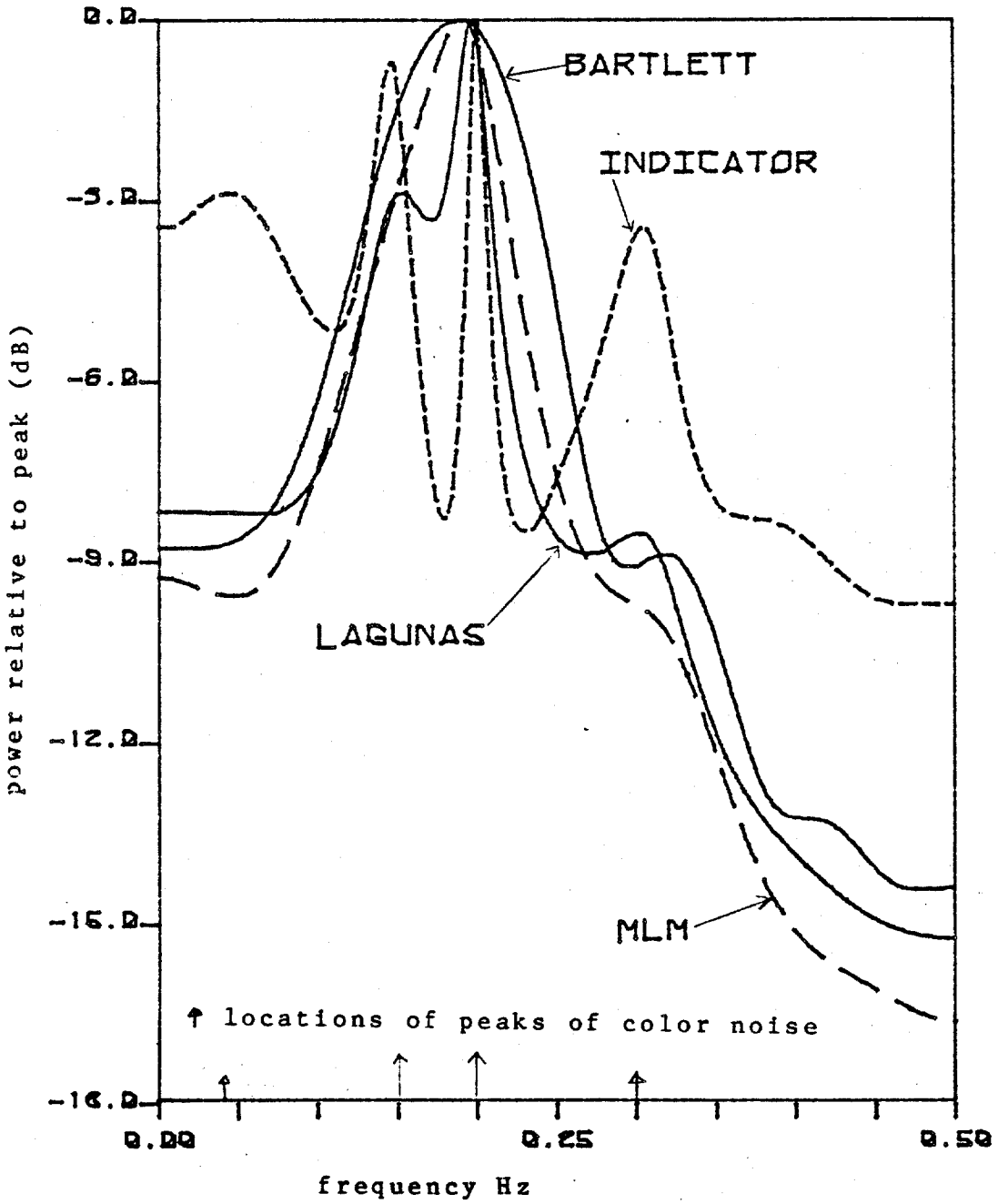

Figure #5· spectra for {r(t)=ζ(t)+5.33cos(0.3πt) +10.66cos(0.4πt)+color noise;t=0,1,2,...,10.}

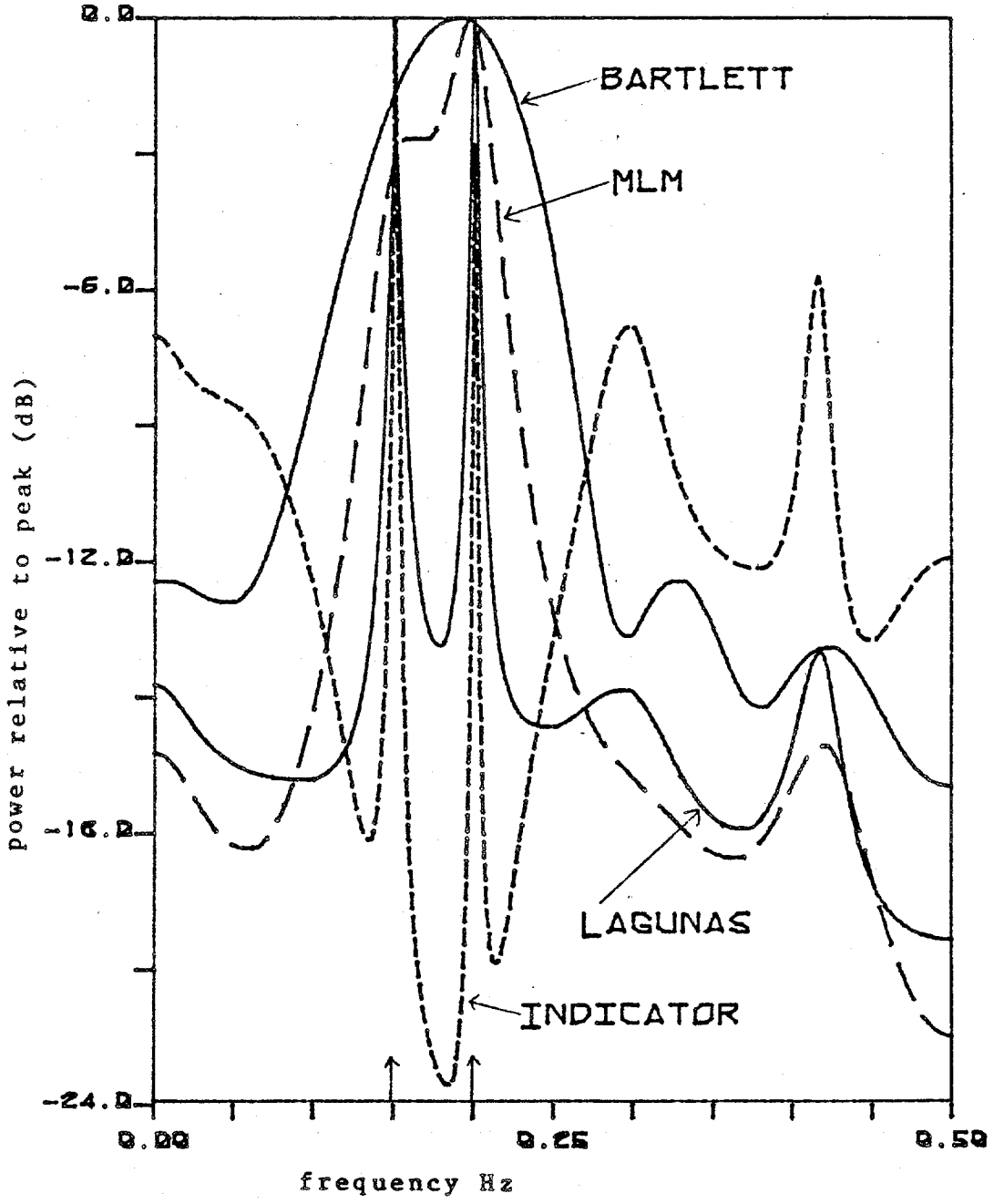

Figure #6: spectra for {r(t)=ξ(t)+5.33cos(0.3πt)
+10.66cos(0.4πt)+n(t);t=0,1,2,...,10.}
n(t): 11 random numbers uniformly distributed
between -0.25 and 0.25

-1.48 dB. We also include the spectra with colored noise in figure #5. The correlation function used in this figure is:

$$r(t)+ 2\, e^{-0.4t}\left[\cos(0.2\pi t)+ \frac{0.4}{0.2\pi}\sin(0.2\pi t)\right]$$

$$+ 2\, e^{-0.2t}\left[\cos(0.6\pi t)+ \frac{0.2}{0.6\pi}\sin(0.6\pi t)\right] ;$$

where t=0,1,2,...10.

The colored noise is constructed as the sum of two independent wide-band processes. Each of the two independent processes has a spectrum which could be obtained from a simple RLC circuit driven by white noise. The peaks of these two spectra are at 0.0435 and 0.296 Hz approximately. These peaks are explicitly indicated by the indicator only. In figure #6 the spectra are obtained for the perturbated correlation function, r(t)+n(t);t=0,1,2,...,10, where the n(t) is a sequency of random numbers with a zero mean and uniform distribution between -0.25 and 0.25. The extra humps in this figure indicate the possible appearance of extra sinusoidal components caused by adding n(t). In all these figures the two sinusoidal signals are always distinguishable through using the indicator's formula. Our simulated results show that this indicator can easily distinguish sinusoidal signals but does not accurately estimate the magnitude of the spectrum or the whole shape of the spectrum. The reason why this indicator can sharply point out the sinusoidal

components is that this indicator heavily weights the eigenvector corresponding to the minimum eigenvalue of R. This reason is similar to that for Pisarenko's method, see page 106 in [5]. We also studied the pole-zero behavior of this indicator for the case of uniform samples by simulations. We found that this indicator can always place some of the zeros in between the significant poles and close to these poles. This is probably the reason why this indicator can separate/resolve the peaks so well and narrow the peaks. But it is hard to describe this behavior theoretically.

CHAPTER 3

APPLICATIONS

In this chapter two applications, and the cross spectral estimator will be discussed. We will introduce the cross spectral estimator in the first section followed by applications in modal analysis and frequency wavenumber estimation.

Section #1: Cross Spectral Estimation

Since the cross spectrum is very important in many applications, we discuss it first and show some of the results for two channels using simulated data at the end of this section. We will use (EQ 12) to estimate the cross spectrum throughout this chapter, because it always gives reliable results empirically. The other reason we prefer using (EQ 12) to estimate the cross spectrum is that it has an additional interesting interpretation.

For simplicity and clearness, we will use the two-channel-one-dimension case to interpret (EQ 12) using LLSE. This interpretation generalizes to the multichannel multidimensional case with some notation complexity. The problem statement is the following. Let $\underline{x}'$=[x1, x2,..., xi,..., xL] and $\underline{y}'$=[y1, y2,..., yi,..., yL], where xi and yi are the samples at time t=ti from the two channels, x(t) and

y(t). Let $\underline{hx}$=[hx1,.., hxi,.., hxL] and $\underline{hy}$=[hy1,.., hyi,.., hyL] be the two filters which we will apply to x(t) and y(t), where hxi and hyi are the coefficients of $\underline{hx}$ and $\underline{hy}$ at the time lag ti. We plan to use both $\underline{hx}$ and $\underline{hy}$ to find the quantity we want. Let s(tL) be the quantity s(tL)=u(tL)+v(tL),

$$\text{where } u(tL) = \sum_{i=1}^{L} hx(L-i)\ x(ti)$$

$$v(tL) = \sum_{i=1}^{L} hy(L-i)\ y(ti)$$

The idea is to adjust both $\underline{hx}$ and $\underline{hy}$ in such a way that s(t) is the desired quantity. This idea is formulated in the following way. Rearrange {hxi,hyi} into a new vector $\underline{h}$ and {xi,yi} into a new sampled series $\underline{z}$. Let $\underline{h}'$=[hx1,hy1, hx2,hy2, hx3,hy3,..., hxi,hyi,..., hxL,hyL] and $\underline{z}'$=[x1,y1, x2,y2, x3,y3,..., xi,yi,..., xL,yL]. Suppose we know the correlation matrix for $\underline{z}$, $E\{\underline{z}\underline{z}'\}=R$. One method of estimating the spectrum using s(t) is to impose an unbiased constraint on $\underline{h}$ at a frequency w and then minimize $S=E\{ss'\}$ in order to reject the influence from all other frequencies. This contraint is:

$\underline{h}'\underline{e}=\underline{c}'=[a,b]$, where a,b = 0,1 ,

$\underline{e}'=[e1', e2', e3',..., ei',...., eL']$ and $ei=e^{jwti}\ I$, where

I is the 2 by 2 identity matrix. With this constraint we want to find a vector $\underline{h}$ which has a minimum $S=E\{ss'\}=\underline{h}'R\underline{h}$.

The derivation is straightforward. The solution for $\underline{h}$ is:

$$\underline{h} = R^{-1}\,\underline{e}\,\{\,[\,\underline{e}'\,R^{-1}\,\underline{e}]^{-1}\,\}\,\underline{c}$$

When $\underline{c}'=[1,0]$, we get $\underline{h}\langle 1,0\rangle=\underline{h}$, $\underline{s}\langle 1,0\rangle=\underline{h}\langle 1,0\rangle'\underline{z}$ and

$$\min S = \underline{h}\langle 1,0\rangle' R\, \underline{h}\langle 1,0\rangle = [1,0]\,[\,\underline{e}'\,R^{-1}\,\underline{e}\,]^{-1} \begin{pmatrix} 1 \\ 0 \end{pmatrix}.$$

This minimum value of S is just the estimated spectrum for x(t) using (EQ 12).

When $\underline{c}'=[0,1]$, we get $\underline{h}\langle 0,1\rangle=\underline{h}$, $s\langle 0,1\rangle=\underline{h}\langle 0,1\rangle'\underline{z}$ and

$$\min S = \underline{h}\langle 0,1\rangle' R\, \underline{h}\langle 0,1\rangle = [0,1][\,\underline{e}'\,R^{-1}\,\underline{e}\,]^{-1} \begin{pmatrix} 0 \\ 1 \end{pmatrix}.$$

This minimum value of S is just the estimated spectrum for y(t) using (EQ 12).

Heuristically, we may use either the cross term $\underline{h}\langle 1,0\rangle'R\,\underline{h}\langle 0,1\rangle$ or $\underline{h}\langle 0,1\rangle'R\,\underline{h}\langle 1,0\rangle$ as a cross spectral estimator, as follows:

$$Sxy(w) = \underline{h}\langle 1,0\rangle' R\, \underline{h}\langle 0,1\rangle = [1,0][\,\underline{e}'\,R^{-1}\,\underline{e}\,]^{-1} \begin{pmatrix} 0 \\ 1 \end{pmatrix}$$

$$Syx(w) = \underline{h}\langle 0,1\rangle' R\, \underline{h}\langle 1,0\rangle = [0,1][\,\underline{e}'\,R^{-1}\,\underline{e}\,]^{-1} \begin{pmatrix} 1 \\ 0 \end{pmatrix}$$

Sxy(w) and Syx(w) are just the estimated cross spectra between x(t) and y(t) using (EQ 12). Another way to formulate this problem is: Let $U'(tL)=[\,u'(tL)\;v'(tL)\,]$ and

$$H(n) = \begin{pmatrix} hxx(n) & hxy(n) \\ hyx(n) & hyy(n) \end{pmatrix} .$$

Then, $U(tL) = \sum_{m=1}^{L} H(tL-tm) \begin{pmatrix} x(tm) \\ y(tm) \end{pmatrix}$

Let $H' = [\, H'(0), H'(1), .., H'(L-1) \,]$.

We want to find an H which has a minimum tr(H'RH) subject to the unbiased constraint $H'\underline{e}=I$. (tr(.) means trace.)

The solution for H is: $H = -R^{-1}\,\underline{e}\,(\underline{e}'R^{-1}\,\underline{e})^{-1}$

So, $H'RH = (\underline{e}'R^{-1}\,\underline{e})^{-1}$, which is identical to (EQ 12).

Note H has 3L variables while the previous $\underline{h}$ has 2L variables when we need to estimate the autospectrum only for one channel.

Figure #7 is a simulated example which shows how (EQ 12) works for estimating cross specra. In this figure the autocorrelation functions, rx(t) and ry(t), of both channels are the same as that used in figure #1. The cross correlation function rxy(t) is equal to rx(t) without white noise. The lags used are {t|t=-10,-9,...,0,.,10}.

Section #2: Modal Analysis

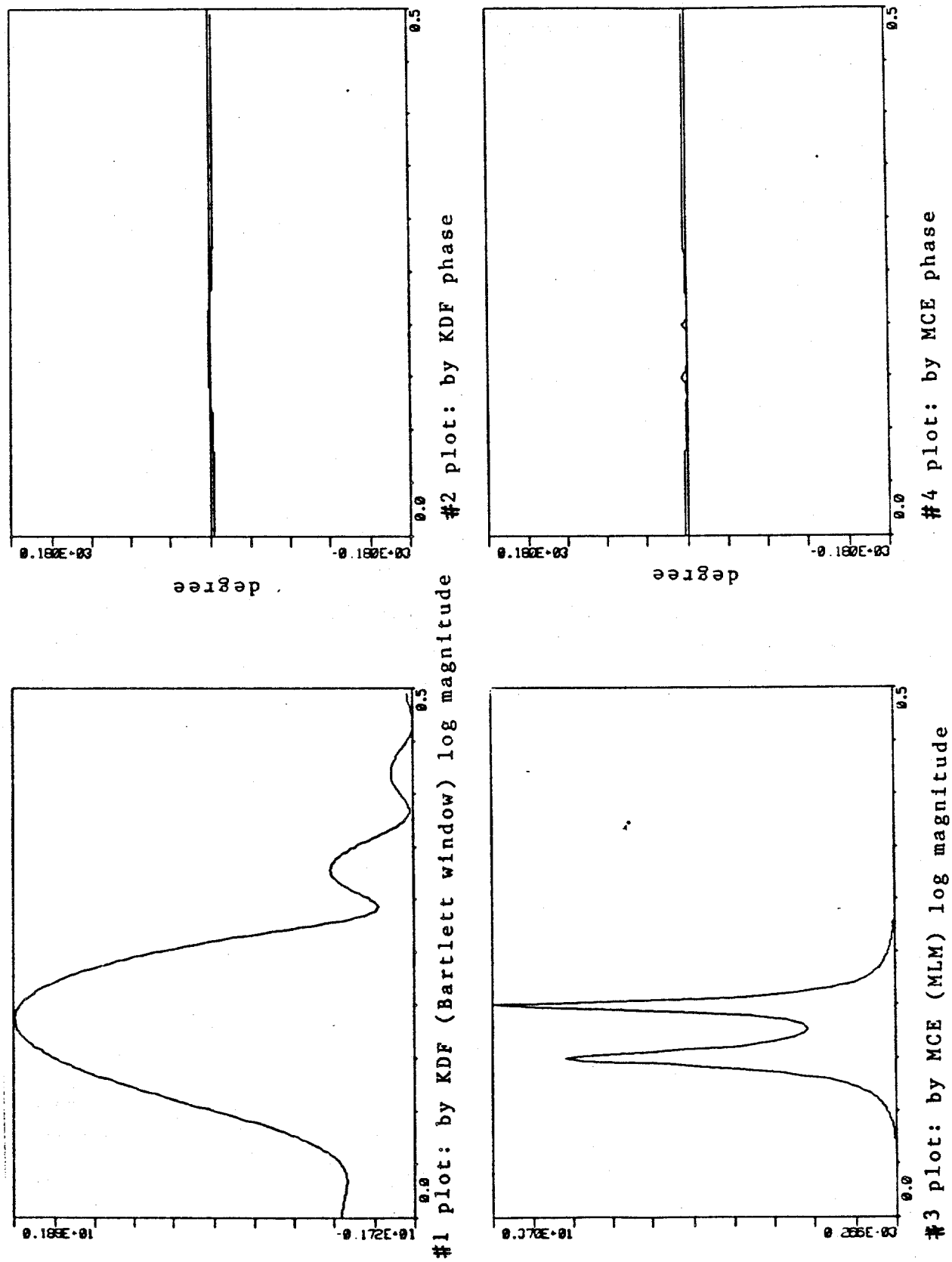

Figure #7: cross-spectra for {rx(t)=ry(t)=r(t)=δ(t)
+5.33cos(0.3πt)+10.66cos(0.4πt);t=0,1,2,...,10.}
{rxy(t)=5.33cos(0.3πt)+10.66cos(0.4πt);t=0,±1,±2,...,±10.}

In this section we will compare our cross spectral estimator with MEM using the acceleration data from sensors oriented in a northerly direction measured at the centers of 4 different decks in Amoco's single caisson as studied in [1]. The 4 records are NAH, NAP, NAW, and NAB, which were recorded at the helicopter, production, wellhead, and boat decks respectively. We will use the estimated correlation functions, figure #8 and #9, to estimate all the spectra in this section. All these correlation functions are estimated by the FFT method through averaging over 58 segments of 512 data points each. The sampling rate is 6.4 Hz and the total record length is 77.3 minutes or 29696 data points. Figure #10 plots the natural log (ln) values of the autospectra estimated by (EQ 12) for the helicopter (NAH), production (NAP), well (NAW) and boat decks. These four autospectra are obtained by using the two channel formula of (EQ 12) between NAH and each of NAP, NAW, and NAB. We plot only one spectrum for NAH, because the spectra for NAH are almost the same among the three cross spectra. All these spectra were estimated using 40 lags or 6.09375 seconds of the correlation functions. According to modal analysis, the small vibration of this caisson can be modelled approximately as the superposition of several natural modes. Each mode moves primarily at its own natural frequency and mode shape as detailed in [1]. The first and second mode peaks are easily identified in figure #10. Figures #11 and

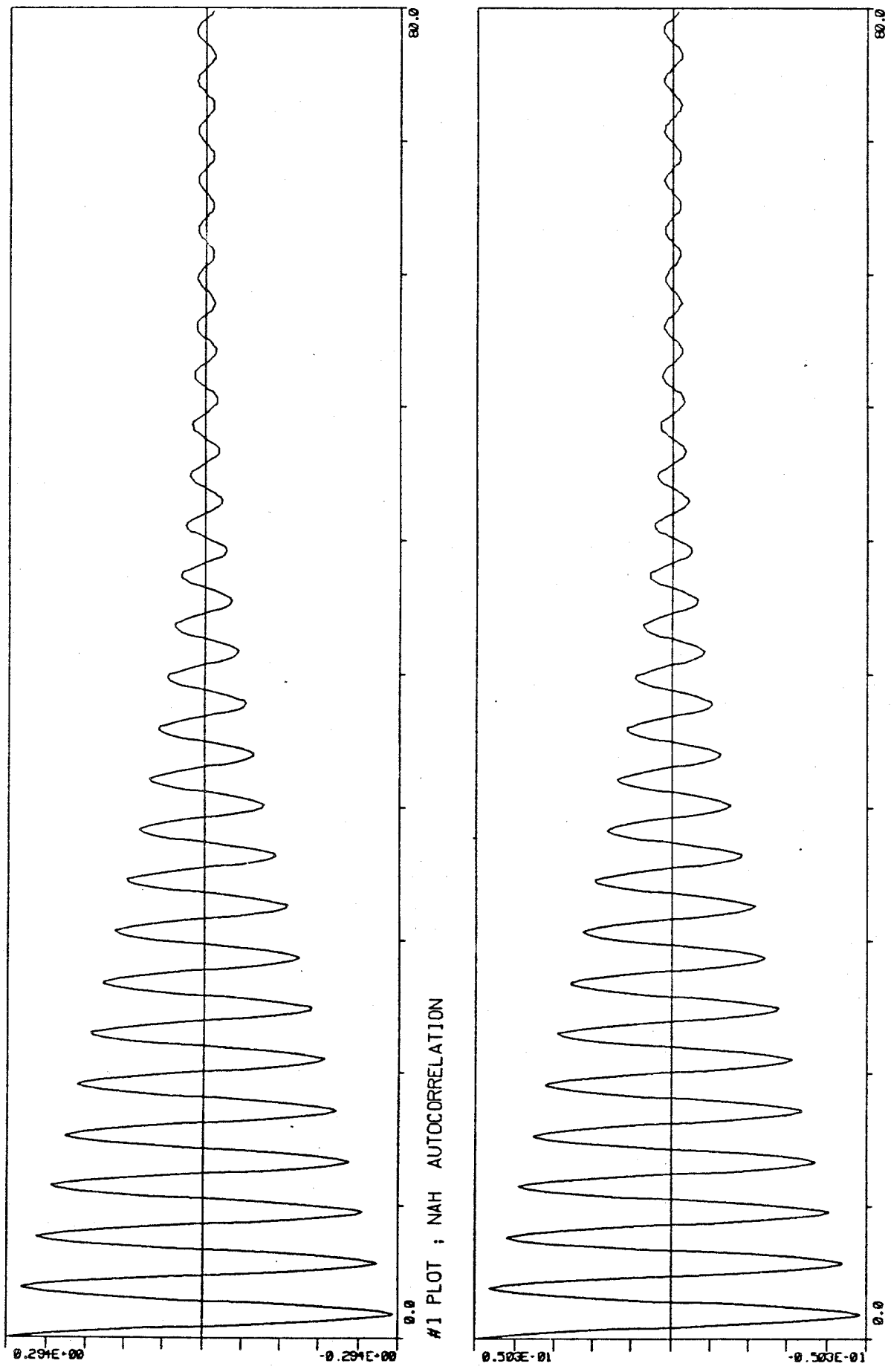

Figure #8: autocorrelation functions; unit of time=sec
data from files 'LOL2*.COR' ; sampling frequency=6.4Hz
total number of lags=512

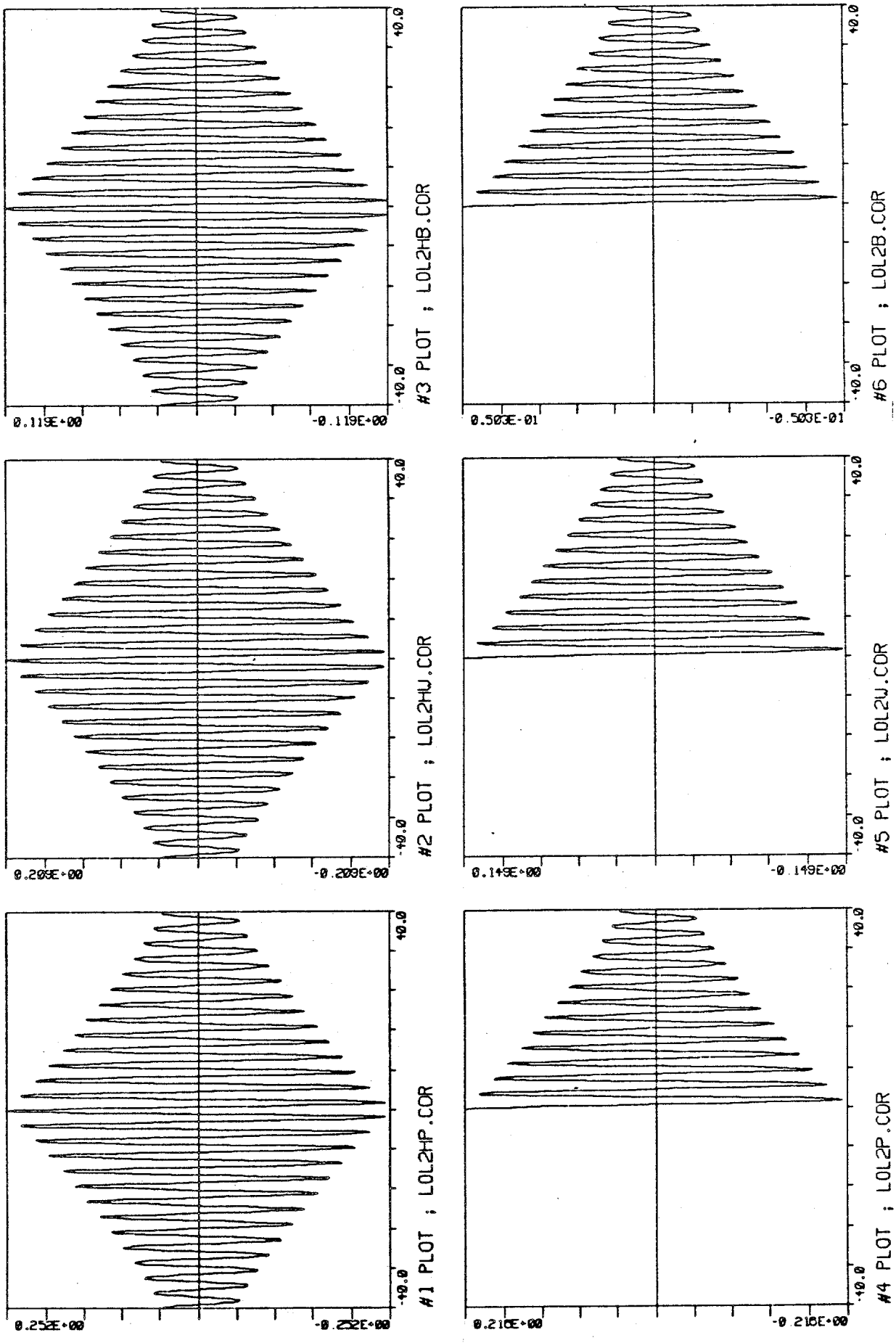

Figure #9: cross-correlation & autocorrelation functions between H and each of P,W,and B decks; unit of time=sec data from files 'L0L2*.COR' ; sampling frequency=6.4Hz total number of lags=256

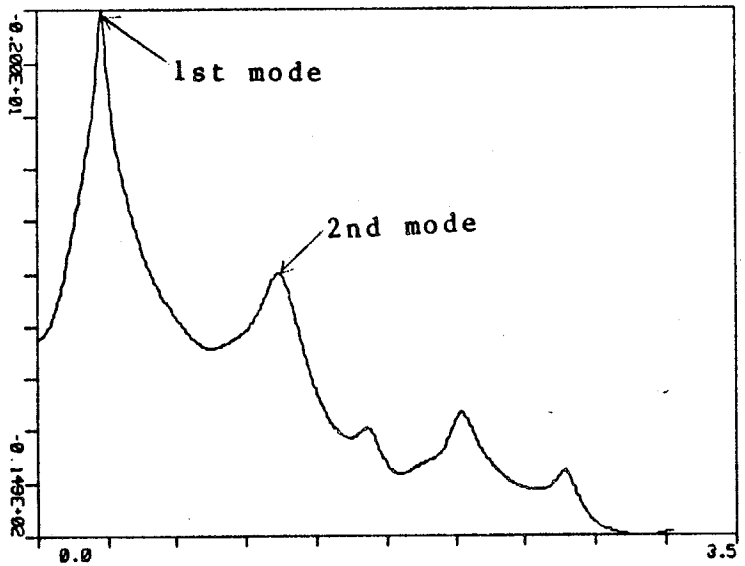

#1 PLOT ; NAH LOG MAGNITUDE

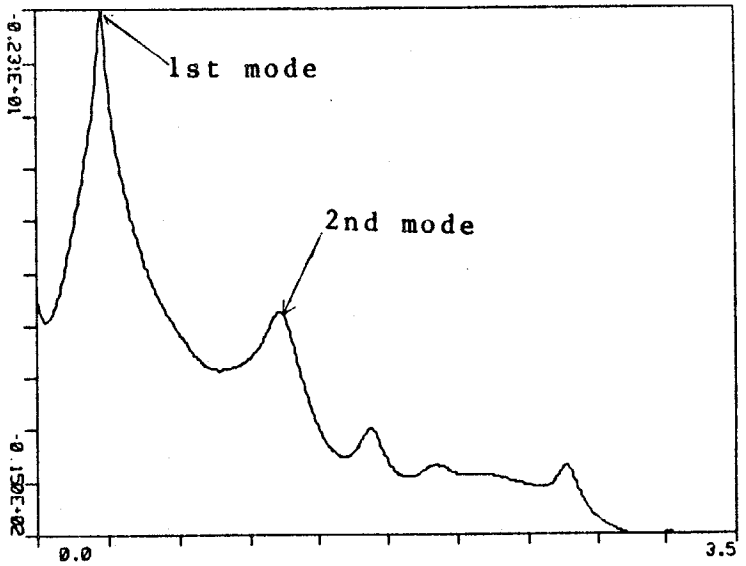

#2 PLOT ; NAP LOG MAGNITUDE

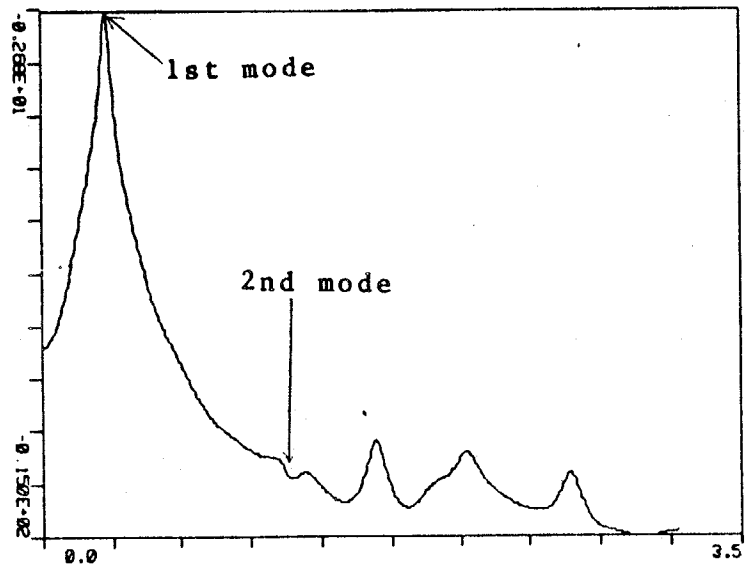

#3 PLOT ; NAW LOG MAGNITUDE

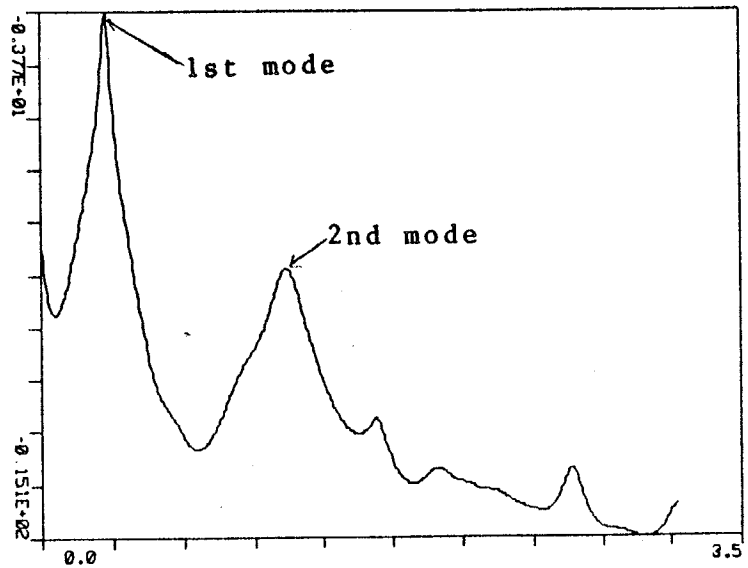

#4 PLOT ; NAB LOG MAGNITUDE

Figure #10: autospectra for the four decks estimated using the two-channel-one-dimensional formula (EQ 12); These two -channels are (H and P) (H and W) (H and B)
Only one plot for NAH because they look almost the same.

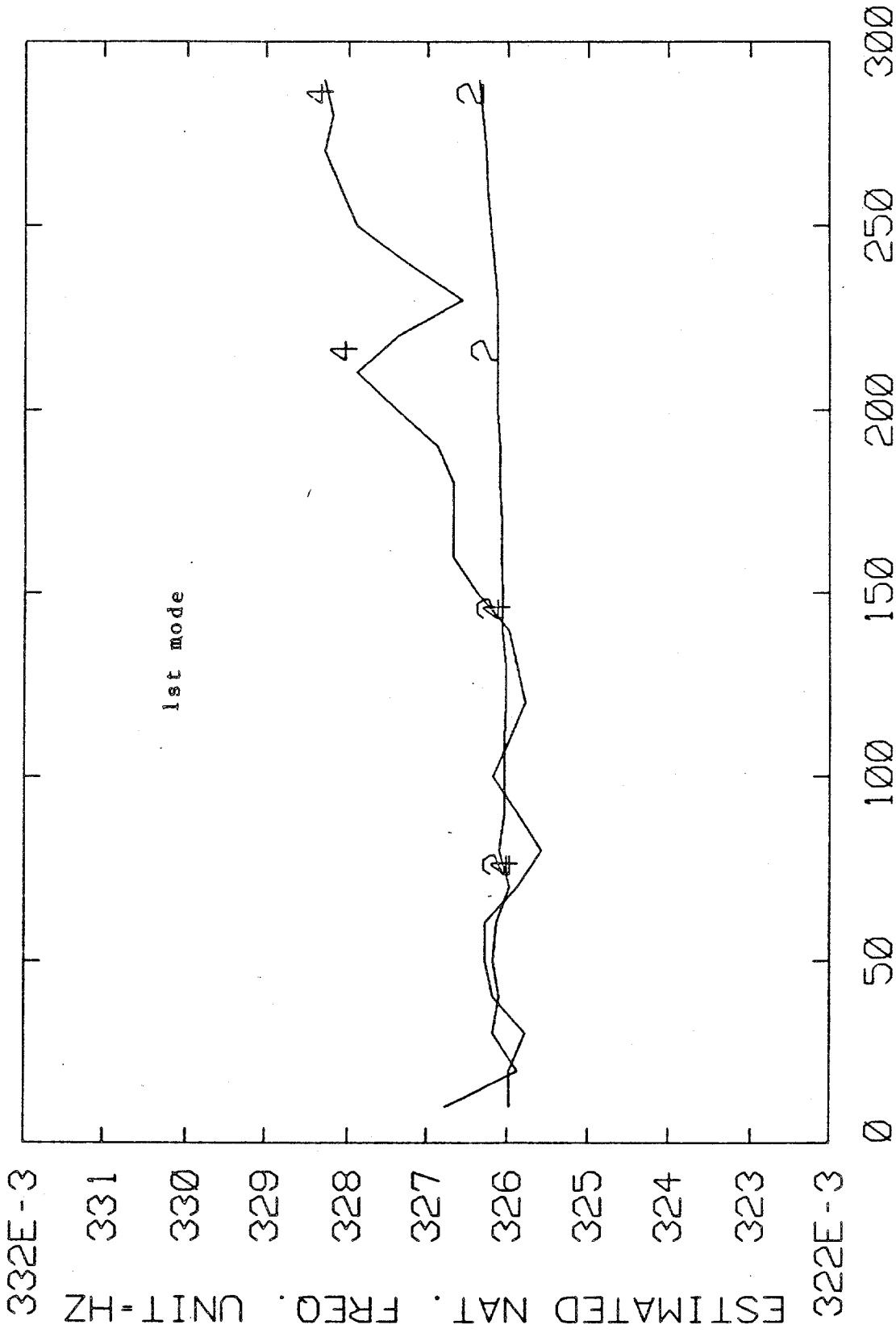

Figure #11: estimated natural frequency
Line#2 by MLM,#4 by MEM;horizontal axis units=lag

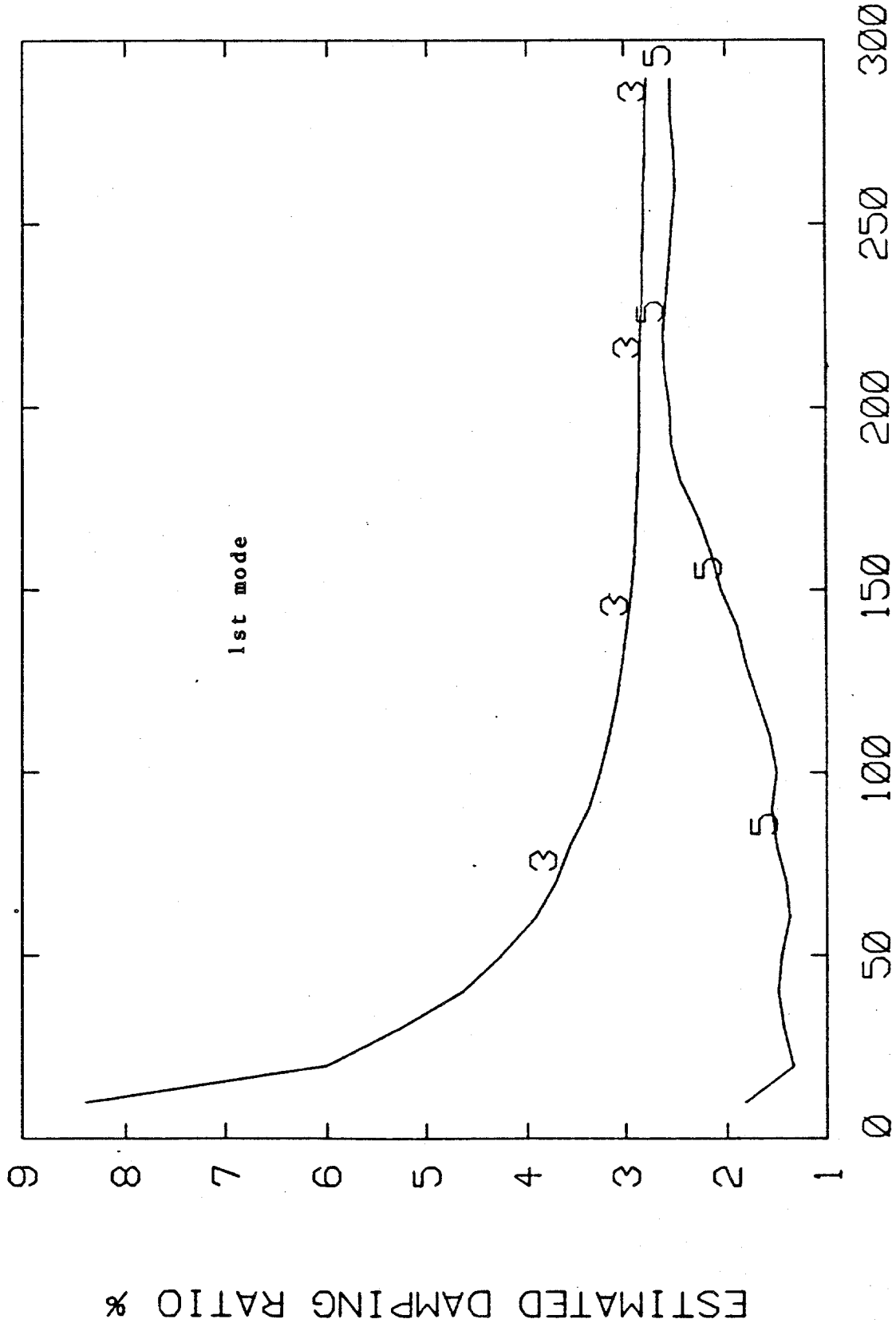

Figure #12: estmated damping ratio(%)
Line#3 by MLM,#5 by MEM;horizontal axis units=lags

#12 show the estimated natural frequency and damping ratio obtained by MLM and MEM for the first mode as a function of lags. The NAH's autocorrelation function is used in these two figures. The half-power bandwidth is used in approximating the damping ratio, see [3]. The figure shows that the damping ratio estimated by MLM looks higher than that from MEM, and the estimated natural frequency by MLM has less variation than that by MEM. Figure #13 shows the estimated cross spectra between NAH and the other records estimated by (EQ 12) using 40 lags of the correlation functions. Only the natural log (ln) of the magnitudes of the cross spectra are shown in this figure. The estimated first and second mode shapes, obtained by using the ratios of these cross spectra at the frequencies 0.32 Hz and 1.2 Hz, are plotted in figure #14. For comparison purposes, results using MEM at 80 lags as given on page 151 in [1] are also plotted in this figure.

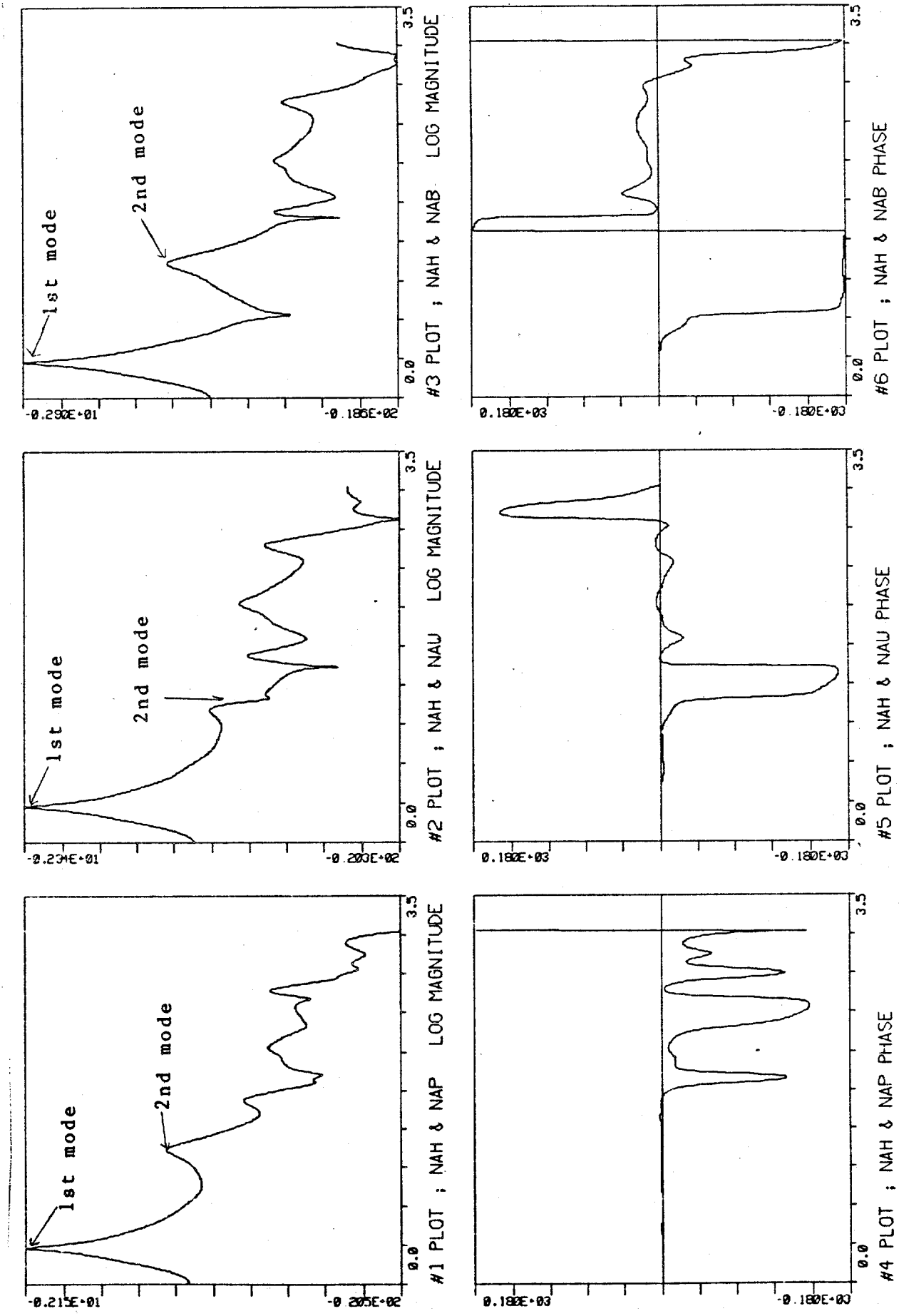

Figure #13: cross-spectra between H and each of P,W, and B using the estimator (EQ 12) and 40 lags of the correlation functions; horizontal axis units=Hz vertical axis units=degree for phase

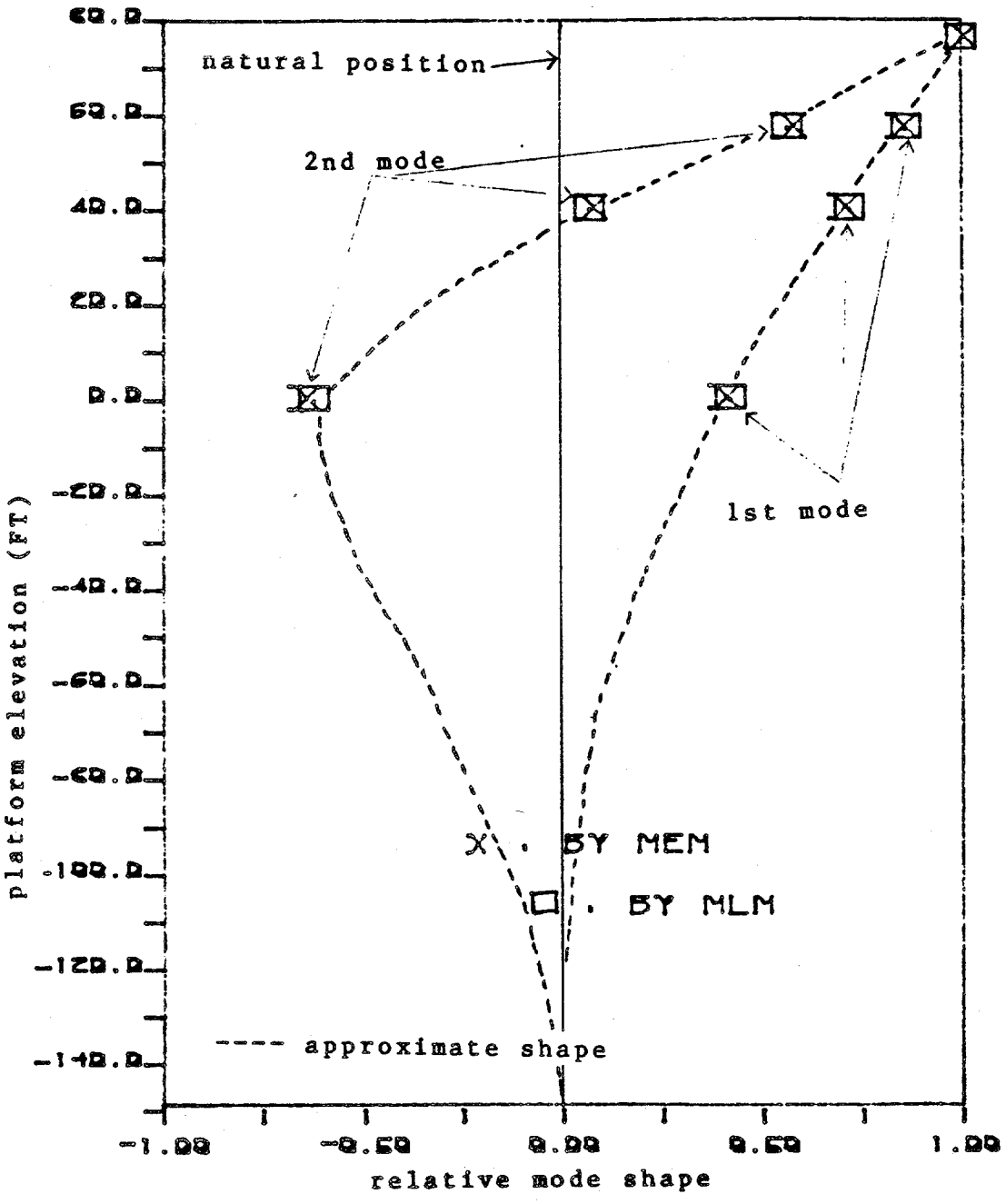

Figure #14: comparison of calculated mode shapes at each elevation(deck)

Section #3: Wavenumber Spectrum Estimation

Using (EQ 12) to estimate the one-channel multidimensional case has been discussed in [10]. We will show several examples using the sinusoidal indicator, which is detailed at the end of chapter 2. Three simulated examples using this indicator are plotted in figures #15 to #17. Only the positive wavenumbers are plotted. Figure #15 shows the estimated spectrum for the 2-D correlation function, $\{r(n,m) = \delta(n)\delta(m) + 2.0\cos(0.2\pi n+0.2\pi m) + 2.0\cos(0.4\pi n+0.64\pi m);\ -2\leq n,m\leq 2\}$ This r(n,m) has a 5x5 coarray, or $-2\leq n,m\leq 2$, and a 3x3 filter support (see fig.4 page 172 in [10] for explanation and comparison). Figure #16 shows the estimated spectrum for the correlation function, $\{r(n,m)= 0.25\delta(n)\delta(m) + \cos(0.4\pi n+0.4\pi m) + \cos(0.6\pi n+0.6\pi m)\ ;-3\leq n,m\leq 3\}$. This is the same coarray as that used in figure 2, page 853 [11]. Figure #17 shows the estimated spectrum for the correlation function, $\{r(n,m)= 2.0\delta(n)\delta(m) + 2.0\cos(0.6666\pi n+0.4\pi m) + \cos(0.2\pi n+0.44\pi m)\ ;-2\leq n,m\leq 2\}$. This is the same coarray as that used in figure 7 TABLE IV [12]. Figures 4(a) from [10], 2(b) from [11] and figure 7(c) from [12] are included in figures #18 and #19 for quick comparison. They are obtained by the modified MLM [10], IMLM [11], and MEM [12]. Figures #15 to 17 show that the sinusoidal indicator can easily distinguish the 2-D sinusoidal signals as good as the modified MLM, IMLM, and MEM.

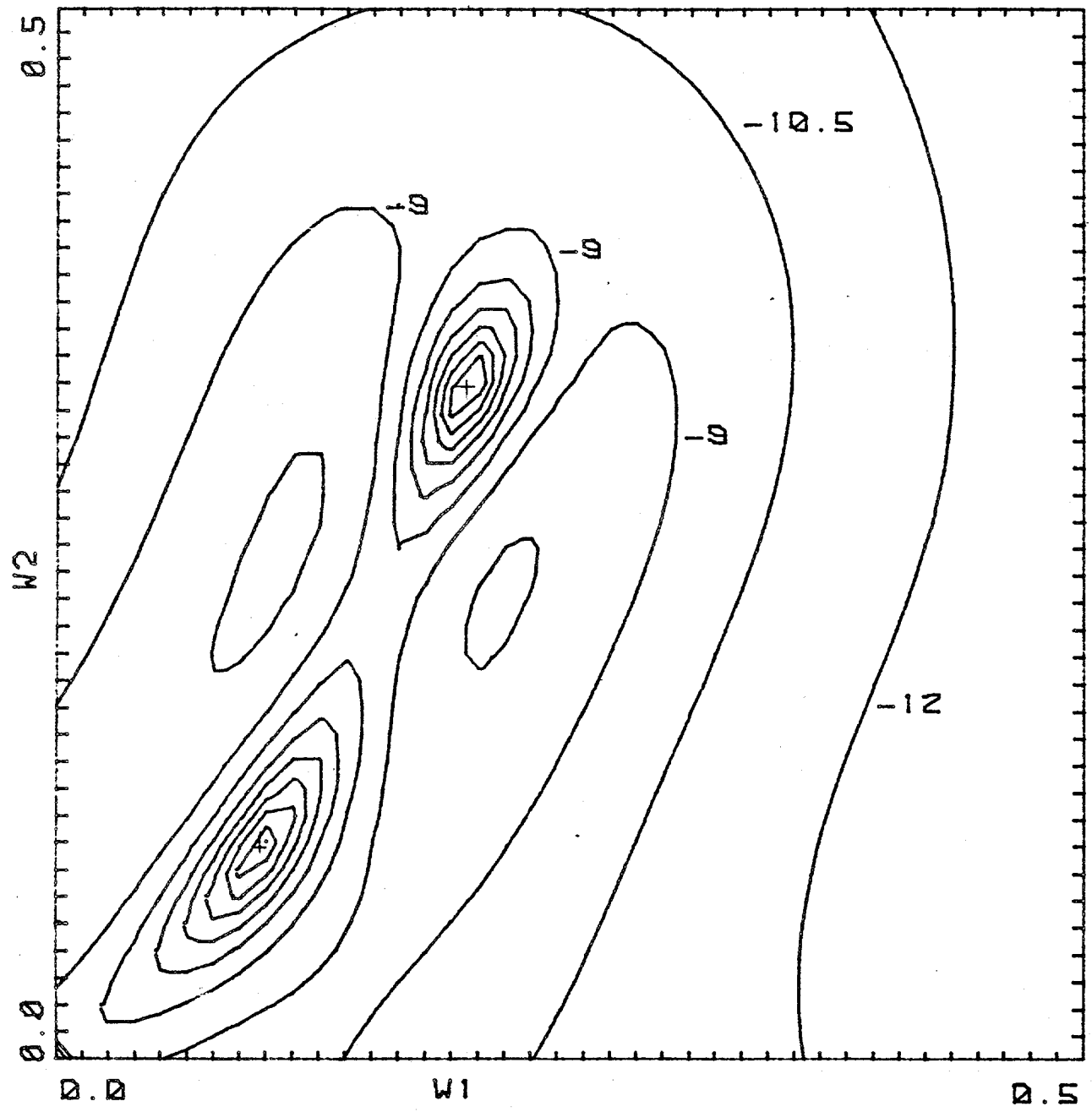

Figure #15: spectral estimates for the case of two sinusoids in noise The spatial correlaton function is $\{r(n,m)= \delta(n)\delta(m)+ 2\cos(0.2\pi n+0.2\pi m) + \cos(0.4\pi n +0.64\pi m); -2 \leq n,m \leq 2$ or 5x5 coarray$\}$. The symbol "+" represents the locations of true sinusoidal signals. The contour levels shown are in units of dB relative to the largest peak value.

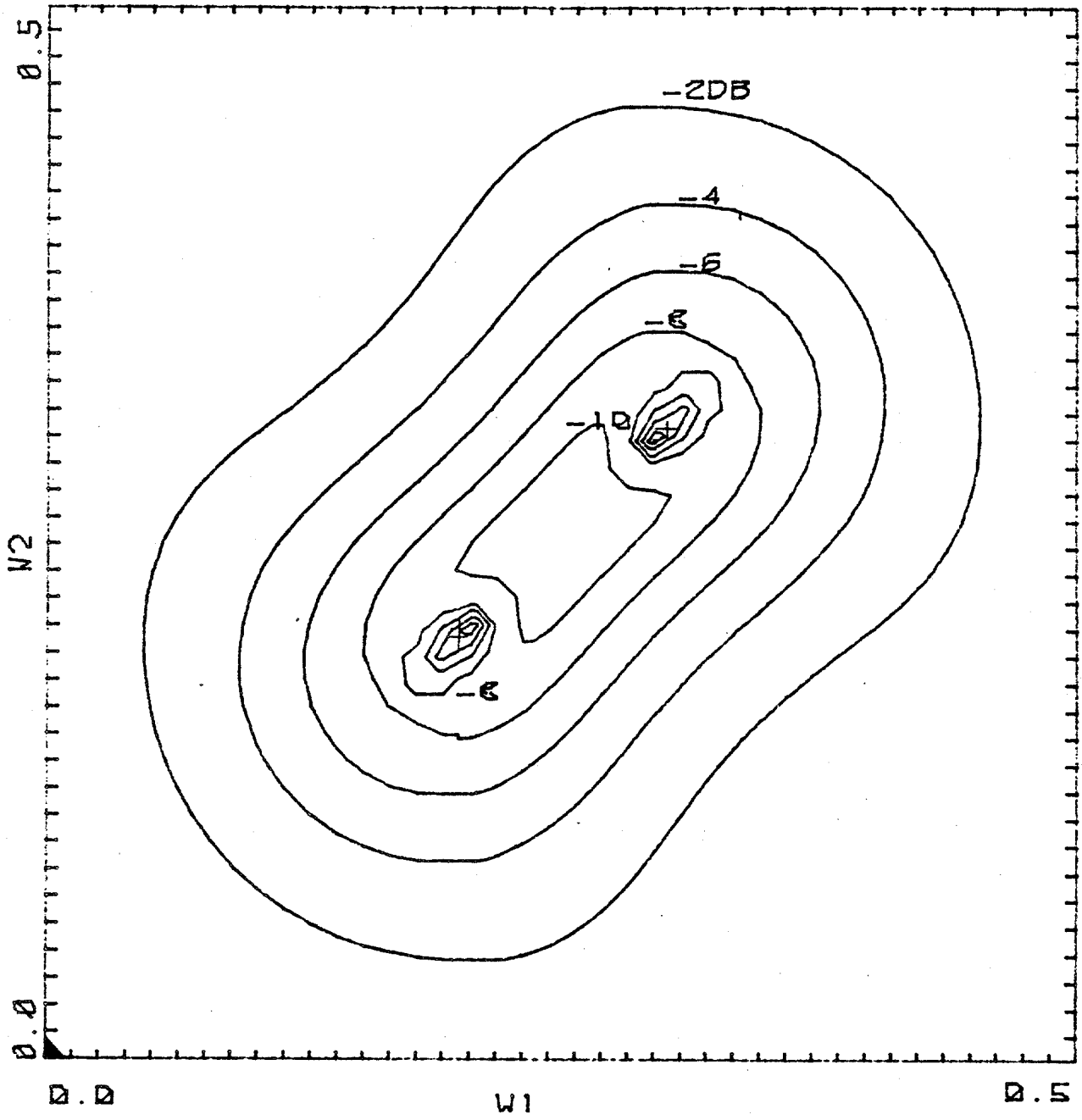

Figure #16: spectral estimates for the case of two sinusoids in noise The spatial correlaton function is $\{r(n,m)=0.25\delta(n)\delta(m)+\cos(0.4\pi n+0.4\pi m)+\cos(0.6\pi n+0.6\pi m);-3\leq n,m\leq 3$ or 7x7 coarray$\}$. The symbol "+" represents the locations of true sinusoidal signals. The contour levels shown are in units of dB relative to the largest peak value.

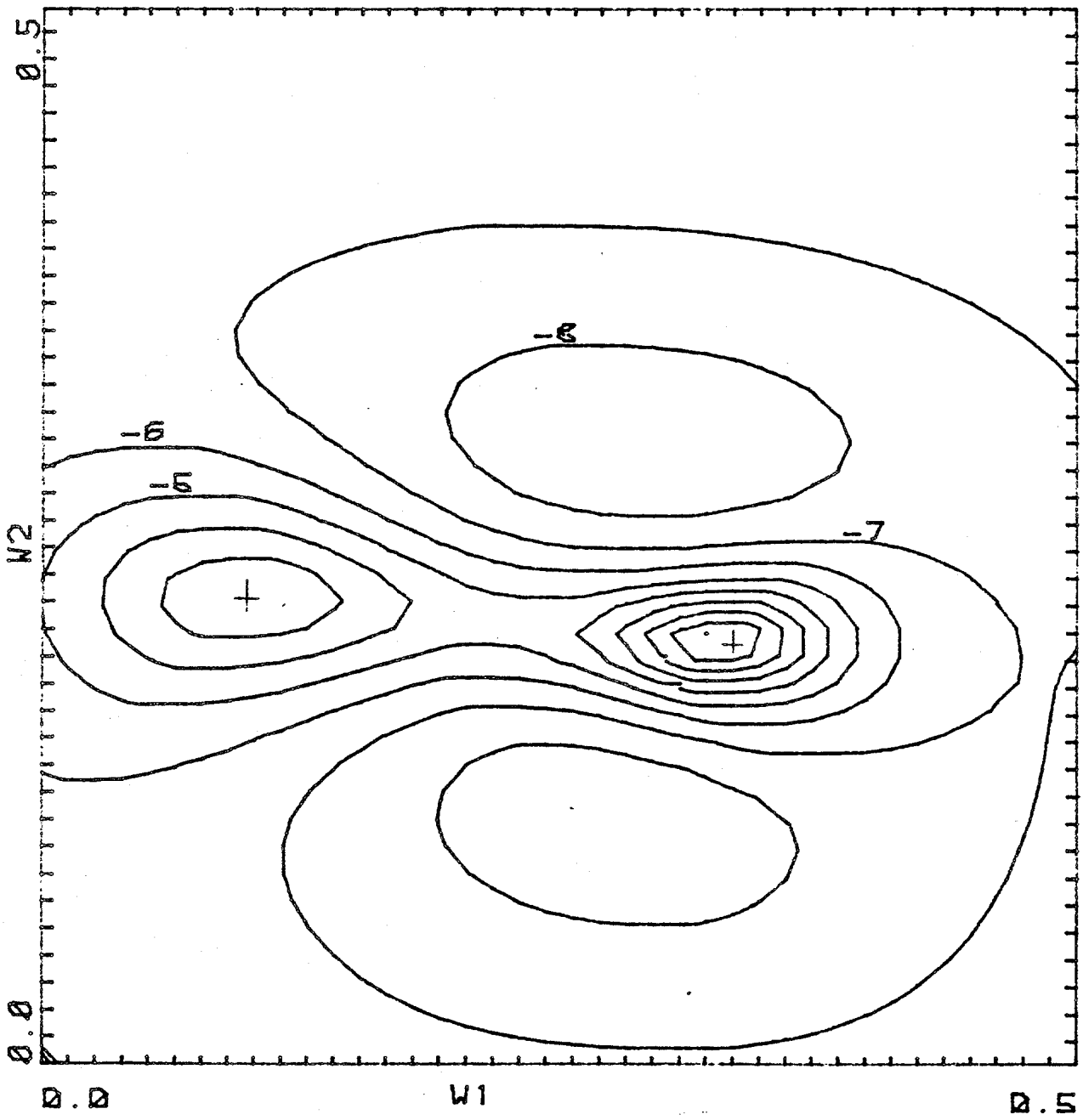

Figure #17: spectral estimates for the case of two sinusoids in noise The spatial correlaton function is {r(n,m)=2δ(n)δ(m)+2cos(0.6666πn+0.4πm)+cos(0.2πn +0.44πm);$-2\leq n,m\leq 2$ or 5x5 coarray}. The symbol "+" represents the locations of true sinusoidal signals. The contour levels shown are in units of dB relative to the largest peak value.

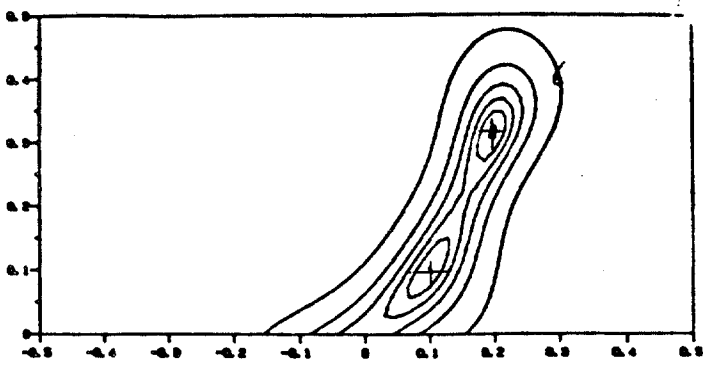

Fig. 4(a) in [10]: MLM modified.
data correlation support 5x5
two sinusoidal (3 dB each) at (0.1,0.1) and (0.2,0.32)
contour from 1.5 to 9, contour interval of 1.5 dB

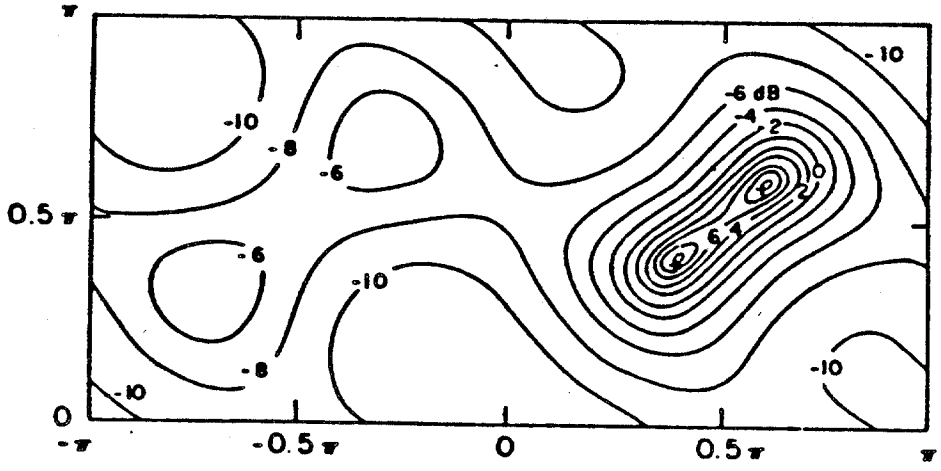

Fig. 2(b) in [11]: IMLM estimate
spectral estimate for the case of two sinusoids in noise
The contours are 2 dB apart.

Figure #18: spectra from [10] and [11]

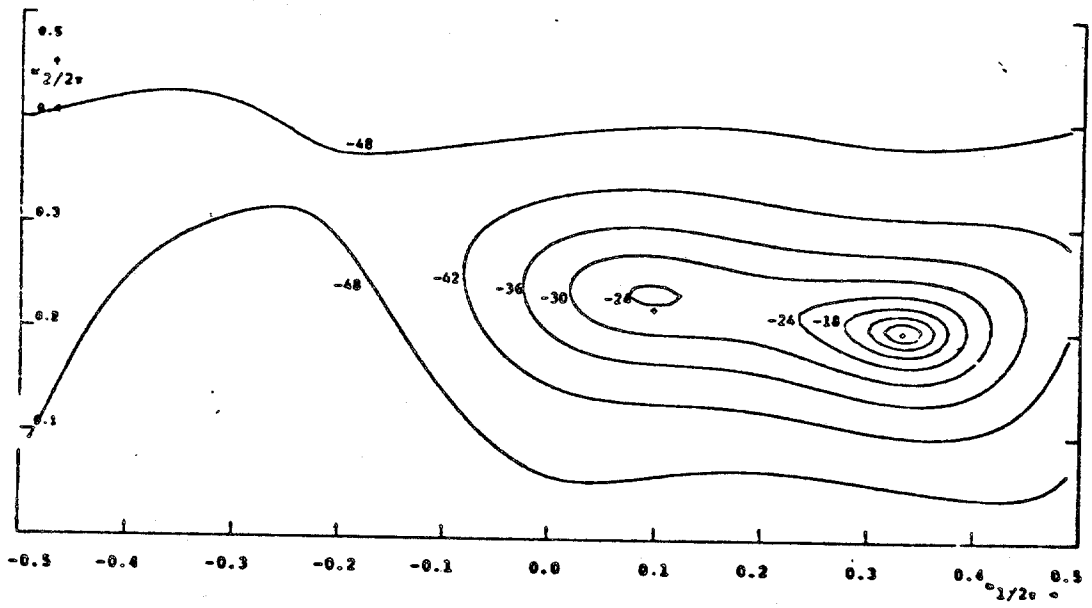

Fig. 7(c) in [12]: MEM estimate

Figure #19: spectrum from [12]

CHAPTER 4

CONCLUSION

In this work we apply two cross-entropy-like principles to estimate the power spectrum through designing a set of filters and knowing the finite sampled correlation function. Some of the present results are close to the MLM and classical windowing methods but give new interpretations to them. We also include two applications in chapter 3 with the emphasis on the cross spectral estimator. Several additional important features peculiar to the present approach are summarzed here.

First, the sensitivity of the estimated spectrum can be obtained roughly by differentiating the variances in (EQ 9,11) with respect to Rx. They are:

$$\text{MCE:}\ \frac{\partial [Ry^{-1}]ii}{\partial Rx} = -\{\, Rx^{-1}\, \underline{t}i'\, \underline{t}i\, Rx^{-1}\,\}'$$

which depends on Rx, and

$$\text{KDF:}\ \frac{\partial [Ry]ii}{\partial Rx} = tr(ti'\ ti)$$

which does not depend on Rx.

Unless we use a data adaptive filter, the sensitivity of the estimator which the KDF method gives usually has no response to the data Rx. Therefore, the KDF is usefull when one has no knowledge about Rx.

Second, note that using the data adaptive MLM filter (equation (12) from [9]) in (EQ 11) makes the equation identical to MLM. When p=1, (EQ 9) by MCE is identical to (EQ 11) by KDF.

Third, we have shown some empirical results using the estimator (EQ 12) and the indicator which always give convenient estimated spectra. More work is necessary for finding other good estimators which can be reached by this approach.

Fourth, in section 2.2, note that we build a matrix T which has NxN variables for a single channel, one dimensional signal, {x(n),n=1,N}. This contrasts with the usual situation, where we build a discrete finite length filter with N variables which processes x(n). We attempted to take advantage of these NxN-N extra variables to obtain an accurate estimated spectrum, but the results always come out to be identical to MLM. The following example is one of those that have been tried. Let $\underline{x}'=[x(1),x(2),\ldots,x(N)]$. We want to find a T which has a minimum tr(TRT′) subject to the constraint $\underline{e}'T'T\underline{e}=1$, where $\underline{e}$ is identical to that used in the special case #2 of Chapter 2, $R=E\{\underline{x}\underline{x}'\}$, and the rows of T are N filters. The constraint means that the sum of the energies from the output of these N filters is unbiased (although not phase unbiased) for a sinusoidal signal with frequency w. We hope that minimizing tr(TRT′) will reduce

the influence from other frequency bands. The solution is still MLM. Note that T′T is a non-negative definite matrix and tr(TRT′)=tr(RT′T).

Fifth, the general theory (EQ 1 to 4) can be used in other subjects [14].

APPENDIX

A Technical Approach for Improving The Resolution Ability

In this appendix we will derive a family of spectral estimators which are obtained by weighting the magnitude of the spectrum. The MEM and square window method are included in this technical approach. The criterion is maximizing

$H = \int_{-B}^{B} F[S(f)]df$, where the weight on the magnitude of S(f) is F[S]=logS and the constraints are $R(m) = \int_{-B}^{B} S(f)e^{j2\pi fmT} df$, $|m| \leq M$. This suggests examining the possible functions F. The following simple example is a test of this idea. x(t) is assumed to be zero mean, stationary and band limited random process. H is defined to be an integral function.

$$H = \int_{-B}^{B} F[S(f)]df$$

f: frequency

B: frequency band of x(t)

F: arbitrary function of S

S: spectrum of x(t)

$R(t)=E[x(y)x(y+t)]$

$R(t)$: autocorrelation function of $x(t)$

$R(t_m)$ known for $-M \leq m \leq M$; m : integer

($R(t_m)$ is sampled at time t_m)

The sampling time interval T is small enough

for $1/2T = B$, B: bandwidth.

$t_{m+1} = t_m + T$

We estimate $S(f)$ by giving $R(m)=R(t_m)$ for $-M \leq m \leq M$.

The true spectrum $S(f)$ should be

$$S(f)= \sum_{m=-inf}^{inf} R(m)\, e^{-j2pifmT} \quad T \ .$$

Since M is finite, we need a creterion for choosing

the $R(m)$ for $|m| > M$.

Such a creterion is H. This means that the H function is

maximized or minimized by choosing $R(m)$ for $|m| > M$.

Thus for $|m| > M$,

$$\frac{\partial H}{\partial R(m)} = 0 \ .$$

It remains to choose a proper function F.

For simplicity assume $F(S)= S^n$. Then

$$H= \int_{-B}^{B} S(f)^n \, df, \text{ and so}$$

$$\frac{\partial H}{\partial R(m)} = \frac{\partial}{\partial R(m)} \int_{-B}^{B} df \left\{ \sum_{m'=-\inf}^{\inf} R(m') e^{-j2\pi f m' T} T \right\}^n$$

$$= \int_{-B}^{B} df \, n \left\{ \sum_{m'=-\inf}^{\inf} R(m') e^{-j2\pi f m' T} T \right\}^{n-1} e^{-j2\pi f m T} T$$

Since $\frac{\partial H}{\partial R(m)} = 0$ for $|m| > M$, we have

$$\int_{-B}^{B} df \{ So(f) \}^{n-1} e^{-j2\pi f m T} T = 0 \quad ;\text{where } So(f) = nS(f)$$

This implies that So(f) is expressible in the form of a truncated Fourier series as follows:

$$So(f) = \sum_{m'=-M}^{M} C(m') e^{-j2\pi m' f T}$$

where $C(m) = C^*(-m)$ in order to insure that So(f) is a real quantity.

The next step in the derivation is to determine values for the set of coefficients { C(m') } such that the spectral density estimator S(f) is consistent with the known values of the autocorrelation function, that is,

$$R(m) = \int_{-B}^{B} df \, S(f) e^{j2\pi m f T} \quad \text{for } |m| \leq M$$

$$= \int \left\{ \frac{So}{n} \right\}^{\frac{1}{n-1}} e^{j2\pi m f T} df$$

$$= \int e^{j2\pi fmT} \left\{ \frac{1}{n} \sum_{m'=-M}^{M} C(m')\, e^{-j2\pi fm'T} \right\}^{\frac{1}{n-1}} df$$

Let $z = e^{j2\pi fT}$. Then

$$\Rightarrow \quad R(m) = \frac{B}{j\pi} \oint z^{m-1} \left\{ \sum_{m'=-M}^{M} C(m')\, z^{-m'} \frac{1}{n} \right\}^{\frac{1}{n-1}} dz \quad ; \ |m| \leq M$$

When n=2

$$R(m) = \frac{B}{j\pi} \oint z^{m-1} \left\{ \sum_{m'=-M}^{M} C(m')\, z^{-m'} \right\} (0.5)\, dz \quad ; \quad |m| \leq M$$

$$= \frac{0.5B}{j\pi} \int_{-B}^{B} \left\{ \sum_{m'=-M}^{M} C(m')\, z^{-m'+m-1} \right\} dz$$

$$= B\, C(m) \ ;$$ Beause only 1 simple pole appears.

This means that the spectral estimator by the square window method is an optimal solution for $H = \int_{-B}^{B} S^2 \, df$.

Since $C(-n) = C^{*}(n)$, So(f) may be expressed as

$$\sum_{m=-M}^{M} C(m)\, z^{-m} = G(z)\, G^{*}\left(\frac{1}{z^{*}} \right), \text{ where}$$

$$G(z) = \sum_{n=0}^{M} g_n\, z^{-n}$$

G(z) is chosen to be minimum phase, and

$$G^{*}\left(\frac{1}{z^{*}}\right) = \sum_{n=0}^{M} g_n^{*} z^{n}$$

$G^{*}\left(\frac{1}{z^{*}}\right)$ is choosen to be maximum phase.

Substitute this in R(m).

$$R(m) = \frac{B}{jpi} \oint \left\{ \frac{1}{n} G(z)\, G^{*}\left(\frac{1}{z^{*}}\right) \right\} z^{n-1}\, z^{m-1}\, dz \quad ; \quad |m| \leq M$$

The above M+1 nonlinear equations can be used to solve the $\{g_n, n=0 \text{ to } M\}$ M+1 unknowns by numerical methods.

When $F[S(f)] = \log S(f)$, the solution is that of MEM.

REFFERENCES

1. Briggs, Michael Jeffrey, "Multichannel Maximum Entropy Method of Spectral Analysis applied to Offshore Structures," WHOI/MIT Dissertation, August 1981

2. Burg, J. P., "Maximum Entropy Spectral Analysis," Ph.D. Thesis, Stanford University, May, 1975

3. Cook, Michael Ferris, "Damping Estimation, Response Prediction and Fatigue Calculation of an Operational Single Pile Platform," WHOI/MIT Dissertation, May 1982

4. Eberhard, A., "An Optimal Discrete Window for the Calculation of Power Spectra," IEEE vol. AU-21, no. 1, February 1973

5. Haykin, S., "Nonlinear Methods of Spectral Analysis," Topics in Applied Physics, vol. 34, Springer-Verlag

6. Duckworth, Gregory Lynn,"Processing and Inversion of Arctic Ocean Refraction Data," Ph.D Thesis, M.I.T., Sep. 1983

7. Kay, Steven M. and Marple, Stanley Lawrence, Jr., "Spectrum Analysis-A Morden Perspective," Proceedings of the IEEE, vol. 69 no. 11, Nov. 1981

8. Kullback, S., "Information Theory and Statistics," New York: John Wiley & Sons, 1959

9. Lacoss, R. T., "Data Adaptive Spectral Analysis Methods," Geophysics, vol. 36, no. 4, pp. 661-675, August, 1971

10. Lagunas-Hernandez, Miguel A. and Gasull-Llampallas, Antoni, "An Improved Maximum Likelihood Method for Power Spectral Density Estimation," IEEE Transactions On Acoustics, Speech, And Signal Processing, vol. ASSP-32, no. 1, February, 1984

11. Lim, Jae S. and Dowla, Farid U., "Improved Maximum Likelhood Method for Two-Dimensional Spectral Estimation," ICASSP, IEEE, Boston, 1983

12. Lim, J. S. and Malik, N., "A New Algorithm for Two-dimensional Maxmum Entropy Spectrum Power Spectrum Estimation," IEEE Trans. on Acoust., Sp. & Sig. Proc., vol. ASSP-29, pp.410-413, June 1981

13. Marzetta, Thomas L., "A New Interpretation for Capon's

Maximum Likelihood Method of Frequency-Wavenumber Spectral Estimation," IEEE Transactions on Acoustics, Speech, and Signal Processing, vol. ASSP-31, no. 2, pp. 445-449, April, 1983

14. Musicus, Bruce R., "Iterative Algorithms for Optimal Signal Resconstruction and Parameter Identification Given Noisy and Incomplete Data," Ph.D. Thesis, Department of E.E., M.I.T., 1982

15. Papoulis, Athanasios, "Probability, Random Variables, and Stochastic Processes," second edition, McGraw-Hill, Inc., 1984

16. Shore, John e., "Axiomatic Derivation of the Principle of Maximum Entropy and the Principle of Minimum Cross-Entropy," IEEE Transactions on Information Theory, vol. IT-26, no. 1, pp. 26-37, January, 1980

17. Shore, John E, "Minimum Cross-Entropy Spectral Analysis," IEEE Transactions on Acoustics, Speech, and Signal Processing, vol. ASSP-29, no. 2, pp. 230-236, April, 1981

OTC 5006

The Prediction of Lockin Vibration on Flexible Cylinders in a Sheared Flow

by J.K. Vandiver, *Massachusetts Inst. of Technology*

Abstract

A method is proposed for the prediction of the flow induced vibration response of flexible cylinders such as cables, pipes, and risers, in a sheared flow. The significance of material and hydrodynamic sources of damping is discussed. The reduced damping or response parameter plays a key role in response prediction. However, the dependence of the response parameter and therefore the response amplitude on the ratio of cylinder mass per unit length to the displaced fluid mass per unit length is shown to be widely misunderstood. Under lockin conditions, damping is important in determining response amplitude, but cylinder mass per unit length is not.

Introduction

Flexible cylinders, such as cables, drill pipe, and marine risers, often exhibit an harmonic flow induced vibration response known as lockin. Under uniform flow conditions, lockin has been extensively studied and empirical response prediction techniques are often adequate. However, real ocean applications often require response prediction under non-uniform (sheared) flow conditions. Very long cylinders with closely spaced natural frequencies rarely exhibit lockin behavior and frequently behave as infinite strings (1). For shorter cylinders, with well separated natural frequencies, lockin with one mode is possible, even in the presence of shear. However, in such cases, response amplitude is very difficult to predict and it is often difficult to determine which mode, if any, will dominate the response. In this paper, a method for predicting lockin in a sheared flow is proposed. The method makes extensive use of the concept of the response parameter or reduced damping, as it is sometimes called.

A very common misconception regarding the response parameter is pointed out. The response parameter is shown to be primarily a function of damping and is specifically not a function of the cylinder mass per unit length.

References and figures at end of paper.

Normal Mode Model of Lockin Vibrations

A pipe or cable under tension has, from an analytical view, an infinity of natural modes. When the cylinder is deployed with its longitudinal axis normal to an incident uniform flow, vibration is caused by the shedding of vortices in the wake of the cylinder. The vortex shedding process generates both fluctuating lift and drag forces on the cylinder. Under the correct circumstances, described extensively in the literature, (2,3) a phenomena known as lockin may occur. Lockin is characterized by the synchronization of the wake with either the cross-flow (lift direction) oscillations or with the in-line (drag direction) vibrations. This paper focuses on cross-flow lockin only, in which one cross flow mode dominates the response. At lockin in a uniform flow the lift forces are coherent over the entire length of the cylinder. A normal mode solution to the partial differential equation of motion may be obtained, and is briefly reviewed below.

Consider a beam or string under tension with fixed ends as defined in Figure 1. Let the vortex-induced cross-flow displacement be given by

$$y(x,t) = \sum_i q_i(t)\Psi_i(x) \qquad (1)$$

where the $\Psi_i(x)$ are the mode shapes and the $q_i(t)$ are the modal amplitudes. Using the method of normal mode superposition, and assuming insignificant damping related intermodal coupling, a set of independent equations of motion are obtained, one for each mode. These equations are of the form:

$$M_i\ddot{q}_i + R_i\dot{q}_i + K_iq_i = N_i(t) \qquad (2)$$

This equation is simply that of a linear, single degree of freedom mass-spring-dashpot system excited by a force $N_i(t)$, known as the modal exciting force for mode i. There exists one such

For cylinders that do not have a constant mass per unit length, the m in these equations is replaced with an equivalent uniform mass per unit length m_e. m_e is the equivalent constant mass per unit length which would yield the same modal mass from Equation 4 as the actual variable mass per unit length m(x). Therefore

$$m_e = \frac{\int_0^L m(x)\Psi_i^2(x)\,dx}{\int_0^L \Psi_i^2(x)\,dx} \tag{20}$$

For the remainder of this paper, a constant mass per unit length m shall be assumed, to simplify the analysis.

D is the cylinder diameter, assumed constant, and S_t is the Strouhal number given by

$$S_t = \frac{f_s D}{U} \tag{21}$$

where f_s is the vortex shedding frequency and U is the free stream fluid velocity. At lockin the natural frequency and the vortex shedding frequency are assumed to be equal.

$$2\pi f_s = \omega_s = \omega_i = 2\pi S_t U/D \tag{22}$$

Over many years the variety of these evolved forms has led to confusion and misinterpretation of the significance of the various terms which form the response parameter S_G.

The most serious misinterpretation is the implication that lockin response amplitude depends on the mass ratio, μ. It has been generally believed that very dense cylinders respond with lower amplitudes than low density ones. This is not true. It is in fact dependent on fluid exciting forces and structural damping (not damping ratio). The mass per unit length of the cylinder is only important in determining the natural frequency. The validity of these statements can be demonstrated by simply drawing upon definitions, as shown below.

From Equations 18 and 6

$$k_s = \frac{4\pi m_e \zeta_s}{\rho D^2} = \frac{4\pi m_e R_i}{\rho D^2\, 2\omega_1 M_i} \tag{23}$$

Using the definitions of modal mass, and effective mass per unit length from Equations 4 and 20 yields,

$$k_s = \frac{2\pi R_i}{\rho D^2 \omega_i \int_0^L \Psi_i^2(x)\,dx} \tag{24}$$

For the case of constant damping constant per unit length, r(x)=r

$$k_s = \frac{2\pi r}{\rho D^2 \omega_i} \tag{25}$$

If k_s is not a function of m(x) then from Equation 15 neither is S_G.

$$S_G = 2\pi S_t^2 k_s \tag{15}$$

$$S_G = \frac{4\pi^2 S_t^2 R_i}{\rho D^2 \omega_i \int_0^L \Psi_i^2(x)\,dx} \tag{26}$$

R_i is the equivalent, linear, structural modal damping. The actual source of damping may not in fact be linear. For most interesting vibration cases the damping is low and for any specific steady state response amplitude an equivalent linear damping is an acceptable approximation.

There is experimental confirmation that S_G and hence the predicted response do not depend specifically on the mass ratio but on the ratio ζ_s/μ. As shown, this is because in taking this ratio the dependence on mass per unit length cancels out. Griffin in reference (7) presents a plot of response amplitude, $2\bar{Y}/D$, versus reduced velocity $V_r=U/f_n D$ where f_n is the natural frequency. This figure is reproduced in figure 4.

Two different cases are shown, one in air and one in water. For both the ratio ζ_s/μ is approximately constant. However, the damping ratios and therefore the mass ratios are different by an order of magnitude. Bothelo has also observed this apparent lack of specific dependence on μ (8).

Both Griffin and Botelho have pointed out another interesting fact, which can be seen in Figure 4. The in water case has a larger damping ratio, by a factor of 10, and therefore it has a much broader bandwidth, than the in air case with lower damping. The halfpower bandwidth for a linear oscillator is equal to $2\zeta_i\omega_i$. Thus one would expect to see a wider region of large amplitude response in a figure such as 4, for those cylinders with larger damping ratios. This author is of the opinion that the consequence of a higher damping ratio is to make lockin vibration of the cylinder less sensitive to local variations in flow velocity (hence reduced velocity) and therefore more tolerant of shear. In other words, two geometrically similar cables with the same reduced damping but different damping ratios will respond differently to a shear. The one with the higher damping ratio will likely experience lockin over a greater portion of its length.

For most engineers S_G has little physical meaning. In the next section, an attempt is made to clarify it.

An Interpretation of S_G, The Response Parameter

No one denies its importance but a common sense interpretation is needed for S_G. To develop one requires a statement of the equation of motion for the normal mode excited at resonance during lockin. At lockin the lift force per unit length in phase with the cross-flow velocity of the cylinder can be expressed as

$$f(x,t) = 1/2\ \rho U^2 D C_L(x)_e^{i\omega_i t} \tag{27}$$

where

$$I_i = \frac{\int_0^L \Psi_i^4(x)\,dx}{\int_0^L \Psi_i^2(x)\,dx} \qquad (39)$$

For example, a string or a beam with pinned ends and constant tension have mode shapes which are given by

$$\Psi_i(x) = \sin\left(\frac{i\pi x}{L}\right) \qquad (40)$$

and $I_i = 3/4 \qquad (41)$

Other values for I_i corresponding to different mode shapes are given in Reference 4, as is a table identifying the source of the data used in Figure 2.

The factor $I_i^{1/2}/\psi_{imax}$ was used in an attempt to reduce the scatter in plotting response data for many different types of structures versus S_G. That this was the appropriate factor to use to accomodate various mode shapes was based on the assumption that the wake oscillator model correctly predicts response. Implicit in the wake oscillator model are particular assumptions regarding the spatial variation of $C_L(x)$. This author is of the opinion that such models are only approximations and that much of the scatter in the data is due to the fact that the correction factor has substantial error for some types of mode shapes.

It should also be noted that only very little of the data shown in Figure 2 is derived from cables and beams under tension such as risers and casing strings, which have essentially sinusoidal mode shapes. In the last few years a large amount of experimental data have been accumulated on such cylinders, and should be compiled in a separate plot of $2y_{max}/D$ versus S_G without correction factors such as $I^{1/2}/\Psi_{imax}$.

A Proposed Equivalent Response Parameter for Sheared Flow: S_{GE}

Under sheared flow conditions lockin may occur over a limited portion of the cylinder defined by the range X_1 to X_2. For sections of the cylinder outside of this range lockin does not occur and energy is lost due to hydrodynamic damping. In the analysis to follow it is assumed that only one mode has significant response, and even though exciting forces do exist outside of the lockin region they are not at the natural frequency and cause insignificant response. The method proposed is intended to be used to evaluate several possible vibration modes, one at a time, to determine which if any is likely to dominate the response.

A substantial database exists, which tabulates observed response versus the response parameter, S_G, but for uniform flows only. The approach proposed here takes advantage of this existing database by providing an estimate of the response parameter of an equivalent cylinder in a uniform flow, which would behave the same as the cylinder in the sheared flow. In order to be equivalent, both the cylinder in the sheared flow and the equivalent cylinder in the uniform flow must have the following characteristics.

i. The modal response amplitude for each must be the same and therefore from Equation 14

$$\frac{N_{ie}}{\omega_i R_{ie}} = \frac{N_{is}}{\omega_i R_{is}} \qquad (42)$$

where the subscripts e and s refer to the equivalent and sheared cases respectively.

ii. The exciting force over the region x_1 to x_2 must be the same for both cases. Outside of this region the forces contributing to lockin are assumed to be zero for the sheared case, and appropriate to that of a fully locked in cylinder in the equivalent case. The equivalent cylinder experiences lockin over its entire length and therefore additional power is fed into the resonant mode outside of the region x_1 to x_2. In order for the response amplitude to stay constant the modal damping in the equivalent cylinder must be increased, so as to dissipate the greater injected power.

Solving for the equivalent damping

$$R_{ie} = R_{is}\,\frac{N_{ie}}{N_{is}} \qquad (43)$$

The equivalent response parameter is obtained directly from Equation 26.

$$S_{GE} = \frac{4\pi^2 S_t^2 R_{ie}}{\rho D^2 \omega_i \int_0^L \Psi_i^2(x)\,dx} \qquad (44)$$

$$= \frac{8\pi^2 S_t^2 m_e \zeta_{ie}}{\rho D^2} \qquad (45)$$

where

$$\zeta_{ie} = \frac{R_{ie}}{2\omega_i M_i} \qquad (46)$$

and m_e is defined in Equation 20. It remains to obtain a detailed expression of R_{ie} in terms of R_{is}, and N_{ie}/N_{is}. From Equation 29 and item (ii) above,

$$N_{ie}/N_{is} = \frac{\int_0^L C_L(x)\Psi_i(x)\,dx}{\int_{X_1}^{X_2} C_L(x)\Psi_i(x)\,dx} \equiv \frac{P_u}{P_s} \qquad (47)$$

and from Equation 5

$$R_{is} = \int_0^L (r_s(x) + r_h(x))\Psi_i^2(x)\,dx \qquad (48)$$

ω_s	shedding frequency
ρ	density of water
μ	mass ratio
ϕ_i	phase angle
$\Psi_i(x)$	mode shape
Ψ_{imax}	maximum value of the mode shape

Acknowledgements

This work was sponsored by the Technology Assessment Research Program of the Minerals Management Service.

References

1. Kim, Y.H., Vandiver, J.K., Holler, R., "Vortex-Induced Vibration and Drag Coefficients of Long Cables Subjected to Sheared Flows," Proceedings of the Fourth International Offshore Mechanics and Arctic Engineering Symposium, Volume One, ASME, Dallas, Texas, Feb. 1985.

2. Griffin, O.M., Ramberg, S.E., "Some Recent Studies of Vortex Shedding with Application to Marine Tubulars and Risers," ASME J. of Energy Resources Technology, Vol. 104, March 1982.

3. Sarpkaya, T., "Vortex-Induced Oscillations, A Selective Review," J. of Applied Mechanics, Vol. 46, June 1979.

4. Griffin O.M., "OTEC Cold Water Pipe Design for Problems Caused by Vortex-Excited Oscillations," Naval Research Laboratory Memorandum Report 4157, March 14, 1980.

5. Griffin, O.M., "Vortex Shedding From Stationary and Vibrating Bluff Bodies in a Shear Flow," Naval Research Laboratory Memorandum Report 4287, August 11, 1980.

6. Stansby, P.K., "The Locking-on of Vortex Shedding Due to the Cross-Stream Vibration of Circular Cylinders in Uniform and Sheared Flows," J. of Fluid Mechanics, Vol. 74, 1976.

7. Griffin, O.M., "Vibrations and Flow-Induced Forces Caused by Vortex Shedding," Symposium on Flow-Induced Vibration, Volume 1, ASME Winter Annual Meeting, Dec. 1984.

8. Botelho, D.L.R., "An Empirical Model for Vortex-Induced Vibrations," Calif. Institute of Tech., Earthquake Engineering Research Laboratory Report No. EERL 82-02, August 1982.

THE RELATIONSHIP BETWEEN IN-LINE AND CROSS-FLOW, VORTEX-INDUCED, VIBRATION OF CYLINDERS

J. Kim Vandiver
Massachusetts Institute of Technology

Jen-Yi Jong, Wyle Laboratories

ABSTRACT

Cable strumming experiments were conducted at Castine, Maine in 1981 and from an icebreaker in 1983. The purpose was to study the vibration characteristics of long flexible cylinders subjected to vortex-induced oscillation. Particular emphasis was placed on the investigation of the relationship between in-line and cross-flow vibration. Under non-lockin, random vibration conditions, linear spectral analysis indicated that in-line and cross-flow response were linearly independent of one another, while the results of modal analysis showed that the moving average vibration energies in these two directions were strongly related. A higher order spectral analysis was performed to demonstrate a non-linear correlation between in-line and cross-flow vibration of flexible cylinders excited by vortex shedding in both uniform flow and sheared flow conditions.

The results of bispectral analysis demonstrated the existence of a quadratic relationship between in-line and cross-flow motion under both lockin and non-lockin conditions. The well-known frequency doubling phenomena in in-line response was proven to be the result of such a quadratic correlation.

INTRODUCTION

Many types of ocean-based structures such as marine risers, TLP tension members, deep water pipelines and hydrophone cables are susceptible to vortex-induced vibration. These strumming oscillations are of great practical importance because they may cause failure by fatigue.

The resolution of problems associated with prediction of vortex-induced vibration has proven to be extremely difficult due to the complex, non-linear interactions, between the structural motions and the vortex-shedding. The well-known wake capture phenomenon is a typical example of such non-linear interactions. A sampling of papers on this topic can be found in references 1 through 4.

The emphasis in the literature has been placed mostly on the study of vibration characteristics in the cross-flow direction. The behavior in the in-line direction is much less well-understood. No attempt has been made previously to investigate the relationship between cross-flow and in-line response, or equivalently, between lift and drag forces under non-lockin conditions. Even the answer to the preliminary question of whether they are correlated or independent is not available for non-lockin conditions. In the design of, for example, a marine riser, the correlation between the response in these two perpendicular directions plays an important role in fatigue life estimation, because of its relation to the stress statistics of the structure.

One of the purposes of the experiments described in this paper was to study the relationship between in-line and cross-flow response of long flexible cylinders under realistic field conditions. These tests were more realistic than laboratory ones, because it was possible to use cylinders of sufficient length so that many different natural modes could be excited, simultaneously, in both directions. The experiments at Castine were performed on flexible cylinders, 75 feet long, which were exposed to a uniform currents. Measurements taken included current, drag, tension and biaxial acceleration at seven locations unequally spaced along the test cylinder. Linear spectral analysis of lockin and non-lockin response data revealed little coherence between in-line and cross-flow vibration.

A frequency doubling relationship between cross-flow and in-line response has long been observed for lockin conditions and has been evident in an approximate sense in the broadband spectral characteristics typical of multi-moded non-lockin conditions. Quadratic operations are known to have frequency doubling characteristics.

Furthermore, by a least squares error minimization method, it was possible to evaluate the individual modal contributions for in-line and cross-flow motions under lockin and non-lockin conditions, thus enabling the computation of vibration energy. The results of modal analysis showed that there existed a strong correlation between the drag coefficient and the total vibration energy as well as a correlation between the in-line and cross-flow

Proceedings ASME, ETCE Conference, Paper No. OMAE-No-170, New Orleans, February 1986.

vibration energy. The evidence suggested that a spectral analysis technique capable of detecting quadractic system behavior was required. Bi-spectral analysis is specifically sensitive to quadratic relationships. The cross-bicoherence spectrum ultimately provided definitive evidence of a quadratic correlation between cross-flow and in-line response under both lockin and non-lockin conditions.

These conclusions were tested using data gathered on very long cables deployed in sheared currents under the ice in the Arctic in 1983 with similar conclusions.

THE EXPERIMENTS

Castine-1981

The site chosen for the experiment was a sandbar located at the mouth of Holbrook Cove near Castine, Maine. At low tide, the sandbar was exposed allowing easy access to the test equipment while at high tide it was covered by about 10 feet of water. The test section was oriented normal to the direction of the current which varied from 0 to 2.4 ft/sec over the tidal cycle with only small spatial differences over the section length at any given moment. The data taking station for the experiment was the R/V Edgerton, moored approximately 300 feet from the sandbar and chartered from the MIT Sea Grant Program. Figure 1 shows a schematic diagram of the test section.

A 75 foot long instrumented cable was developed specifically for this experiment. The outer sheath for the cable was a single piece of clear flexible PVC tubing, which was 1-1/4 inches in outer diameter by 1.0 inch in inside diameter. Three 1/8 inch diameter stainless steel cables ran through the tubing and served as tension carrying members. Seven biaxial pairs of accelerometers were placed along the cable at positions L/8, L/6, L/4, 2L/5, 5L/8, and 3L/4, where L is the length of the cable. The accelerometers were Sundstrand Mini-Pal Model 2180 Servo Accelerometers, which are sensitive to the direction of gravity. The biaxial pairing of these accelerometers made it possible to determine their orientation and hence extract real vertical (cross-flow) and horizontal (in-line) accelerations of the cable at the seven locations. For some tests the composite cable was placed inside a 1.631 inch O.D. by 1.493 inch I.D. steel tube, referred to as the pipe.

A load cell mounted at one end of the test cylinder measured the horizontal shear force on one end of the test cylinder. The cylinder and its two end supports were symmetric, and therefore the measured force was one half the total drag force on the cylinder. Mean drag force was measured. The load cell was a Sensotec Model 41, packaged for underwater use. The current was measured by a Neil Brown Instrument Systems DRCM-2 Acoustic Current Meter located 12.5 feet from the west end of the test cylinder and 2 feet upstream. It was set so that it determined the current at the level of the test cylinders. The current was found to be spatially uniform to within 3.0% from end to end for all current speeds above 0.5 feet per second. Additional details can be found in references 5, 6 and 7.

The Arctic-1983

During an Arctic cruise in the summer of 1983 on the Research Vessel Polarstern, cable strumming experiments were conducted in sheared currents near the ice edge in the Frahm Strait close to the eastern coast of Greenland. The cables, up to 2000 feet long, were suspended vertically under the ice and provided data with hundreds of modes responding simultaneously. Current profiles were recorded using the same acoustic current meter and acceleration was measured using biaxial pairs of piezoelectric accelerometers. For complete details see references 8 and 9.

PRELIMINARY ANALYSIS OF EXPERIMENTAL DATA

Castine Data

The orientation of the biaxial accelerometers was initially unknown. The accelerometers used were sensitive to gravity and gave a DC offset to the recorded signal in proportion to the vector component of gravity. From the DC offset the accelerometer orientation angle was obtained. After this angle was found, the in-line and cross-flow accelerations were obtained by performing a vector rotation.

Once the in-line and cross-flow accelerations were found, it was necessary to undertake a complex process to determine the displacement time histories by double integration. In the frequency domain, the transfer function of an integrator possesses a singularity at zero frequency. Therefore, low frequency noise components near this singularity blow up and smear the output signal from the integrator. To avoid this an effective filtering and integration procedure was developed. The details may be found in the thesis by Jong [10].

A broad view of the data may be obtained by examining compressed 2-1/2 hour records of drag coefficient, current speed, and RMS displacement response as shown in Figure 2. Data was collected on the rising tide. This example represents one complete experimental run.

The data shown were calculated by a moving average whose window was 8.53 seconds in length, which is long enough to average over many cycles of vibration but short enough to show subtle variations in behavior. The displacement data are taken from location L/6. Over the 2-1/2 hour span of time shown in the figure, some periods correspond to lockin response, and others to non-lockin. As current speed falls within a lockin range, a substantial increase of cross-flow and/or in-line RMS displacement is apparent. A corresponding elevated plateau in the drag coefficient is also observed. These are raw RMS displacements at the location specified and have not been corrected for mode shape. Due to the fact that these raw data are highly positional and mode shape dependent, the in-line and cross-flow RMS displacements in the figure do not give a good indication of any relationship existing between the two. A modal analysis is required to represent the behavior of the entire cylinder and to understand the relationship between in-line and cross-flow motion. It is instructive to begin with sample time histories typical of lockin and non-lockin behavior.

Lockin

Lockin occurs when the vortex shedding frequency falls within a few percent of a natural frequency of the cylinder. The vortex shedding process is synchronized with the cylinder's motion, and a stable, periodic, transverse displacement of nearly constant amplitude is observed. Figure 3 shows an example of a cross-flow displacement time history of the pipe at L/4 during lockin with the third mode. Figure 4 is the corresponding acceleration power spectrum, presented on a logarithmic scale. The dominant response peak is at 2.4 Hz. All spectra shown in this paper were computed using a 100 pole maximum entropy

spectral estimator [11]. The input was an autocorrelation function 34 seconds in maximum lag, computed from 136 seconds of data. The sampling rate was 30 Hz.

In the in-line direction, the motion is quite different. A periodic displacement of non-constant amplitude is apparent in Figure 5. Figure 6 presents the corresponding acceleration power spectrum. One important observation in this result is that the dominant frequency in the in-line direction is 4.8 Hz, exactly double that in the cross-flow direction. This frequency doubling phenomenon was always observed under lockin conditions.

By double integration of both measured in-line and cross-flow acceleration time histories, it is possible to plot the trajectory of the motion of a point on the cylinder. Figure 7 shows the motion at L/4 projected onto a plane which is normal to the cylinder axis (orbital diagram). This point on the pipe prescribed figure eight motions. In this case the cross-flow motion was locked-in with the third mode at 2.4 Hz. The in-line motion was primarily at twice the frequency of the cross-flow motion and was dominated by response in the fifth mode. The fifth mode natural frequency for this cylinder is twice that of the third mode. Though at different frequencies the two motions must be highly correlated.

At this point in the analysis, one does not generally know for certain which natural modes of vibration are responding. It will in fact be shown that the in-line response though sharply peaked near one frequency does not always correspond to a resonant natural frequency, as it does in this case. Under lockin conditions it is always at twice the cross-flow lockin frequency.

Non-lockin

When the vortex shedding frequency is outside of the lockin range, non-lockin vibration results. The response is characterized by random fluctuations of amplitude and frequency in both in-line and cross-flow directions. The lift force correlation length along the cylinder becomes much shorter than that at lockin. Figures 8 and 9 show typical acceleration power spectra in the cross-flow and in-line directions. Wide band lift and drag forces are implied. Figure 10 shows the corresponding orbital diagram; the random walk character of the figure gives no evidence of correlation. An important observation to be made is that spectral peaks in the in-line response occur at frequencies which are equal to the sums of various combinations of two spectral peak frequencies in the cross-flow direction. For example, peak E at 3.70 Hz is the sum of 1.70 and 2.00 Hz from peaks A and B. The frequency doubling and summing phenomena seen in the lockin and non-lockin data suggest non-linear quadratic correlation. Furthermore, linear coherence between displacements in the two directions is very low [10, 12]. In line response peaks for both lockin and non-lockin cases frequently do not correspond to natural frequencies. The subject of which modes account for this response is an interesting one and will be discussed in the next section.

MODAL ANALYSIS

In this section, a least squares error minimization method is used to estimate the modal displacements of all the participating modes. Vibration energies in both directions are then calculated from the modal displacements and the known mode shapes. By this method of modal analysis, the response of the cylinder can be expressed in terms of a superposition of mode shapes Yi(x) multiplied by the modal displacements Pi(t) [10, 13]:

$$y(x,t) = \sum_i Pi(t)Yi(x) \qquad (1)$$

In this experiment, the response was measured at seven unequally spaced positions. A least squares method was used to estimate the modal displacement time histories in terms of the measured responses at these seven positions. For each test case the response was dominated by a finite number of modes, usually two to six in number. A first guess at the responding modes was obtained by inspection of the response spectrum at any one location. By summing the normal mode responses over the apparent participating modes, the following equations are obtained, where the range M to N covers all of the participating modes. For taut, constant tension, pin-supported, uniform cylinders, the i-th mode shape is given by a sinusoidal curve as:

$$Yi(x) = \sin(i\pi\, x/L) \qquad (2)$$

At time t=to, the response of position x=xj can be expressed as:

$$y(xj,to) = \sum_{i=M}^{N} Pi(to)Yi(xj) + E(xj) \qquad (3)$$

Where E(Xj) is the error term.

Rewriting (3) in matrix form,

$$(y) = [Y]\,(P) + (E) \qquad (4)$$

where

yj is an element in the vector of the measured response at to.
Yij is an element in the mode shape matrix.
Pi is an element in the vector of the natural coordinates at to.
Ej is the error vector.

i=M,N j=1,7

The sum of error squares ee is given by

$$ee = (E)^T(E) = ((y) - [Y](P))^T((y) - [Y]\,(P))$$

$$= (y)^T(y) - 2(P)^T[Y]^T(y) + (P)^T[Y]^T[Y](P) \qquad (5)$$

The vector of natural coordinates Pi is to be determined such that the error squared term is minimized.

$$\min[ee] = \min\,[(E)^T(E)] \qquad (6)$$

Let

$$\frac{d}{dPi}(ee) = 0 \qquad (7)$$

and solve for P(t).

$$(P) = [[Y]^T[Y]]^{-1}[Y]^{-1}(y) \qquad (8)$$

or

$$(P) = [T]\,(y) \qquad (9)$$

where [T] is the transfer matrix:

$$[T] = [[Y]^T[Y]]^{-1}[Y] \quad (10)$$

Equation (9) decomposes the measured response at the seven positions into the natural coordinates, provided the mode shapes are known and the guess of the responding modes is initially correct. Figure 11 shows an example of the in-line pipe displacement at position L/8. In the displacement spectrum, there are several peaks, each likely corresponding to one particular mode to be identified. Using the method discussed above, the natural coordinate time histories were obtained for the 4th, 5th, 6th, and 7th modes. These modal displacement time histories are shown in Figure 12. Each time history represents an antinode displacement for that mode expressed in inches. A scale of -1 to +1 inch is shown on the figure. All modal time histories are to be considered to have a zero mean. Their sum correctly weighted by the value of the respective mode shapes at any particular location would equal the displacement at that point.

At constant current speed, when the cylinder is at non-lockin, the participation of different contributing modes varies with time as illustrated in Figure 12. It is enlightening to study this feature of non-lockin response on a longer time scale. A 448-second record of non-lockin pipe response was analyzed and the contributing modal displacements were evaluated. Moving average RMS modal displacement responses in both directions were calculated. These are plotted in inches in Figures 13 and 14. The RMS value of the individual modal antinode responses are shown. Notice that as the response of one mode recedes, another appears to take its place.

The amplitude scales on Figures 13 and 14 are to be interpreted as follows. Each modal RMS amplitude is plotted above a horizontal line representing zero deflection for that mode. If the scale given on the left edge of the figure and spanning 0 to 2.0 inches is moved upwards until zero corresponds to the zero line for the mode of interest then the response can be read off directly. For example, the maximum RMS response for mode two is approximately 0.72 inches.

The same graphical scaling method is used in Figure 15 except that the units of energy are foot-pounds and of current speed are feet per second. Drag coefficient is dimensionless.

Moving average vibration energies were calculated from these natural coordinates and mode shapes in both in-line and cross-flow directions as shown in Figure 15. The vibration energy is given by

$$E(t) = L/4 \sum_i [EI \cdot Pi^2(t)(i\pi/L)^4 + T \cdot Pi^2(i/L)^2 + m \cdot \dot{Pi}^2(t)] \quad (11)$$

Obvious correlations exist between in-line and cross-flow vibration energy and between vibration energy and drag coefficient can be seen in Figure 15. The high plateaus in drag coefficient and response energy correspond to periods when one mode was able to dominate the response and lockin or partial lockin over a portion of the cylinder existed. This figure represents flow conditions at the boundary between lockin and non-lockin behavior. A scatter diagram of the in-line vibration energy versus drag coefficient is plotted in Figure 16. The temporal history is retained by connecting successive points as indicated by the arrows. A very clear memory phenomena is revealed. Drag coefficients are higher going into lockin than coming out.

As mentioned before, the in-line response frequencies are equal to the sums of pairs of cross-flow response frequencies. It is usually not obvious which in-line modes respond. Modal identification methods were used to provide the answer, with some very surprising results. One interesting case is described below.

For a taut cable, all of the natural frequencies are integer multiples of the lowest. Therefore, under lockin conditions, it is reasonable to expect that the fluctuating drag forces will excite an in-line mode whose natural frequency is twice that of the mode which is responsible for the cross-flow lockin. This is not always the case, as will be shown. In the example, a modal analysis of data taken with the bare cable revealed that the cross-flow vibration was second-mode lockin. It was expected that the unsteady drag forces would excite the fourth in-line mode, because its natural frequency was the same as the drag force fluctuations. However, modal analysis revealed that in-line motion was third mode, instead of the fourth mode as had been expected. The frequency of this third motion was not the natural frequency of the third mode but was in fact equal to the natural frequency of the fourth mode. The response was not resonant with the fourth mode, but was inertia controlled response of the third mode.

Though not initially obvious, the explanation is quite simple and applies to all taut cables and pipes with sinusoidal mode shapes. Under lockin conditions the shedding of vortices over the entire cylinder is essentially simultaneous, independent of the cross-flow mode shape. Regardless of the symmetry of the cross-flow mode shape with respect to the center of the cylinder the in-line drag force fluctuations are symmetrically distributed. Therefore, the in-line modal force for all even numbered modes is zero. In this example, although the drag force fluctuations were at the natural frequency of the fourth in-line mode, (an anti-symmetric mode) the dominant modal force corresponded to the third mode, (a symmetric mode) resulting in non-resonant third mode motion [10].

Similar peculiar results of non-resonant, in-line motion also happened under non-lockin conditions and can be explained with an understanding of the quadratic relationship between in-line and cross-flow response.

BISPECTRAL ANALYSIS OF QUADRATIC CORRELATION

From the results of modal analysis there was substantial evidence of a quadratic relationship between in-line and cross-flow response. Higher order spectral analysis was required to study the correlation between time histories resulting from a nonlinear process. The bispectrum was used here to investigate the quadratic coupling between response in the cross-flow and in-line directions [10]. General references on nonlinear spectral analysis are 14, 15, 16, and 17.

For a stationary random time series x(t) the auto-bispectrum, B(Wj,Wk), of x(t) is defined as:

$$Bxxx(Wj,Wk) = E[Xj \cdot Xk \cdot X^*j+k] \quad (12)$$

where Wj and Wk are discrete frequencies at which a Fourier transform has been computed. Xj and Xk are the Fourier transform coefficients computed from the time series x(t) at frequencies Wj and Wk and X*j+k is the complex conjugate of the coeffiecient at Wj+k.

The mathematical definition of the Fourier transform used is:

$$Xk = 1/T \int_0^T x(t)\exp(i \cdot Wk \cdot t)dt \qquad (13)$$

E[ ] is the expectation operator and is computed as an ensemble average. In this paper the bispectrum calculations were made in the following way. A stationary time series was sampled at 30 Hz. Fast Fourier transforms of 100 segments, all 128 samples in length were computed. Ensemble averages using the 100 realizations were used to compute each bispectrum point. The frequency resolution is therefore 0.23 Hz and the maximum frequency in the spectrum is 15 Hz. The results are more easily understood when plotted as coherence functions.

The auto-bicoherence spectrum, a normalized auto-bispectrum is:

$$bxxx(Wj,Wk) = \frac{|Bxxx(Wj,Wk)|}{\{E[|Xj \cdot Xk|^2]E[|X^*j+k|^2]\}^{1/2}} \qquad (14)$$

By using Schwarz's inequality, it can be shown that auto-bicoherence spectrum is bounded by 0 and 1. If the component at Wj + Wk, is related by nonlinear quadratic coupling the auto-bicoherence spectrum will be close to unity. On the other hand, if the component at Wj + Wk is uncorrelated quadratically to the components at Wj and Wk, the autobicoherence will be near zero. For this application the cross-bispectrum between two time series x(t) and y(t) is the most useful.

Let x(t) and y(t) be two zero mean jointly stationary time series, the cross-bispectrum between x(t) and y(t) is:

$$Bxxy(Wj,Wk) = E[Xj \cdot Xk \cdot Y^*j+k] \qquad (15)$$

The cross bicoherence spectrum between x(t) and y(t) is:

$$bxxy(Wj,Wk) = \frac{|Bxxy(Wj,Wk)|}{\{E[|Xj \cdot Xk|^2]E[|Y^*j+k|^2]\}^{1/2}} \qquad (16)$$

The cross bicoherence spectrum also ranges from zero to unity. Bicoherence functions require three dimensional plots, one axis each for frequencies Wj and Wk and a magnitude axis.

Lockin Example

Figures 4 and 6 show the acceleration spectra for cross-flow and in-line motion under lockin conditions. The principal cross-flow peak occurs at 2.4 Hz and the principal in-line response peak occurs at 4.8 Hz. The cross-bicoherence for this case, Figure 17, has its highest peak at frequencies (fj, fk) = (2.4 Hz, 2.4 Hz). These figures are presented showing frequencies on two axes. The height is to be interpreted as resulting from moving the base of any peak of interest down to the horizontal axis and then estimating the peak height on the vertical scale of zero to 1.0, shown at the left of the figure. The vertical frequency axis goes from 0 to 7.5 Hz as shown on the right of the figure. Therefore, peak X has a height of 1, and corresponds to a sum frequency of 2.4 Hz + 2.4 Hz = 4.8 Hz. This essentially perfect coherence is the result of a quadratic relationship between the 2.4 Hz vibration energy in the cross-flow motion and the 4.8 Hz motion in-line.

Non-Lockin Example

Figures 8 and 9 show cross flow and in-line response spectra at non-lockin. The cross-bicoherence for this case is given in Figure 18. The peaks labelled X, Y and Z demonstrate the quadratic coherence between peaks E,F and G in the in-line spectrum and peaks A, B, C and D in the cross flow spectrum. For example, the peak E at 3.70 Hz in the in-line spectrum occurs at the sum of frequencies at A and B (1.70 + 2.00 Hz). The quadratic relationship is confirmed in peak X in Figure 18 which is at (fj, fk) = (1.7, 2.0 Hz) and is near unity in height. Other similar correlations are specifically indicated in the figure.

Sheared Current

The bispectrum results shown so far are for the uniform flow low modal density data obtained at Castine. To investigate the extent to which the hypothesis of quadratic correlation can be generalized, a much different data set was needed. The Arctic experiments conducted by Vandiver and Kim were in sheared flows, using cables which were long enough to have flow induced vibration properties characteristic of infinitely long cables [8,9].

The test cable, 975 feet in length, in this example, was suspended vertically from a research vessel with a heavy weight at the bottom end. An accelerometer was located at 100 feet from the bottom end of the cable orientated at an unknown angle to the flow. The measured response had both in-line and cross-flow response components in it. Figure 19 shows on a linear scale the FFT power spectrum of the measured response with peaks at 4, 8, 12 and 16 Hz. Figure 20 shows the auto-bicoherence for this data revealing numerous peaks of high coherence. The most notable one is at (fj, fk) = (8.0, 4.0 Hz). Thus demonstrating that quadratic correlation exists even in a long cable, with sheared flow.

CONCLUSIONS

A variety of field vibration data has been used to demonstrate that for all conditions studied including lockin, non-lockin uniform and sheared flow, quadratic correlation exists between in-line and cross-flow vibration components.

These results suggest that the time series modelling or prediction of the vibration response of marine risers, cables, pipelines and other cylinders exposed to currents should take into account these nonlinear correlations. This is especially true when fatigue damage prediction is a concern, because fatigue is dependent on stress statistics and these depend on the correlation between various vibration components.

When estimating stress statistics for mechanical systems it is desirable and often assumed that the stress time histories can be modelled as Gaussian random processes. It is a mathematical fact that if the bispectrum of a time series is non-zero, the time series is not the result of a Gaussian or normally distributed random process. It is not appropriate to model flow induced vibration as Gaussian random processes.

This paper has demonstrated strong quadratic correlation between cross-flow and in-line vibration caused by vortex shedding. This suggests that it should be possible to identify the second order nonlinear transfer function which can relate the cross-flow to the in-line vibration. In other words, given the cross-flow time series and the proper

non-linear transfer function, one should be able to model or predict the resulting in-line vibration. This has been done by the authors and is presented in references [10 and 12].

ACKNOWLEDGEMENTS

This research represents a segment of a multiyear program at M.I.T. focussed on the umderstanding of flow-induced vibration. The overall program has had broad federal and industrial support. This particular portion was sponsored by the Technology Assessment and Research Branch of the Minerals Management Service and by the Marine Technology Division of the Naval Research Laboratory.

REFERENCES

1. Griffin, O.M. and Ramberg, S.E., "Some Recent Studies of Vortex Shedding With Application to Marine Tubulars and Risers," Journal of Energy Resources Technology, vol. 104, March 1982.

2. King, R., "A Review of Vortex Shedding Research and Its Application," Ocean Engineering, Vol. 4., pp. 141-171., Pergamon Press, 1977.

3. Sarpakaya, T., "Vortex-Induced Oscillations, A Selective Review," ASME Journal of Applied Mechanics, vol. 46, June 1979, pp. 241.

4. Vandiver, J.K., "The Prediction of Lockin Vibration on Flexible Cylinders in a Sheared Flow," Proc. 1985 Offshore Technology Conference, paper No. 5006, Houston, Texas May 1985.

5. McGlothlin, J.C., "Drag Coefficients of Long Flexible Cylinders Subject to Vortex-Induced Oscillation," S.M. Thesis presented to the Massachusetts Institute of Technology, Cambridge, Massachusetts, 1981.

6. Vandiver, J.K., "Drag Coefficients of Long Flexible Cylinders," Proc. Offshore Technology Conference, paper No. 4490, 1983.

7. Griffin, O.M. and Vandiver, J.K., "Vortex-Induced Strumming Vibrations of Marine Cables with Attached Masses," Journal of Energy Resources Technology, vol. 106, December 1984.

8. Kim, Y.-H., Vortex-Induced Response and Drag Coefficients of Long Cables in Ocean Currents," Ph.d. thesis, MIT, Department of Ocean Engineering, 1984.

9. Kim, Y.-H., Vandiver, J.K., Holler, R., "Vortex-Induced Vibration and Drag Coefficients of Long Cables Subjected to Sheared Flows," Proc. 4th International Offshore Mechanics and Arctic Engineering Symposium, vol. 1, ASME 1985. Book No. 10185A, J.S. Chung Editor.

10. Jong, J.-Y., "The Quadratic Correlation Between In-Line and Cross-Flow Vortex-Induced Vibration of Long Flexible Cylinders," Ph.d. thesis, MIT, Department of Ocean Engineering, 1984.

11. Campbell, R.B. and Vandiver, J.K., "The Determination of Modal Damping Ratios from Maximum Entropy Spectral Estimates," ASME J. Dynamic Systems Measurement and Control, vol. 104 March 1982.

12. Jong, J.-Y. and Vandiver, J.K., "The Identification of the Quadratic System Relating Cross-Flow and In-Line Vortex-Induced Vibration," ASME Proc., 1985 Winter Annual Meeting.

13. Meirovitch, Leonard, Analytic Methods in Vibrations, MacMillan Co., New York, 1967.

14. Brillinger, D.R., Time Series, Holt, New York, 1975.

15. Brillinger, D.R. and Rosenblatt, M., "Asymptotic Theory of Estimate of K-th Order Spectra," in Spectral Analysis of Series, B. Harris Ed., Wiley, New York, 1967.

16. Kim, Y.-C. and Power, E.J., "Digital Bispectral Analysis and its Application to Nonlinear Wave Interactions," IEEE Transactions on Plasma Science, vol. PS7, no. 2, June 1979.

17. Kim, Y.-C., Wang, W.-F., Powers, E.J., and Roth, J.R., "Extension of the Coherence Function to Quadratic Models," Proceedings of the IEEE, vol. 67, no. 3, March 1979.

Table 1. English to S.I. Conversion Factors

Length	1.0 ft	=	.3048 m
	1.0 in	=	.0254 m
Velocity	1.0 ft/s	=	.3048 m/s
Acceleration	1.0 in/s^2	=	.0254 m/s^2
Force	1.0 lbf	=	4.448 N
Energy	1.0 ft-lbf	=	1.355 J

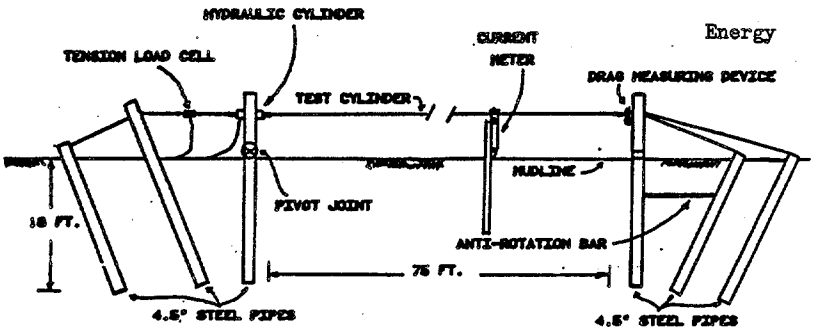

FIGURE 1. SCHEMATIC DIAGRAM OF THE EXPERIMENT TEST SECTION

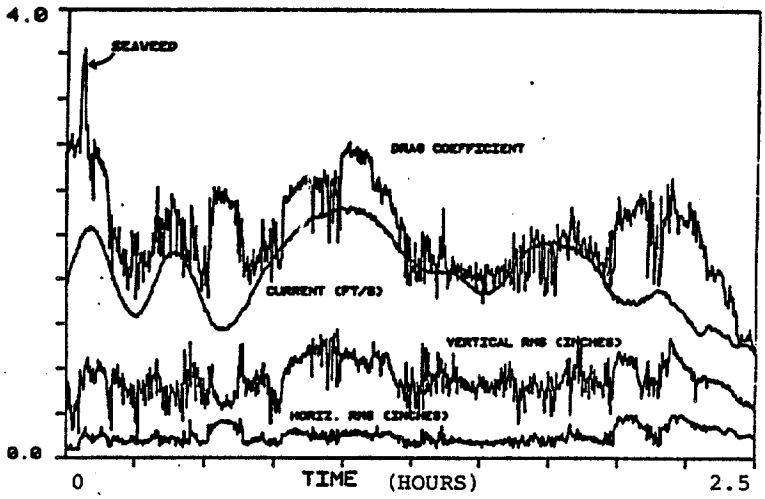

Figure 2. Moving Average Record of the RMS Displacement, Current, and Drag Coefficient for the Pipe at L/8

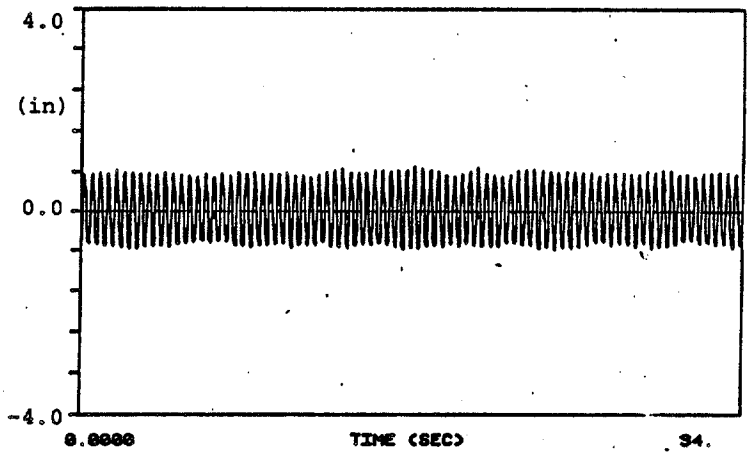

Figure 3. Cross-Flow Displacement at Lockin

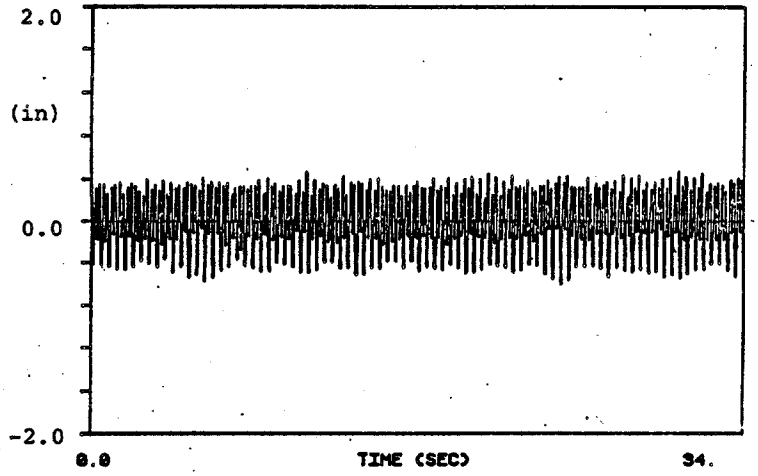

Figure 5. In-Line Displacement at Lockin

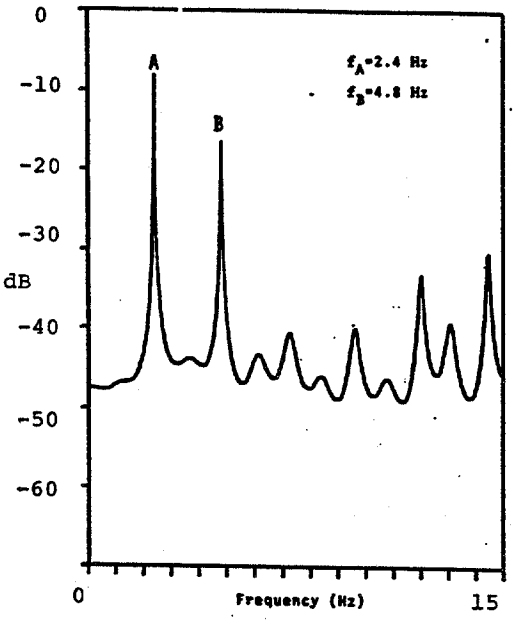

Figure 4. Acceleration Spectrum of Cross-Flow Response at Lockin

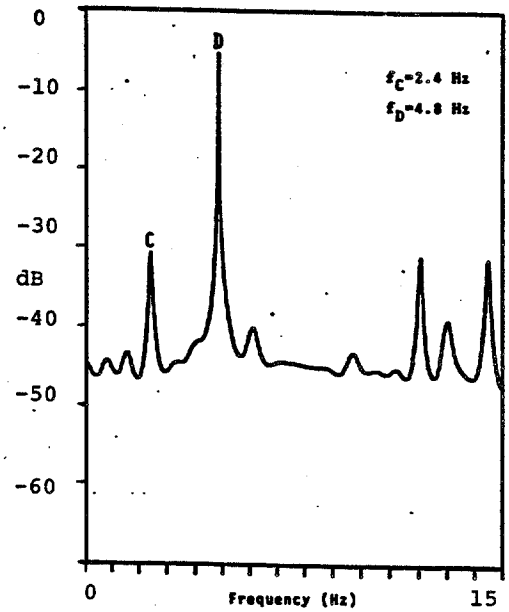

Figure 6. Acceleration Spectrum of In-Line Response at Lockin

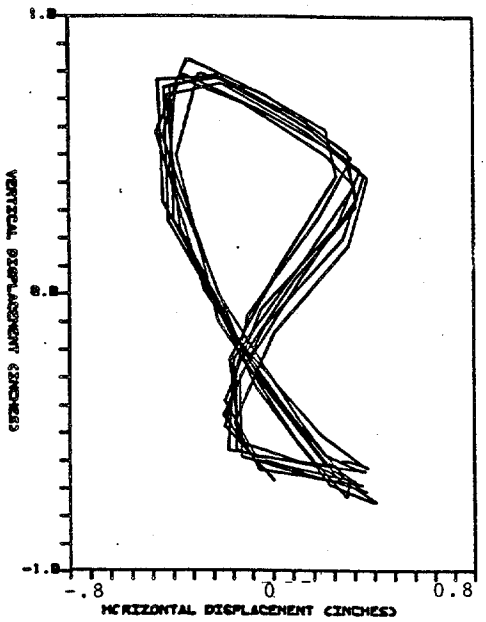

Figure 7. Orbital Motion at L/4 at Lockin

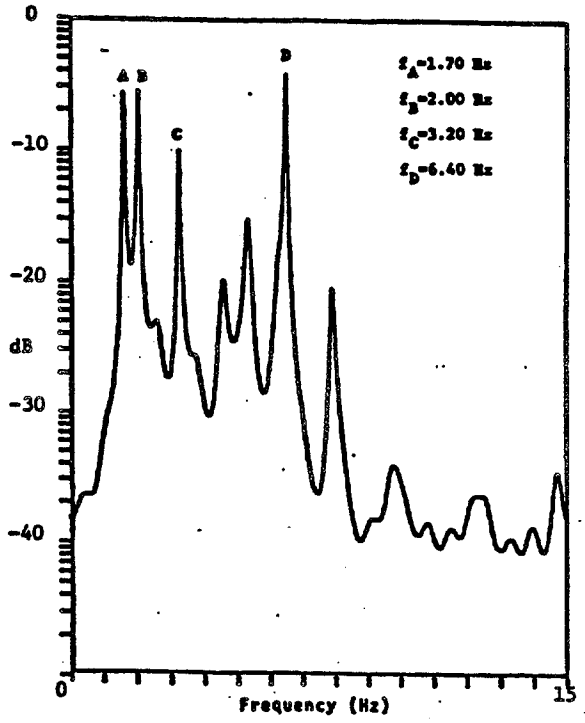

FIG. 8 Power Spectrum of Cross-Flow Acceleration at Non-Lockin

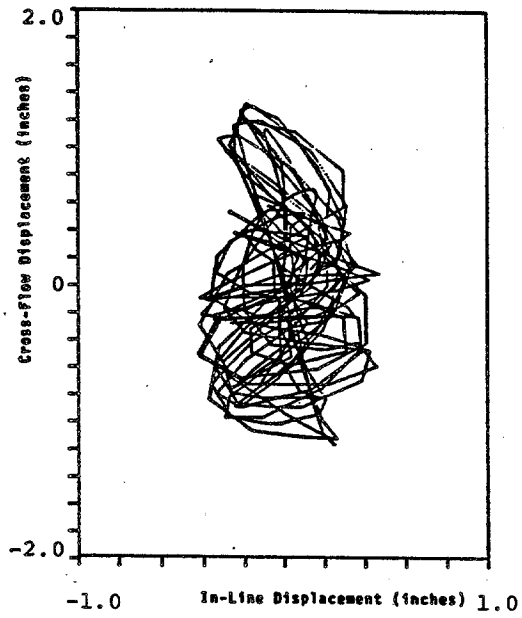

Figure 10. Orbital Motion at L/8 at Non-Lockin

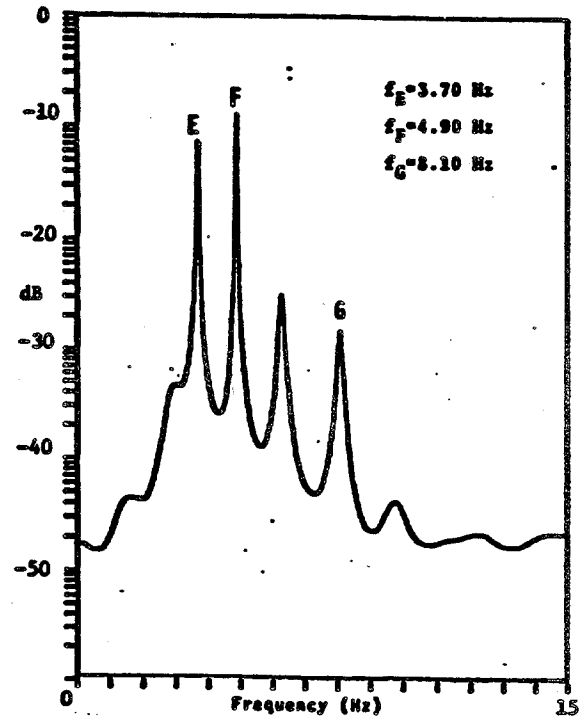

FIG. 9 Power Spectrum of In-Line Acceleration at Non-Lockin

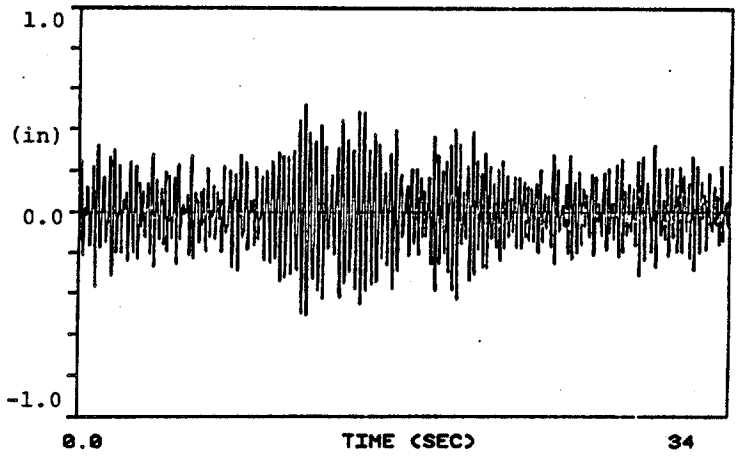

Figure 11. In-Line Displacement at L/8 at Non-Lockin 4th, 5th, 6th, and 7th Modes Responding

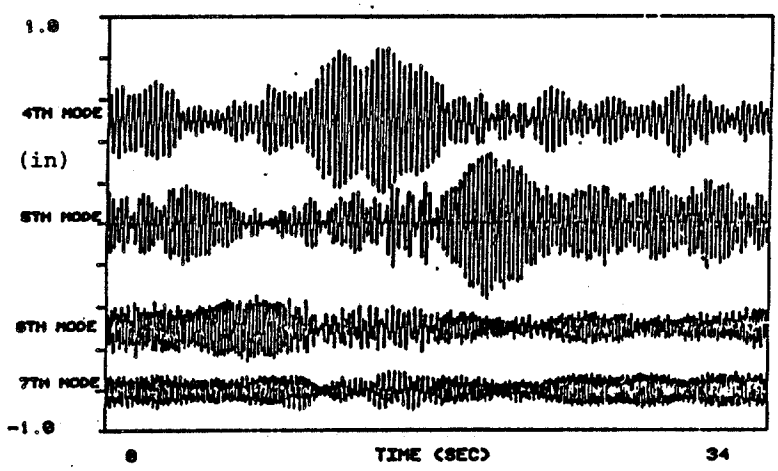

Figure 12. Natural Cooridinate Time Histories for the 4th, 5th, 6th, and 7th In-Line Modes of the Pipe

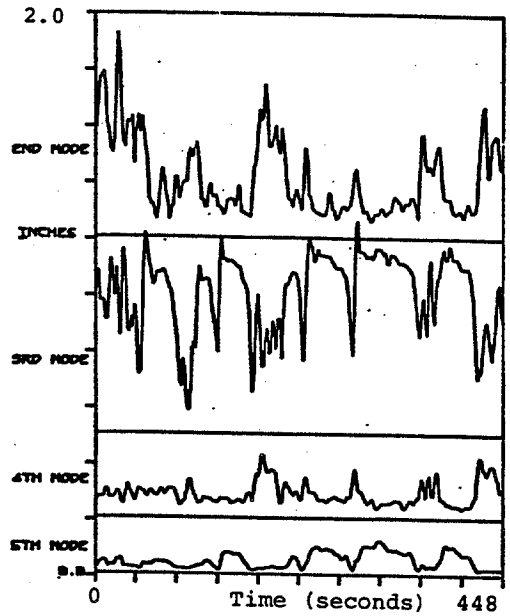

Figure 13. Natural Coordinate RMS Displacements for the 2nd, 3rd, 4th, and 5th Cross-Flow Modes of the Pipe

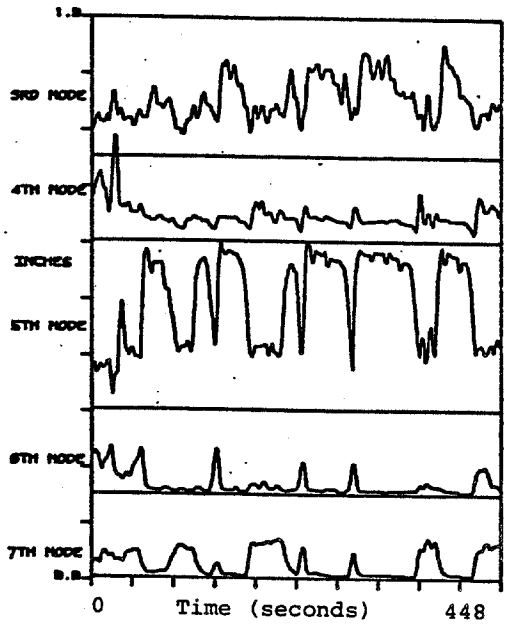

Figure 14. Natural Coordinate RMS Displacements for 3rd, 4th, 5th, 6th, and 7th In-Line Modes of the Pipe

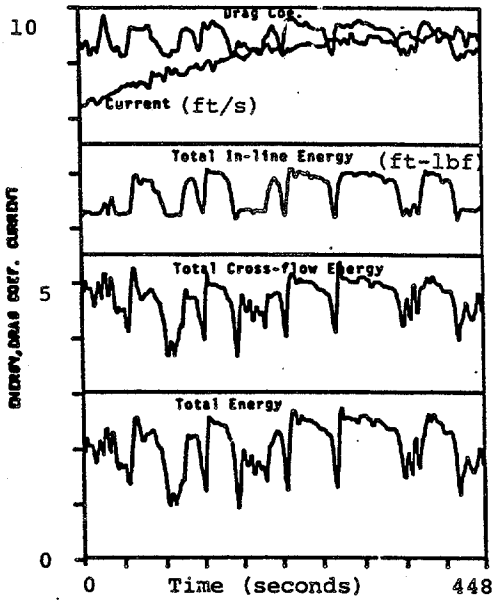

Figure 15. Drag Coefficient, Current (ft/s), Vibration Energy(ft-lbf)

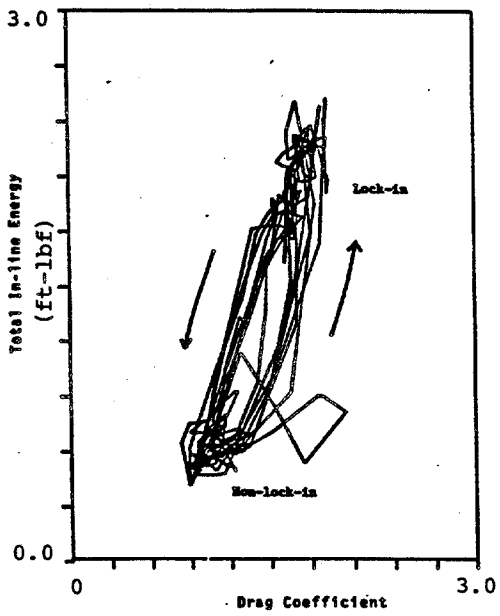

Figure 16. Drag Coefficient vs. Total In-Line Vibration Energy

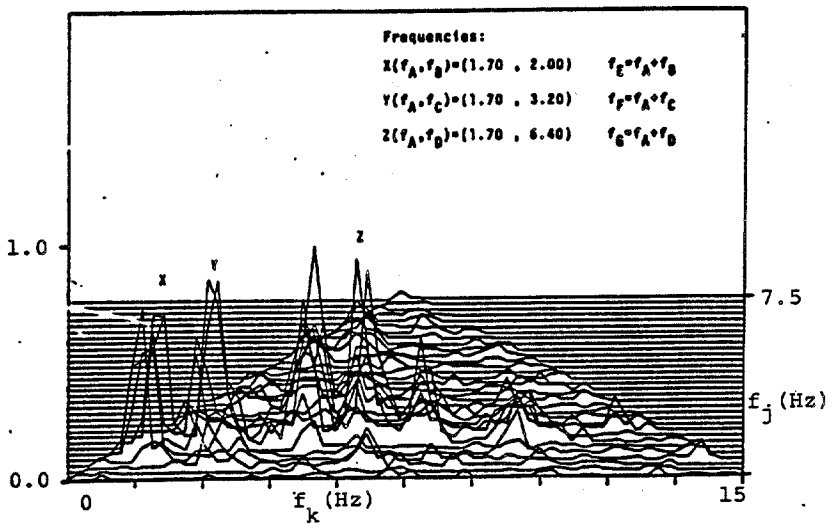

Figure 18. Cross-Bicoherence Between Cross-Flow and In-Line Response at Non-Lockin

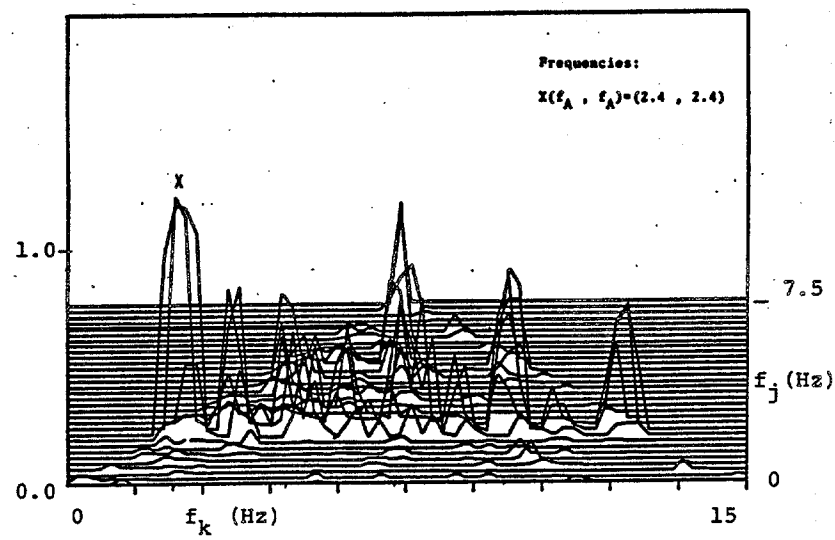

Figure 17. Cross-Bicoherence Between Cross-Flow and In-Line Response at Lockin

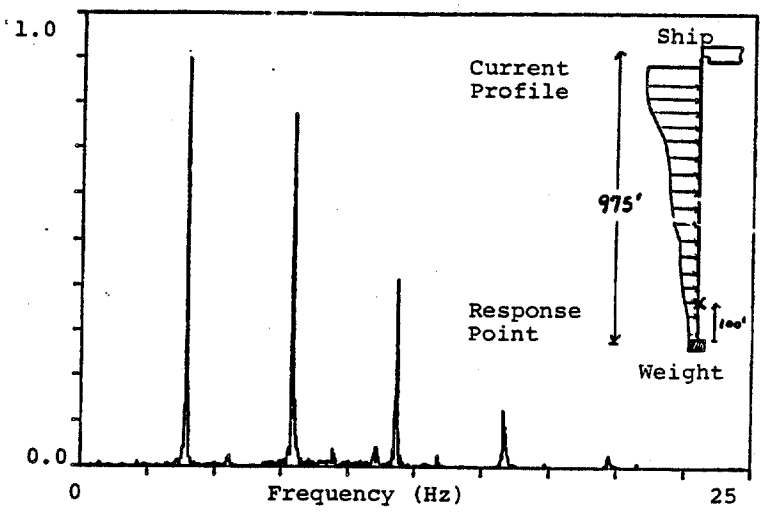

Figure 19. Linear Spectrum of Acceleration Response From the Arctic Experiment

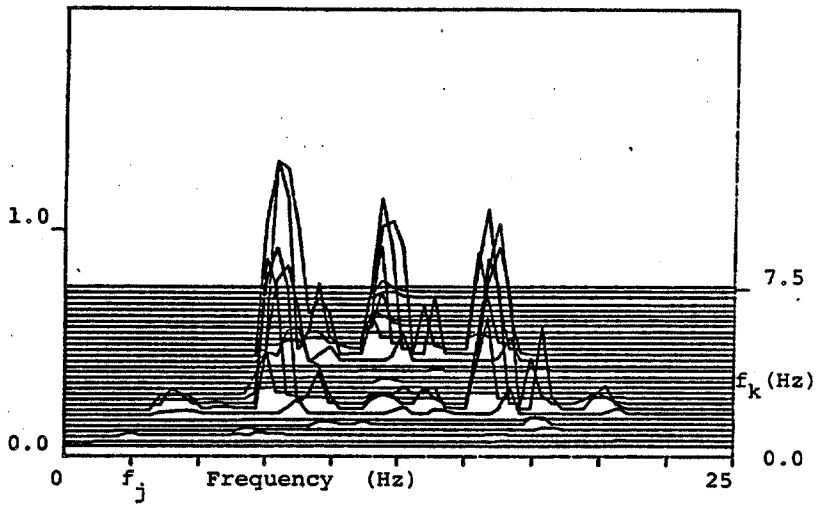

Figure 20. Auto-Bicoherence of Single Axis Acceleration Data from the Arctic

THE IDENTIFICATION OF THE QUADRATIC SYSTEM RELATING CROSS-FLOW AND IN-LINE, VORTEX-INDUCED VIBRATION

BY

Jen-Yi Jong, Wyle Laboratories

J. Kim Vandiver, Massachusetts Institute of Technology

ASME, WINTER ANNUAL MEETING
NOVEMBER 1985

ABSTRACT

This paper presents an application of the multiple regression method to the identification of the nonlinear relationship between cross-flow and in-line, vortex-induced vibration. Previous results of bispectral analysis of the Castine data by Jong [7] indicated that cross-flow and in-line response are correlated quadratically for both lock-in and non-lock-in cases. Therefore, a second order nonlinear system was used to model the relationship between cross-flow and in-line vibration. The cross-flow response is treated as the input to the nonlinear system and the in-line response is defined as the output. Both time domain and frequency domain multiple regression methods are presented in the evaluation of the quadratic system function under lock-in and non-lock-in conditions respectively. Nonlinear input/output correlations higher than second order in the relationship are shown to be negligble.

NOMENCLATURE

$x(t)$	cross-flow acceleration
$y(t)$	in-line acceleration
$y_1(t)$	output from the Case 1 square law operator
$y_2(t)$	output from the Case 2 square law operator
$y_s(t)$	simulated in-line response
y_o	d.c. component of the in-line response
$n(t)$	noise
$g(u,v), g_1(\ ), g_2(\ )$	second order impulse response function
$h(u)$	linear impulse response function
$G(w)$	special form of $g(u,v)$
K	order of linear convolution
M	order of the second order convolution
$G(W_1,W_2), G_1(W_1,W_2) G_2(W_1,W_2)$	Fourier transforms of g, g_1, and g_2
$H(w), H_1(W), H_2(W)$	Fourier transform of $h(u)$, $h_1(w)h_2(u)$
MSE	mean square error
$E[\ ]$	expected value operator
$Sxx(W)$	auto spectrum of $x(t)$
$Sxy(W)$	cross spectrum of $x(t)$ and $y(t)$
$Bxxx(Wp,Wq)$	auto bispectrum of $x(t)$
$Bxxy(Wm,Wn)$	cross bispectrum of $y(t)$ and $x(t)$
W	frequency (radians/sec)
$\delta(\ )$	delta function
$\underline{I}$	unity vector
$\underline{\ }$	underscore indicates a vector
$[\ ]$	square brackets indicate a matrix

INTRODUCTION

Marine risers, pipelines, and hydrophone cables are all examples of structures subjected to vortex-induced vibration. The response of the cylinder depends on a complex interaction between the natural modes of the vibration and the vortex-shedding process. The implementation of good design procedures that account for strumming vibration is becoming more essential as the offshore industry moves into deeper water.

In a spatially uniform flow, lock-in may occur when the vortex-shedding frequency is within a few percent of a cylinder's natural frequency. Sustained periodic vibration results in both in-line and cross-flow directions. The cross-flow motion is dominated by one mode at the natural frequency of the cylinder. The in-line motion is dominated by a frequency twice that of the cross-flow motion. Typical in-line amplitudes are one-half that of the cross-flow displacement [8].

When the shedding frequency is outside the lock-in bandwidth, non-lock-in occurs and the response time histories in both in-line and cross-flow directions are best described as random processes. Several modes may respond in both directions. The cross-flow response frequencies are generally dominated by natural frequencies of the cylinders. The response frequencies typical of the in-line motion are not typically natural frequencies, but are most closely associated with sums of frequencies of dominant cross flow spectral peaks. The evidence of frequency doubling and summing under lock-in and non-lock-in conditions supports the hypothesis that in-line and cross-flow response are non-linearly correlated. As an initial test a bispectral analysis of flow induced vibration data obtained during a field test at Castine, Maine, was performed by Jong [7]. A very clear nonlinear correlation was evident between in-line and cross-flow vibration. The cross-bicoherence provided conclusive evidence that cross-flow and in-line response are correlated

quadratically for both lock-in and non-lock-in cases. These conclusions suggested that, in general, a second order nonlinear system can be used to model the relationship between cross-flow and in-line response.

The data analyzed in this paper was gathered during a field test in Castine, Maine in 1981. The experimental arrangements are described in Refs. 7 and 17 and are very briefly described here. A steel tube 75 feet long (22.86 m) and 1.625 inches in diameter (4.13 cm) was suspended horizontally under tension between two pilings. A spatially uniform tidal current normal to the longitudinal axis of the cylinder provided the vortex related excitation. Tension, current, drag force, and seven biaxial cylinder accelerations were recorded. Reynolds numbers of 300 to 20,000 were encountered.

The purpose of the research described in this paper was to examine the adequacy of a second order system in modelling flow induced vibration as observed in the Castine tests and to show that significant contributions, due to higher order nonlinearities, do not exist. To address this issue a quadratic system identification was performed for both the previous lock-in and non-lock-in cases. Due to the nature of nearly deterministic lock-in response, a time domain, multiple regression method was applied in the system identification procedure, while a frequency domain error minimization method was used for the non-lock-in, random vibration cases. The results showed that nonlinearities higher than second order were negligible for both lock-in and non-lock-in. Linear and second order correlation exist at lock-in. Whereas, in-line and cross-flow responses were linearly independent at non-lock-in and quadratic correlation accounted for all but a small amount of the nonlinear correlation between in-line and cross-flow vibration.

QUADRATIC SYSTEM IDENTIFICATION AT LOCK-IN

Initially, the bispectrum analysis was used to identify the quadratic correlation between cross-flow and in-line vibration. In this section, the relationship between cross-flow and in-line response is modelled with a second order nonlinear system, including a linear term and quadratic term. An error term is also introduced to represent imperfections of the model which might be due to the existence of the higher order nonlinearities. The linear and quadratic impulse response functions are identified for the lock-in case by using a time domain multiple regression method. By one and two dimensional convolution of the identified linear and quadratic impulse response functions with the measured cross-flow response, the in-line response can be predicted. The predicted and measured in-line response agree very well, as will be demonstrated with Castine field test data.

Application of Multiple Regression Analysis

Let the input x(t) be the cross-flow response, and output y(t), the in-line response. x(t) and y(t) are assumed to be related by a second order system as follows.

$$y(t) = yo + \sum_{u=0}^{k-1} h(u)x(t-u) + \sum_{u=0}^{M-1}\sum_{v=0}^{M-1} g(u,v)x(t-u)x(t-v)+n(t) \qquad (1)$$

where n(t) is the error term, h(u) is the linear impulse response function and g(u,v) is the second order impulse response kernel. Given the measured input and output data, x(t) and y(t)=1,2,...(N+K-1), the system functions h(u) and g(u,v) are to be determined in such a way that the estimated mean square error (MSE) is minimized. It was assumed with no loss of generality, that the second order impulse response kernel is symmetrical in its arguments:

$$g(u,v)=g(v,u) \qquad (2a)$$

and thus their Fourier transforms are also symmetrical

$$G(W_1,W_2)=G(W_2,W_1) \qquad (2b)$$

Consequently, the quadratic transfer function is symmetric about the line $W_1=W_2$ in the bi-frequency plane. Equation (1) can then be rewritten in matrix form as:

$$\underline{y}=\underline{yo}+[x]\underline{h}+[z]\underline{G}+\underline{n} \qquad (3)$$

where

unknowns h(u) u=0,1,...,K-1

unknowns g(u,v) u=0,1,...,M-1 v=0,1,...,M-1

NN=N+K-1 , MM=M(M+1)/2

z(t,w)=x(t-u)x(t-v) with w=v+M*u-u(u+1)/2

$$G(w)=\begin{cases} g(u,v) & \text{if } u=v \\ 2g(u,v) & \text{if } u\neq v \end{cases}$$

$\underline{h}=[\ h(0),h(1),.....h(K-1)]^T$ Kx1 vector

$\underline{y}=[y(K),y(K+1),.....y(NN)\ ]^T$ Nx1 vector

$\underline{n}=[\ n(K),n(K+1),.....n(NN)\ ]^T$ Nx1 vector

$\underline{yo}=[\ yo,yo,.....yo\ ]^T$ Nx1 vector

$\underline{G}=[G(0),G(1),.....G(MM-1)\ ]^T$ MMx1 vector

$$[x]=\begin{bmatrix} x(K) & x(K-1) & x(K-2).....x(1) \\ x(K+1) & x(K+2) & x(K+3).....x(2) \\ \vdots & & \\ x(N+K-1) & x(N+K-2) & .....x(N) \end{bmatrix}$$
NxK matrix

$$[z]=\begin{bmatrix} z(K,0) & z(K,1).....z(K,MM-1) \\ z(K+1,0) & z(K+1,1)....z(K+1,MM-1) \\ \vdots & \\ z(K+N-1,0) & z(K+N-1,1)..z(K+N-1,MM-1) \end{bmatrix}$$
NxMM matrix

the MSE can be written as

$$MSE=\underline{n}^T[\underline{n}] =$$

$$(\underline{y}-\underline{yo}-[x]\underline{h}-[z]\underline{G})^T(\underline{y}-\underline{yo}-[x]\underline{h}-[z]\underline{G})=$$

$$\underline{y}^T\underline{y}-2\underline{h}^T[x]^T\underline{y}-2\underline{G}^T[z]^T\underline{y}+$$

$$2\underline{h}^T[x]^T[z]\underline{G}+\underline{h}^T[x]^T[x]\underline{h}+$$

$$\underline{G}^T[z]^T[z]\underline{G}-\underline{yo}^T(\underline{y}-[x]\underline{h}-[z]\underline{G})-$$

$$(\underline{y}^T-\underline{h}^T[x]^T-\underline{G}^T[z]^T)\underline{yo}+$$

$$\underline{yo}^T\underline{yo} \qquad (4)$$

Seeking minima in the MSE with respect to yo, hi, and Gi leads to:

let $\partial MSE/\partial yo = 0$, resulting in

$$N*yo+\underline{I}^T[x]\underline{h}+\underline{I}^T[z]\underline{G}=\underline{I}^T\underline{y} \qquad (5)$$

let $\partial MSE/\partial hi = 0$, resulting in

$$([x]^T[z]\underline{G}+([x]^T[x])\underline{h}+yo[x]^T\underline{I}=[x]^T\underline{y} \qquad (6)$$

let $\partial MSE/\partial Gi = 0$, resulting in

$$([z]^T[x])\underline{h}+([z]^T[z])\underline{G}+yo[z]^T\underline{I}=[z]^T\underline{y} \qquad (7)$$

These three equations can be combined and rewritten as

$$\begin{bmatrix} [M1] & [C] & \underline{Q1}^T \\ [C]^T & [M2] & \underline{Q2}^T \\ \underline{Q1} & \underline{Q2} & N \end{bmatrix} \cdot \begin{Bmatrix} \underline{h} \\ \underline{G} \\ yo \end{Bmatrix} = \begin{Bmatrix} \underline{R1} \\ \underline{R2} \\ Ro \end{Bmatrix} \qquad (8)$$

where

$Ro=\underline{I}^T\underline{y}$ = constant

$\underline{R1}=[x]\underline{y}$=Kx1 vector

$\underline{R2}=[z]\underline{y}$=MMx1 vector

$\underline{Q1}=\underline{I}[x]$=1xK vector

$\underline{Q2}=\underline{I}[z]$=1xMM vector

$[M1]=[x][x]$=KxK matrix

$[M2]=[z][z]$=MMxMM matrix

$[C]=[x][z]$=KxMM matrix

For a specified order K and M, the system functions h(u) and g(u,v) can be obtrained by solving the set of linear equations (8) with x(t) and y(t) being the cross-flow and in-line responses respectively. The identified system functions h(u) and g(u,v), can be convolved with the measured cross-flow response x(t) to produce predicted linear and quadratic components of the in-line response y1(t) and y2(t) respectively as shown in equation (9). The total predicted in-line response ys(t) and the residual noise terms are also given.

a. $n(t) = y(t)-ys(t)$

b. $ys(t) = y_o+y_1(t) + y_2(t)$

c. $$y_1(t) = \sum_{u=0}^{K-1} h(u)x(t-u) \qquad (9)$$

d. $$y_2(t) = \sum_{u=0}^{M-1}\sum_{v=0}^{M-1} g(u,v)x(t-u)x(t-v)+y_o$$

AN EXAMPLE FOR THE LOCK-IN CASE

In this section, results are presented in which typical lock-in response data were analyzed by using the time domain multiple regression method described in the previous section. The data was obtained from a vibrating, horizontal steel tube 75 feet in length and 1.625 inches in diameter. The tube behaved dynamically as a uniform beam under tension with pinned ends. The mode shapes in both cross-flow (vertical plane) and in-line (horizontal plane) directions were sine waves. The natural frequencies were unequally spaced due to the bending stiffness of the beam. The natural frequencies are the same in the cross-flow and in-line directions. Vortex shedding excited at various times from the second to the tenth modes of vibration. At any given time, the cross-flow and in-line vibration occured in different modes and at different frequencies.

The tube contained seven biaxial pairs of accelerometers distributed along the axis of the tube. The accelerometers measured in-line and cross-flow vibration. Figure 1 shows a time history of motion in the x-y plane measured by a pair of accelerometers located at one fourth of the length of the tube from one end. The figure eight pattern is the result of lock-in cross-flow vibration in the third mode and in-line vibration in the fifth mode. The fifth mode natural frequency is twice the natural frequency of the third mode. The one fourth point of the span is near an anti-node for both mode shapes. At L/4 both node shapes have 70.7% of their maximum anti-node value. The vortex shedding process under lock-in conditions generates a periodic zero mean lift force distributed coherently along the span of the tube. The vortex shedding also creates a non-zero mean drag force which has fluctuating component at twice the frequency of the lift force.

In this example the drag force excitation frequency coincided with the fifth natural frequency of the tube in the in-line direction. The figure eight pattern indicates that although the in-line and cross-flow motions are at different frequencies, they are highly correlated. These x(t) and y(t) measured time series were used in equation (8) to calculate the system functions h(t) and g(u,v) from which the error n(t) was then obtained. By increasing the order K and M, a convergent MSE was reached. The error n(t) for K=30 and M=9 was a wide-band noise indicated by its flat spectrum. The ratio between the MSE and the variance of in-line response was 2.6%. This small amount of wide-band error implied that nonlinearities higher than second order were negligible for the lock-in case and the second order nonlinear system was a reasonable model, relating the cross-flow and in-line response.

From equation (9b), a simulated in-line response ys(t) was obtained which was in good agreement with the measured in-line response y(t). This agreement is easier to visualize by comparing the x-y diagram of cross-flow response x(t) vs. simulated in-line response ys(t), as shown in Figure 2 to the measured x versus y data shown in Figure 1. The linear and quadratic components of the predicted in-line response $y_1(t)$ and $y_2(t)$ were calculated from equations (9c and 9d). The x-y diagrams of x(t) vs. $y_1(t)$ and x(t) vs. $y_2(t)$ in Figure 3 and 4 show that the linear in-line response and quadratic in-line response contribute quite different patterns to the total in-line

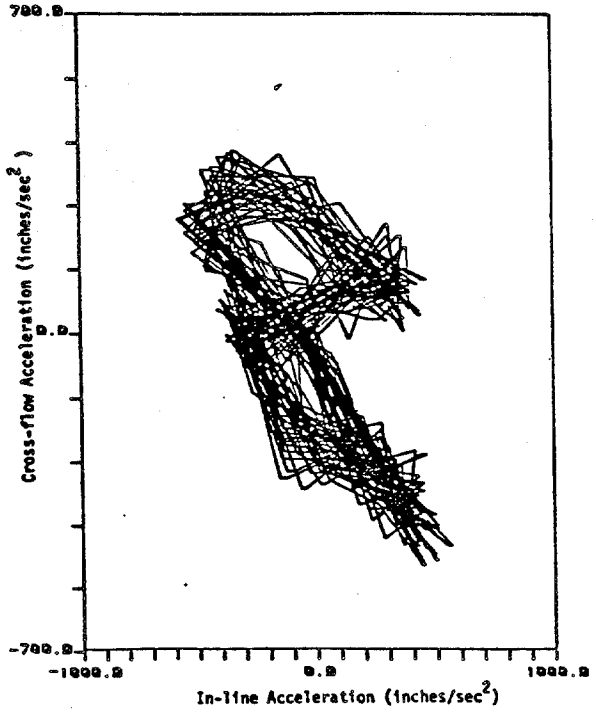

FIG. 1. X, Y Diagram of In-Line Versus Cross-Flow Acceleration

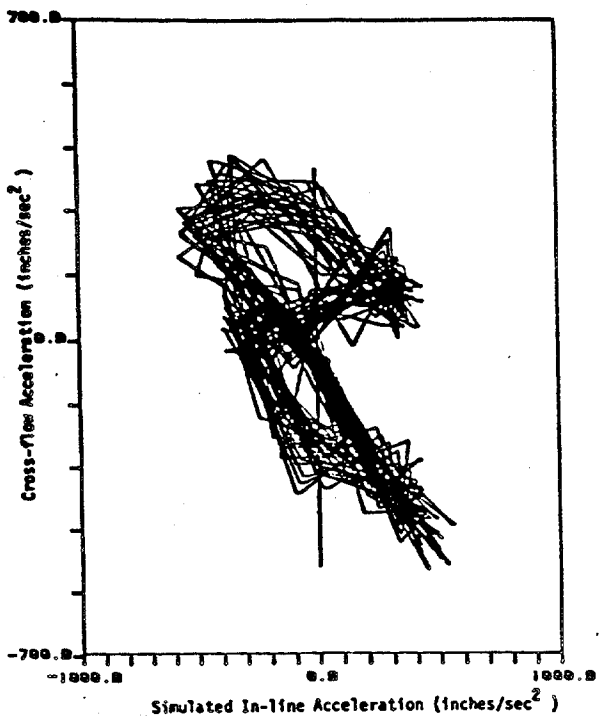

FIG. 2. X, Y Diagram of Cross-Flow Versus Simulated In-Line Acceleration

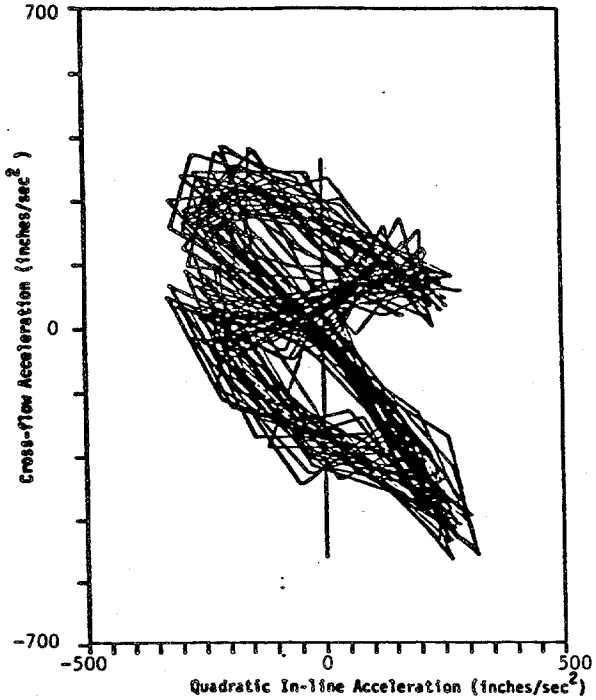

FIG. 3. X, Y Diagram of Cross-Flow Versus The Quadratic Component of In-Line Acceleration

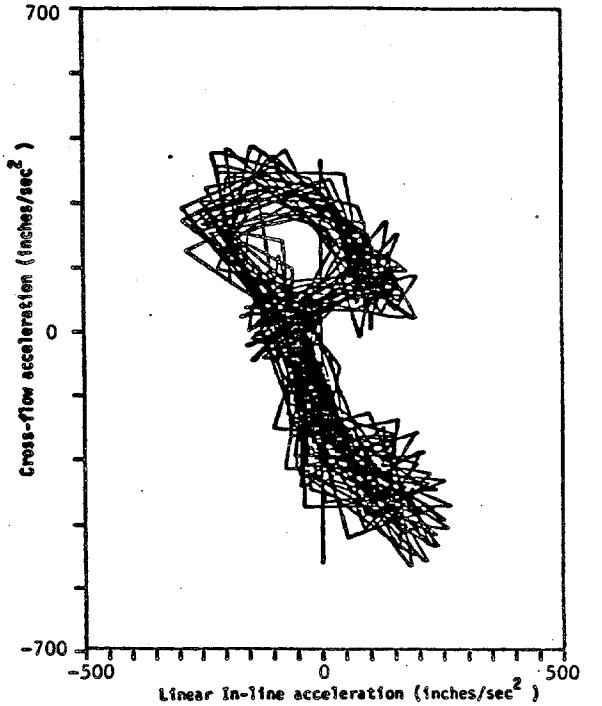

FIG. 4. X, Y Diagram of Cross-Flow Versus The Linear Component of In-Line Acceleration

response.

When the multiple regression method was applied to the non-lock-in case, the rate of convergence was much slower than that of the lock-in case and became inefficient due to the required larger order of K and M. The reason for the slower convergence is that at lock-in, the response time series are quite deterministic. Therefore, only a little past information is required to predict the present response, while the responses at non-lock-in are much more random than the lock-in responses leading to the requirement of a higher order of K and M in equation (1). The quadratic system identification for the non-lock-in case will be discussed in the next section.

QUADRATIC SYSTEM IDENTIFICATION AT NON-LOCK-IN

In this section, a frequency domain multiple regression method for quadratic system identification will be discussed for the non-lock-in case. A quadratic model involving a square law system proposed by Bendat and Piersol [3] is used in the system identification. The residual error is used to evaluate the existance of higher order nonlinearities in the system input/output relationship. High linear coherence between the in-line response and the square of cross-flow response is demonstrated, which provides additional evidence of the existence of the quadratic correlation between in-line and cross-flow response.

Least Squares Quadratic System Identification

A frequency domain quadratic system identification method with the input, a stationary Gaussian random process has been used by several other researchers [5,11]. The method is applied here to non-lock-in response data to obtain the quadratic transfer function.

The input and output of a quadratic system is expressed as given in Equation 1:

$$y(t)= \sum h(u)x(t-u) + \sum\sum g(u,v)x(t-u)x(t-v)+n(t) \quad (1)$$

where n(t) denotes any error associated with the imperfection of the model or noise in the system. Here, a linear term is included even though the in-line and cross-flow response are almost linearly independent [7] for the non-lock-in case. The transfer functions H(W) and $G(W_1, W_2)$, are to be determined such that the mean square error, MSE, of n(t) is minimized. The MSE can be expressed as,

$$MSE=E[n^2(t)]=E[y(t)- \sum h(u)x(t-u) - \sum\sum g(u,v)x(t-u)x(t-v)]^2 \quad (10)$$

Let
$[x(t),X(W)],[y(t),Y(W)], [h(u),H(W)], [g(u,v),G(W_1,W_2)]$

be Fourier transform pairs. We find that

$$MSE=E\Big[\sum_{j=-K}^{K} (Y(Wj)-H(Wj)X(Wj) - \sum_{p+q=j}\sum G(wp,Wq)X(Wp)X(Wq)\exp(iWjt)\Big]^2$$

$$= \sum_{j=-K}^{K} E[Y(W_j)-H(W_j)X(W_j) - \sum_{p+q=j}\sum G(Wp,Wq)X(Wp)X(Wq)]^2 \quad (11)$$

$$= \sum_{j=-K}^{K} E\{|Y(Wj)|^2+|H(Wj)|^2|X(Wj)|^2 -H(Wj)X(Wj)Y^*(Wj)-H^*(Wj)X^*(Wj)Y(Wj) - \sum_{p+q=j}\sum G(Wp,Wq)Y^*(Wj)X(Wp)X(Wq) + \sum_{p+q=j}\sum H^*(Wj)G(Wp,Wq)X^*(Wj)X(Wp)X(Wq) - \sum_{p+q=j}\sum G^*(Wp,Wq)Y(Wj)X^*(Wp)X^*(Wq) + \sum_{p+q=j}\sum H(Wj)G^*(Wp,Wq)X(Wj)X^*(Wp)X^*(Wq)+ \sum_{p+q=j}\sum \sum_{r+s=j}\sum G(Wp,Wq)G^*(Wr,Ws)X(Wp)X(Wq)X^*(Wr)X^*(Ws)\} \quad (12)$$

Let $\partial MSE/\partial H(Wj) =0$, and $\partial MSE/\partial G\ (Wm,Wn) = 0$ with $Wm+Wn=Wj$ for all Wj. We obtain

$$H^*(Wj)E[|X(Wj)|^2]=E[X(Wj)Y^*(Wj)] + \sum_{p+q=j}\sum G^*(Wp,Wq)E[X(Wj)X^*(Wp)X^*(Wq)] \quad (13)$$

$$E[Y^*(Wj)X(Wm)X(Wn)]=H^*(Wj)E[X^*(Wj))X(Wm)X(Wn)] + \sum_{p+q=j}\sum G^*(Wp,Wq)E[X^*(Wp)X^*(Wq)X^*(Wm)X(Wn)] \quad (14)$$

From the following definitions,

$$Sxx(Wj)=E[X(Wj)X(-Wj)]$$

$$Sxy(Wj)=E[X(Wj)Y(-Wj)] \quad (15)$$

$$Bxxx(Wp,Wq)=E[X(Wp)X(Wq)X(-Wp-Wq)]$$

$$Bxxy(Wm,Wn)=E[X(Wm)X(Wn)Y(-Wm-Wn)]$$

Equations (13) and (14) can be rewritten as:

$$H^*(Wj)Sxx(Wj)=Syx(Wj)+ \sum\sum G^*(Wp,Wq)B^*xxx(Wp,Wq) \quad (16)$$

$$Bxxy(Wm,Wn)=H^*(Wj)Bxxx(Wm,Wn) + \sum_{p+q=j}\sum G^*(Wp,Wq)E[X^*(Wp)X^*(Wq)X(Wm)X(Wn)] \quad (17)$$

From these two equations, we see that the determination of the transfer functions H(W) and $G(W_1,W_2)$ required the estimation of the fourth order spectrum, which is difficult, due to computer storage limitations. However, if the input x(t) is a Gaussian random process, this problem can be simplified considerably. If x(t) is a Gaussian random process, the bispectrum Bxxx(Wm,Wn) is zero, and we can write the fourth order cumulant spectrum as:

$$E[X^*(Wp)X^*(Wq)X(Wm)X(Wn)]=$$

$$E[X^*(Wp)X^*(Wq)]E[X(Wm)X(Wn)]+$$

$$E[X^*(Wp)X(Wm)]E[X^*(Wq)X(Wn)]+$$

$$E[X^*(Wp)X(Wn)E[X^*(Wq)X(Wm)]=$$

$$\delta(Wp+Wq)\delta(Wn+Wm)Sxx(Wp)Sxx(Wm) +$$

$$\delta(Wp-Wm)\delta(Wq-Wn)Sxx(Wm)Sxx(Wn)$$

$$\delta(Wp-Wn)\delta(Wq-Wm)Sxx(Wm)Sxx(Wn) \quad (18)$$

The last term in equation (17) for nonzero Wj becomes

$$\sum\sum_{p+q=j} G(Wp,Wq)E[X^*(Wp)X^*(Wq)X(Wm)X(Wn)] = 2G(Wm,Wn)Sxx(Wm)Sxx(Wn) \quad (19)$$

Finally we obtain

$$H(W) = Sxy(W)/Sxx(W) \quad (20)$$

$$G(W_1,W_2)=B^*xxy(W_1,W_2)/2Sxx(W_1)Sxy(W_2) \quad (21)$$

These two equations can be used to determine the linear and quadratic transfer functions, and only require the estimation of the spectra Sxx(W), Sxy(W), and the cross-bispectrum $Bxxy(W_1,W_2)$ for a Gaussian input. It has been shown [7] that the non-lock-in cross-flow response can be approximated by a Gaussian random process as deduced from the Chi-square goodness-of-fit test on the response histogram of the Castine data.

Figures 6 and 5 show the power spectra of the cross-flow and in-line response at non-lock-in. The cross-bicoherence spectrum between these two responses, as shown in Figure 7, indicates a significant quadratic correlation between them. Figure 8 shows the magnitude of the quadratic transfer function $G(W_1,W_2)$ at non-lock-in based on equation (21) with the input cross-flow response a Gaussian random process. Note that in this figure of $G(W_1,W_2)$, all the peaks tend to be concentrated along the 45 degree lines in the bi-frequency plane. While $G(W_1,W_2)$ is the two-dimensional Fourier transform of the second order impulse response kernel g(u,v), for a general quadratic system, it need not possess this particular property. This observation implies that this quadratic system has certain properties which might enable further simplification of the system in the non-lock-in case. A special quadratic system possessing this particular property has been formulated by Bendat and Piersol and will be discussed in the next section.

QUADRATIC SYSTEMS INVOLVING SQUARE-LAW OPERATORS

Two models of a quadratic system which involve a zero memory square-law system, as pictured in Figure 9, have been analyzed by Bendat and Piersol and are briefly discussed here. The zero memory square law system is either followed or preceded by a constant parameter linear system. The properties of these two models, referred to as Case 1 and Case 2, were examined to check if either of them could be used to simplify the quadratic system identification problem for the non-lock-in case.

The combinations of a square-law system and a linear system give the relations between x(t) and y1(t), y2(t) as, from Case 1

$$y1(t)=h1(t)*[x(t)]^2$$

$$= \int h_1(u)[x(t-u)]^2 du$$

$$= \int\int h_1(u)\delta(u-v)x(t-u)x(t-v)du\,dv$$

$$= \int\int g_1(u,v)x(t-u)x(t-v)du\,dv \quad (22)$$

from Case 2

$$y2(t)=[h_2(t)*x(t)]^2$$

$$= [\int h_2(u)x(t-u)du]^2$$

$$= \int\int h_2(u)h_2(v)x(t-u)x(t-v)du\,dv$$

$$= \int\int g_2(u,v)x(t-u)x(t-v)\,du\,dv \quad (23)$$

where * denotes the linear convolution and $\delta(u)$ is the delta function. The second order impulse response kernals for these two cases are

$$g_1(u,v)=h_1(u)\delta(u-v) \quad (24)$$

$$g_2(u,v)=h2(u)h_2(v) \quad (25)$$

The Fourier transforms of these two equations give the quadratic transfer functions $G_1(W_1,W_2)$ and $G_2(W_1,W_2)$, as,

$$G_1(W_1,W_2)=H_1(W_1+W_2) \quad (26)$$

$$G_2(W_1,W_2)=H_2(W_1)H_2(W_2) \quad (27)$$

The system function $H_1(W)$ and $H_2(W)$ can be obtained by writing equations (26) and (27) as

$$G_1(W/2,W/2)=H_1(W/2+W/2)=H_1(W) \quad (28)$$

$$G_2(W,W)=H_2^2(W) \quad (29)$$

By using equation (21) for quadratic system identification with Gaussian inputs, we obtain

$$H_1(W)=G_1(W/2,W/2) = Bxxy_1(W/2,W/2)/2S^2xx(W/2) = Bxy_1(W/2)/2S^2xx(W/2) \quad (30)$$

$$H_2(W)=SQRT[G_2(W,W)]=Bxxy_2(W,W)/2S^2xx(w) = Bxy_2(w)/2S^2xx(W) \quad (31)$$

In which Bxy(W) is the special bispectral density function defined by

$$Bxy(W)=Bxxy(W,W)=E[X(W)X(W)Y^*(2W)] \quad (32)$$

Equations (30) and (31) were derived from the least square error point of view and they are identical to the results formulated by Bendat.

The linear transfer function H(W) derived by Bendat is also identical to the results of section 4 which was

$$H(W)=Sxy(W)/Sxx(W) \quad (33)$$

Checking the properties of the quadratic transfer functions in equations (26) and (27) permits one to determine whether or not the Case 1 model or the Case 2 model is more appropriate to fit to the non-lock-in data. According to equation (26) for Case 1, any peak associated with the function $H_1(W)$ will show up along a 45-degree line in the bi-frequency plane of $G_1(W_1,W_2)$ which is similar to the result stated in section 4, while Case 2 does not possess this property. The Case 1 model was chosen to model the non-lock-in response data. The goodness of fit of the Case 1 model would be checked by the residual n(t).

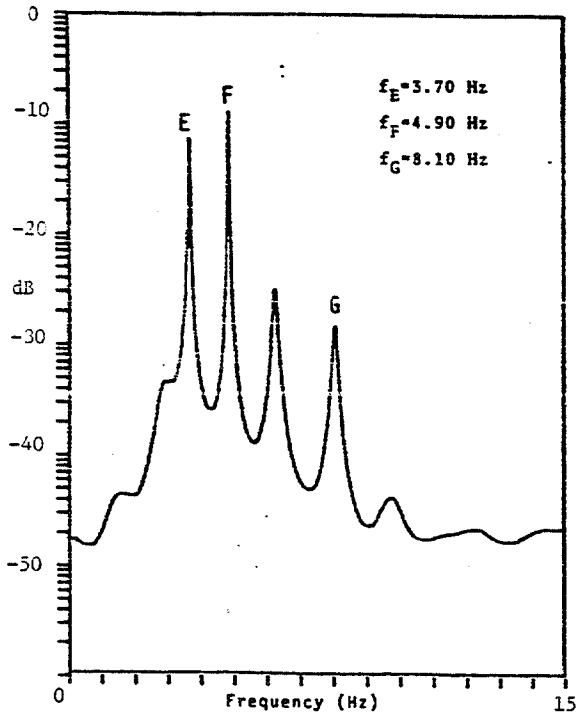

FIG. 5. Power Spectrum of In-Line Acceleration at Non-Lockin

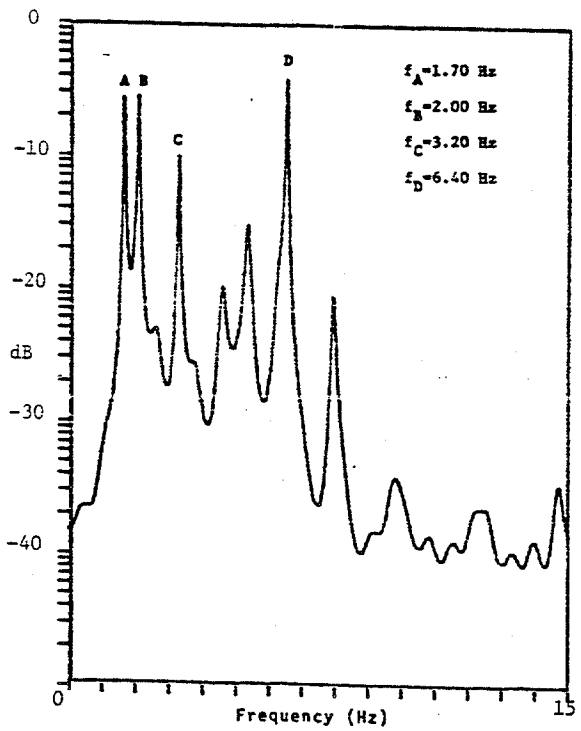

FIG. 6. Power Spectrum of Cross-Flow Acceleration at Non-Lockin

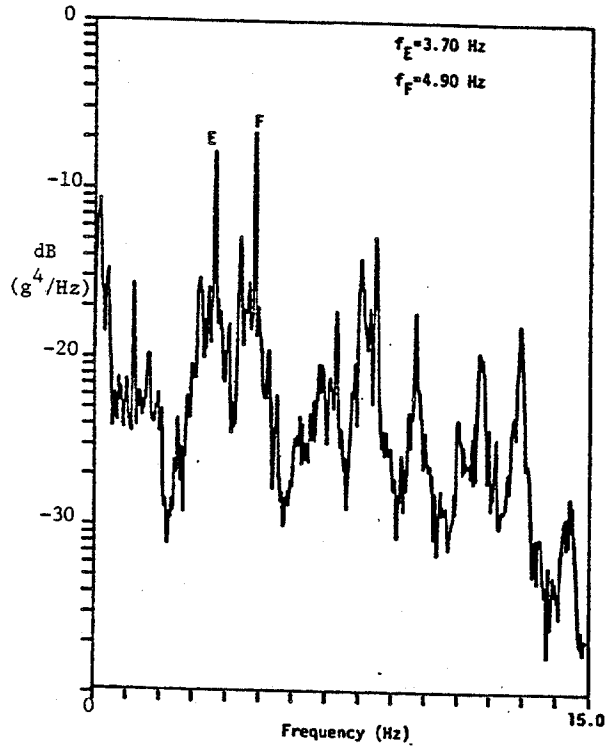

FIG. 10. Power Spectrum of the Square of the Cross-Flow Acceleration

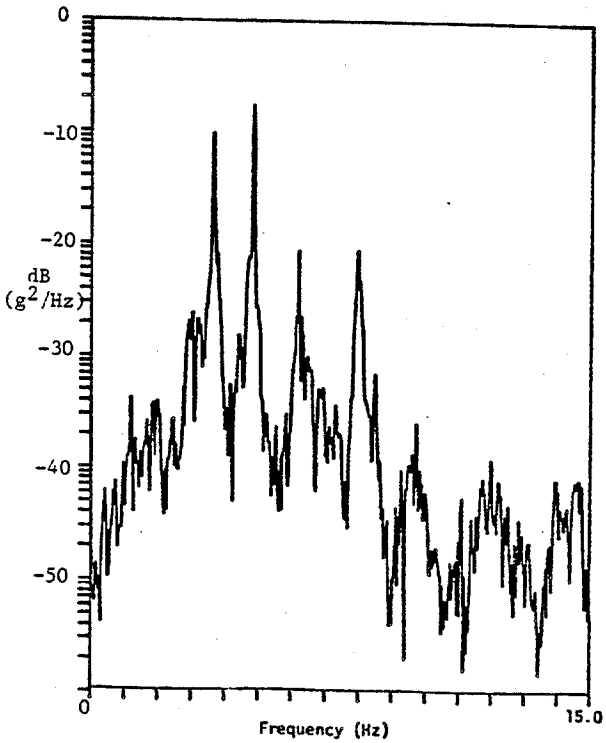

FIG. 11. Spectrum of Simulated In-Line Acceleration

The data presented in the previous section for the non-lock-in cases were analyzed again by using the Case 1 model. The system functions $H(W)$ and $H_1(W)$ were obtained from equations (33) and (30). From the identified system functions $H(W)$ and $H_1(W)$, the spectrums of the residual $n(t)$, the linear and quadratic responses $v(t)$ and $y1(t)$, as well as the simulated in-line response $ys(t)$ were obtained according to,

$$Svv(W)=Sxx(W)\ H(W)^2 \tag{34}$$

$$Sy_1y_1(W)=Sz_1z_1(W)\ H_1(W)^2 \tag{35}$$

$$Sysys(W)=Svv(W)+Sy_1y_1(W) \tag{36}$$

$$Snn(W)=Syy(W)-Sysys(W) \tag{37}$$

A small residual spectrum $Snn(W)$ was obtained which indicated an accurate fit of the Case 1 model to the data. This also meant that higher order nonlinearities were negligible. The spectrum of simulated in-line response $Sysys(W)$ as shown in Figure 11 was in good agreement with in-line response spectrum $Syy(W)$ shown in Figure 5. The spectrum $Sysys(W)$ is almost entirely dominated by the quadratic in-line response. The obtained linear in-line response spectrum $Svv(W)$ was very small and was not shown here. This result is quite different from that of the lock-in case.

Finally, it is interesting to examine the characteristics of the square of the cross-flow response, that is the output $z_1(t)$ from the square-law system in the Case 1 model. Figure 10 shows the spectrum of $z_1(t)$, $Sz_1z_1(W)$, in which the two dominant peaks are located at frequencies exactly equal to that of the in-line response spectrum $Syy(W)$ shown in Figure 5. Figure 12 shows the linear cross-coherence spectrum between $z_1(t)$ and $y(t)$ which demonstrates that these two fluctuating quantities were highly linearly coherent as shown by the high peaks at the two dominant frequencies. This result provided additional evidence of the existence of quadratic correlation between cross-flow and in-line response.

CONCLUSIONS

In conclusion, it should be emphasized that although the results presented in this paper are based on data taken from a single mechanical system, they do suggest that the relationship between cross-flow and in-line response might be best described by a second order nonlinear system for both lock-in and non-lock-in cases. Nonlinear correlations higher than second order were negligible in the nonlinear relationship for both cases. Furthermore, it was indicated in this paper that quadratic transfer functions can be computed by using both time domain and frequency domain multiple regression methods. Knowledge of these transfer functions may be useful in modelling the relationship between cross-flow and in-line response, or equivalently, the lift and drag forces of flow-induced vibration. In addition, for the non-lock-in cases, the square-law system provided a potential way to simplify modelling of the relationship.

In the case of frequency domain analysis, it has been assumed that the non-lock-in cross-flow response is Gaussian. For other applications of quadratic system identification with non-Gaussian input, one can use the time domain multiple regression method to obtain the impulse response kernels. However, the practicality of this method is not clear for a random input case.

ACKNOWLEDGEMENTS

This research represents a segment of a multiyear program at M.I.T. focussed on the understanding of flow-induced vibration. The overall program has had broad federal and industrial support. This particular portion was sponsored by the Technology Assessment and Research Branch of the Minerals Management Service and by the Marine Technology Division of the Naval Research Laboratory.

REFERENCES

1. Bendat, J.S. and Piersol, A.G., Spectral Analysis of Nonlinear Systems Involving Square-Law Operators," J. of Sound and Vibration, 81(2), 1982.

2. Bendat, J.S. and Piersol, A.G., Random Data: Analysis and Measurement Procedures, John Wiley and Sons, New York, 1971.

3. Brillinger, D.R., Time Series. New York: Holt 1975.

4. Brillinger, D.R. and M. Rosenblatt, "Asymptotic Theory of Estimate of K-th Order Spectra," in Spectral Analysis of Series, B. Harris, Ed. New York: Wiley, 1967.

5. Brillinger, D.R., "Identification of Polynomial Systems by Means of Higher Order Spectra," J. of Sound and Vibration, 12(3), 301-313, 1970.

6. Jenkins, G.M. and Watts, D.G., Spectral Analysis and Its Application, San Francisco, CA: Holden-Day, 1968.

7. Jong, Jen-Yi, "The Quadratic Correlation Between In-Line and Cross-Flow, Vortex-Induced Vibration of Long Flexible Cylinders," MIT Ocean Engineering Department, Ph.D. Dissertation, 1984.

8. Jong, Jen-Yi and Vandiver, J.K., "Response Analysis of the Flow-Induced Vibration of Flexible Cylinders Tested at Castine, Maine in July and August of 1981," MIT Ocean Engineering Department Report, 1983.

9. Kim, Y.C. and Powers, E.J., "Digital Bispectral Analysis and Its Application to Nonlinear Wave Interactions," IEEE Transactions on Plasma Science, Vol. PS7 No. 2, June 1979.

10. Kim, Y.C., Wang, W.F., Powers, E.J., and Roth, J.R., "Extension of the Coherence Function to Quadratic Models," Proceedings of the IEEE, Vol. 67, No. 3, March 1979.

11. Powers, E.J., Choi, D. and Miksad, R.W., "Determination of Nonlinear Drift Force Quadratic Transfer Functions by Digital Cross-Bispectral Analysis," Offshore Technology Conference, Paper No. 4440, 1982.

12. King, R., "A Review of Vortex Shedding Research and Its Application," Ocean Engineering, New England Section, Sept. 26, 1975.

13. Sarpakaya, T., "Vortex Induced Oscillations. A Selective Review," ASME J. of Applied Mechanics, Vol. 46, June 1979, pp. 241.

14. Vandiver, J.K and Griffin, O.M., Measurement of the Vortex Excited Strumming Vibrations of Marine Cable," Proc. of Ocean Structural Dynamics, 1982.

15. Vandiver, J.K., "Natural Frequency, Mode Shape, and Damping Ratios for Cylinders Tested at Castine, Maine in the Summer of 1981," unpublished MIT Ocean Engineering Report.

16. Vandiver, J.K. and Mazal, C.H., "A Field Study of Vortex-Excited Vibrations of Marine Cable," Offshore Technology Conference, OTC Paper No. 2491, Houston, Texas, 1976.

17. Vandiver, J.K., "Drag Coefficients of Long Flexible Cylinders," Offshore Technology Conference, OTC Paper No. 4490, Houston, Texas 1983.

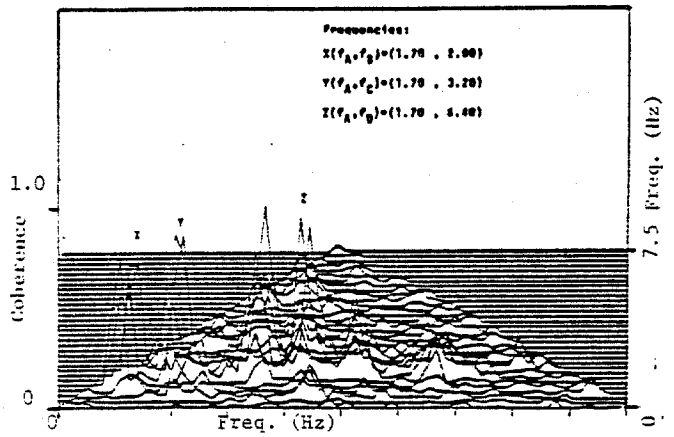

FIG. 7. Cross Bicoherence Between Cross-Flow and In-Line Acceleration

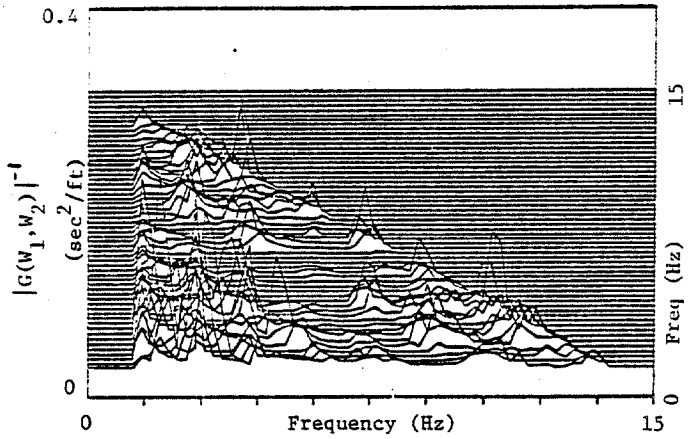

FIG. 8. Quadratic Transfer Function Between Cross-Flow and In-Line Acceleration

Case 1

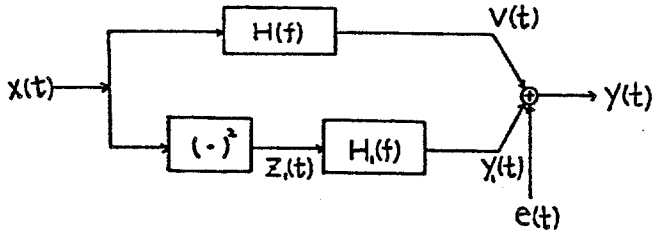

Case 2

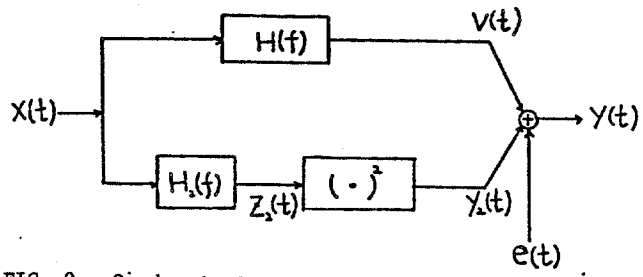

FIG. 9. Quadratic Systems with Square Law Operators

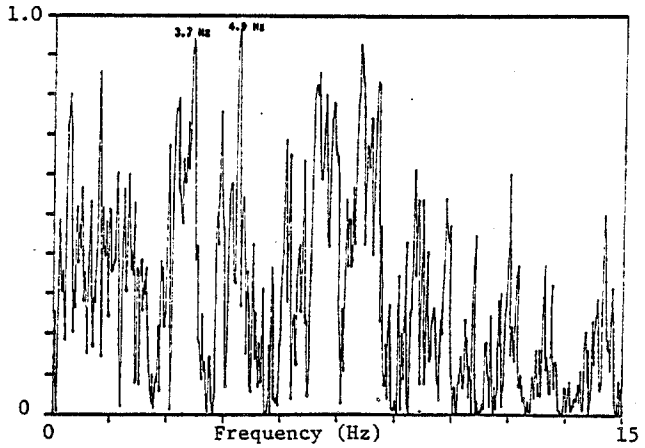

FIG. 12. Linear Coherence Between In-Line Acceleration and the Square of the Cross-Flow Acceleration